

The CO-to-H₂ Conversion Factor

Alberto D. Bolatto,¹ Mark Wolfire,¹
and Adam K. Leroy²

¹Department of Astronomy, University of Maryland, College Park, Maryland 20742;
email: bolatto@astro.umd.edu, mwolfire@astro.umd.edu

²National Radio Astronomy Observatory, Charlottesville, Virginia 22903;
email: aleroy@nrao.edu

Annu. Rev. Astron. Astrophys. 2013. 51:207–68

First published online as a Review in Advance on
June 26, 2013

The *Annual Review of Astronomy and Astrophysics* is
online at astro.annualreviews.org

This article's doi:
10.1146/annurev-astro-082812-140944

Copyright © 2013 by Annual Reviews.
All rights reserved

Keywords

ISM: general, ISM: molecules, galaxies: ISM, radio lines: ISM

Abstract

CO line emission represents the most accessible and widely used tracer of the molecular ISM. This renders the translation of observed CO intensity into total H₂ gas mass critical to understanding star formation and the ISM in our Galaxy and beyond. We review the theoretical underpinning, techniques, and results of efforts to estimate this CO-to-H₂ “conversion factor,” X_{CO} , in different environments. In the Milky Way disk, we recommend a conversion factor of $X_{\text{CO}} = 2 \times 10^{20} \text{ cm}^{-2} (\text{K km s}^{-1})^{-1}$ with $\pm 30\%$ uncertainty. Studies of other “normal galaxies” return similar values in Milky Way–like disks, but with greater scatter and systematic uncertainty. Departures from this Galactic conversion factor are both observed and expected. Dust-based determinations, theoretical arguments, and scaling relations all suggest that X_{CO} increases with decreasing metallicity, turning up sharply below metallicity $\sim 1/3$ – $1/2$ solar in a manner consistent with model predictions that identify shielding as a key parameter. Based on spectral line modeling and dust observations, X_{CO} appears to drop in the central, bright regions of some but not all galaxies, often coincident with regions of bright CO emission and high stellar surface density. This lower X_{CO} is also present in the overwhelmingly molecular ISM of starburst galaxies, where several lines of evidence point to a lower CO-to-H₂ conversion factor. At high redshift, direct evidence regarding the conversion factor remains scarce; we review what is known based on dynamical modeling and other arguments.

1. INTRODUCTION

Molecular hydrogen, H_2 , is the most abundant molecule in the Universe. With the possible exception of the very first generations of stars, star formation is fueled by molecular gas. Consequently, H_2 plays a central role in the evolution of galaxies and stellar systems (see the recent review by Kennicutt & Evans 2012). Unfortunately for astronomers interested in the study of the molecular ISM, cold H_2 is not directly observable in emission. H_2 is a diatomic molecule with identical nuclei and therefore possesses no permanent dipole moment and no corresponding dipolar rotational transitions. The lowest energy transitions of H_2 are its purely rotational quadrupole transitions in the far-IR (FIR) at $\lambda = 28.22 \mu\text{m}$ and shorter wavelengths. These are weak owing to their long spontaneous decay lifetimes of $\tau_{\text{decay}} \sim 100$ years. More importantly, the two lowest para and ortho transitions have upper-level energies of $E/k \approx 510$ K and 1,015 K above ground (Dabrowski 1984). They are thus only excited in gas where $T \gtrsim 100$ K. The lowest vibrational transition of H_2 is even more difficult to excite, with a wavelength of $\lambda = 2.22 \mu\text{m}$ and a corresponding energy of $E/k = 6,471$ K. Thus, the cold molecular hydrogen that makes up most of the molecular ISM in galaxies is, for all practical purposes, invisible in emission.

Fortunately, molecular gas is not pure H_2 . Helium, being monoatomic, suffers from similar observability problems in cold clouds, but the molecular ISM also contains heavier elements at the level of a few $\times 10^{-4}$ atoms per H nucleon. The most abundant of these are oxygen and carbon, which combine to form CO under the conditions prevalent in molecular clouds. CO has a weak permanent dipole moment ($\mu \approx 0.11$ D = 0.11×10^{-18} esu cm) and a ground rotational transition with a low excitation energy of $h\nu/k \approx 5.53$ K. With this low energy and critical density (further reduced by radiative trapping due to its high optical depth), CO is easily excited even in cold molecular clouds. At a wavelength of 2.6 mm, the $J = 1 \rightarrow 0$ transition of CO lies in a fairly transparent atmospheric window. It has thus become the workhorse tracer of the bulk distribution of H_2 in our Galaxy and beyond.

As a consequence, astronomers frequently employ CO emission to measure molecular gas masses. The standard methodology posits a simple relationship between the observed CO intensity and the column density of molecular gas, such that

$$N(\text{H}_2) = X_{\text{CO}} W(^{12}\text{C}^{16}\text{O } J = 1 \rightarrow 0), \quad (1)$$

where the column density, $N(\text{H}_2)$, is in per centimeters squared and the integrated line intensity, $W(\text{CO})$, is in traditional radio astronomy observational units of Kelvins kilometers per second (henceforth, we refer to the most common $^{12}\text{C}^{16}\text{O}$ isotopologue as simply CO and, unless otherwise noted, to the ground rotational transition $J = 1 \rightarrow 0$). A corollary of this relation arises from integrating over the emitting area and correcting by the mass contribution of heavier elements mixed in with the molecular gas,

$$M_{\text{mol}} = \alpha_{\text{CO}} L_{\text{CO}}. \quad (2)$$

Here, M_{mol} is in units of solar mass and L_{CO} is usually expressed in Kelvins kilometers parsecs squared per second. L_{CO} relates to the observed integrated flux density in galaxies via $L_{\text{CO}} = 2,453 S_{\text{CO}} \Delta v D_L^2 / (1 + z)$, where $S_{\text{CO}} \Delta v$ is the integrated line flux density in Janskys kilometers per second, D_L is the luminosity distance to the source in megaparsecs, and z is the redshift [e.g., Solomon & Vanden Bout 2005; our Equation 7 can be used to convert between $W(\text{CO})$ and $S_{\text{CO}} \Delta v$]. Thus, α_{CO} is simply a mass-to-light ratio. The correction for the contribution of heavy elements by mass reflects chiefly helium and amounts to an $\sim 36\%$ correction based on cosmological abundances.

Both X_{CO} and α_{CO} are referred to as the CO-to- H_2 conversion factor. For $X_{\text{CO}} = 2 \times 10^{20} \text{ cm}^{-2} (\text{K km s}^{-1})^{-1}$, the corresponding α_{CO} is $4.3 M_{\odot} (\text{K km s}^{-1} \text{ pc}^{-2})^{-1}$. To translate integrated flux

density directly to molecular mass, Equation 2 can be written as

$$M_{\text{mol}} = 1.05 \times 10^4 \left(\frac{X_{\text{CO}}}{2 \times 10^{20} \frac{\text{cm}^{-2}}{\text{K km s}^{-1}}} \right) \frac{S_{\text{CO}} \Delta v D_{\text{L}}^2}{(1+z)} M_{\odot}. \quad (3)$$

For convenience, we define

$$X_{\text{CO},20} \equiv \frac{X_{\text{CO}}}{1 \times 10^{20} \text{ cm}^{-2} (\text{K km s}^{-1})^{-1}}. \quad (4)$$

We discuss the theoretical underpinnings of these equations in Section 2.

Note that the emission from CO $J = 1 \rightarrow 0$ is consistently optically thick except along very low column density lines of sight, as indicated by ratios of ^{12}CO to ^{13}CO intensities much lower than the isotopic ratio. The reason for this is simple to illustrate. The optical depth of a CO rotational transition is

$$\tau_J = \frac{8\pi^3}{3b} \mu^2 \frac{J}{g_J} (e^{h\nu_J/kT_{\text{ex}}} - 1) \frac{N_J}{\Delta v}, \quad (5)$$

where J and N_J are the rotational quantum number and the column density, respectively, in the upper level of the $J \rightarrow J - 1$ transition; ν is the frequency; T_{ex} is the excitation temperature (in general, a function of J and restricted to being between the gas kinetic temperature and that of the cosmic microwave background); Δv is the velocity width; μ is the dipole moment; $g_J = 2J + 1$ is the statistical weight of level J ; and b and k are the Planck and Boltzmann constants, respectively. Under typical conditions at the molecular boundary, $\tau \approx 1$ for the $J = 1 \rightarrow 0$ transition requires $N(\text{H}_2) \approx 2\text{--}3 \times 10^{20} \text{ cm}^{-2}$ for a Galactic carbon gas-phase abundance of $A_{\text{C}} \sim 1.6 \times 10^{-4}$ (Sofia et al. 2004). At the outer edge of a cloud the carbon is mainly C^+ , which then recombines with electrons to form neutral C (**Figure 1**). Carbon is converted to CO by a series of reactions initiated by the cosmic-ray ionization of H or H_2 (e.g., van Dishoeck & Black 1988) and becomes the dominant carrier of carbon at $A_{\text{V}} \sim 1\text{--}2$. The CO $J = 1 \rightarrow 0$ line turns optically thick very quickly after CO becomes a significant carbon reservoir, over a region of thickness of $\Delta A_{\text{V}} \sim 0.2\text{--}0.3$ for a typical Galactic dust-to-gas ratio.

Equations 1 and 2 represent highly idealized, simplified relations where all the effects of environment, geometry, excitation, and dynamics are subsumed into the X_{CO} or α_{CO} coefficients. A particular example is the effect that spatial scales have on the CO-to- H_2 conversion factor. Indeed, for the reasons discussed in the previous paragraph, X_{CO} along a line of sight through a dense molecular cloud where $A_{\text{V}} \gtrsim 10$ is not expected to be the same as X_{CO} along a diffuse line of sight sampling mostly material where $A_{\text{V}} < 1$ (see, for example, Pineda et al. 2010b, Liszt & Pety 2012). Thus on small spatial scales we expect to see large variability in the CO-to- H_2 conversion factor. This variability averages out on the large spatial scales to a typical value corresponding to the dominant environment. Because of the large optical depth of the CO $J = 1 \rightarrow 0$ transition, the velocity dispersion giving rise to the width of the CO line also plays an important role on $W(\text{CO})$ and indirectly on X_{CO} . Indeed, there is not one value of X_{CO} that is correct and applicable to each and every situation, although there are values with reasonable uncertainties that are applicable over large galactic scales.

The plan of this review is as follows: In the remainder of this section, we provide a brief historical introduction. In Section 2, we present the theoretical background to the CO-to- H_2 conversion factor. In Section 3, we discuss the results of recent calculations of molecular clouds including the effects of turbulence and chemistry. In Section 4, we review the methodology and measurements of X_{CO} in the Milky Way, the best-understood environment. We characterize the range of values that have been found and the underlying physics for each measurement technique. In Section 5, we review the literature on X_{CO} determinations in normal star-forming galaxies

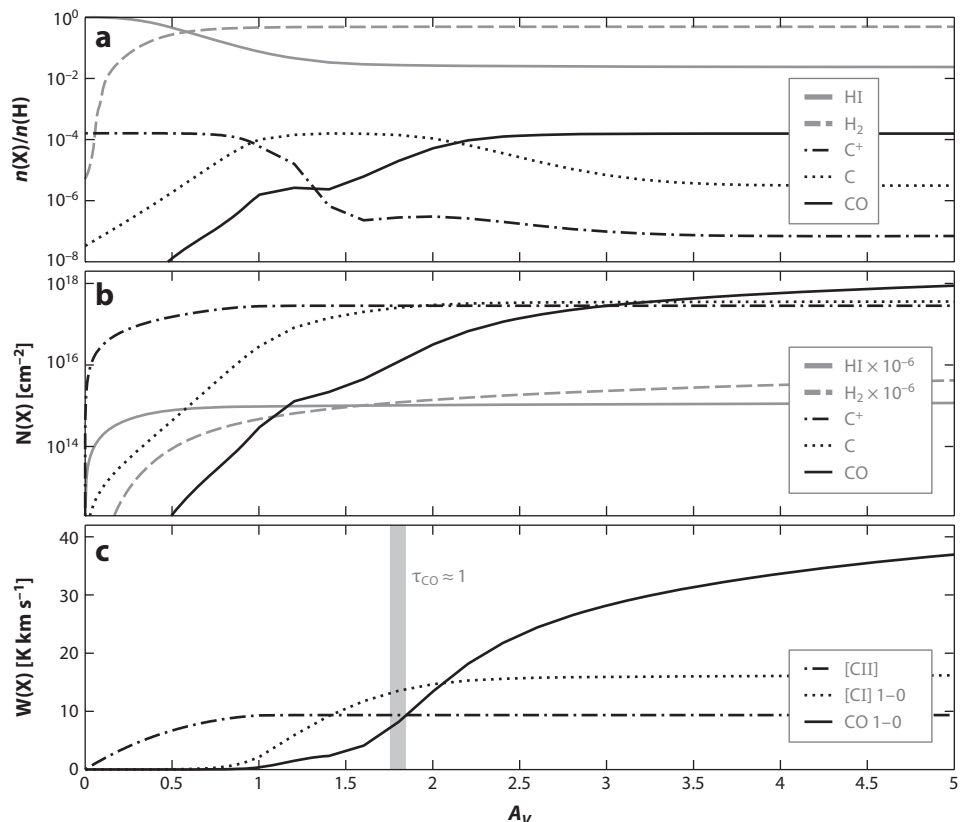


Figure 1

Calculated cloud structure as a function of optical depth into the cloud. (a) Shows the fractional abundance of HI, H_2 , C^+ , C, and CO. (b) Shows integrated column densities of abundances in a from the cloud edge. (c) Shows the emergent line intensity in units of Kelvins kilometers per second for [CII] 158 μm , [CI] 609 μm , and CO $J = 1 \rightarrow 0$. The gray vertical bar shows where CO $J = 1 \rightarrow 0$ becomes optically thick. At the outer edge of the cloud, gas is mainly HI. H_2 forms at $A_V \sim 0.5$, whereas the carbon is mainly C^+ . The C^+ is converted to C at $A_V \sim 1$ and CO dominates at $A_V \gtrsim 2$. The model uses constant H density $n = 3 \times 10^3 cm^{-3}$, a radiation field $\chi = 30$ times the interstellar radiation field described by Draine (1978), a primary cosmic-ray ionization rate of $2 \times 10^{-16} s^{-1}$ per hydrogen nucleon, and these calculations are based on the photodissociation region models constructed by Wolfire, Hollenbach & McKee (2010) and Hollenbach et al. (2012).

and discuss the techniques available to estimate X_{CO} in extragalactic systems. In Section 6, we consider the effect of metallicity, a key local physical parameter. In Section 7, we review the measurements and the physical mechanisms affecting the value of the CO-to- H_2 conversion factor in the starburst environments of luminous and ultraluminous IR galaxies (LIRGs, ULIRGs). In Section 8, we consider the explicit case of X_{CO} in high-redshift systems, where a much more restricted range of observations exists. Finally in Section 9, we offer some recommendations and caveats as to the best values of X_{CO} to use in different environments, as well as some suggestions about open avenues of research on the topic.

1.1. Brief Historical Perspective

Carbon monoxide was one of the first ISM molecules observed at millimeter wavelengths. Wilson, Jefferts & Penzias (1970) reported the discovery of intense CO emission from the Orion nebula using the 36-foot NRAO antenna at Kitt Peak, Arizona. Surveys of molecular clouds in the Galaxy (e.g., Solomon et al. 1972, Wilson et al. 1974, Burton et al. 1975, Scoville & Solomon 1975) established molecular gas to be widespread in the inner Milky Way with a distribution that resembles giant HII regions more closely than that of atomic hydrogen gas. The combination of CO and γ -ray observations demonstrated that H₂ dominates over HI by mass in the inner Galaxy (Stecker et al. 1975). By the end of the following decade, these studies extended to complete the mapping of the Galactic plane (Dame et al. 1987).

The first extragalactic detections of CO occurred in parallel with these early Galactic surveys (Rickard et al. 1975, Solomon & de Zafra 1975). They found CO to be particularly bright in galaxies with nuclear activity such as M82 and NGC 253. The number of extragalactic CO observations grew rapidly to include several hundred galaxies over the next two decades (Young & Scoville 1991, Young et al. 1995), and CO emission was employed to determine galaxy molecular masses (Young & Scoville 1982). By the late 1980s, the first millimeter interferometers spatially resolved molecular clouds in other galaxies (Vogel, Boulanger & Ball 1987; Wilson et al. 1988). Such observations remain challenging, though powerful new interferometric facilities such as the Atacama Large Millimeter Array (ALMA) will change that.

The first detection of CO at cosmological redshifts targeted ultraluminous IR sources and revealed very large reservoirs of highly excited molecular gas (Brown & Vanden Bout 1991; Solomon, Downes & Radford 1992). Because of the deep integrations required, the number of high-redshift CO detections grew slowly at first (Solomon & Vanden Bout 2005), but this field is now developing rapidly driven by recent improvements in telescope sensitivity (see the review by Carilli & Walter 2013 in this volume). An increased appreciation of the roles of gas and star formation in the field of galaxy evolution and the concordant need to determine accurate gas masses provide two of the motivations for this review.

1.2. CO Excitation

Under average molecular cloud conditions, CO molecules are excited through a combination of collisions with H₂ and radiative trapping. They de-excite through spontaneous emission and collisions, except at very high densities where collisions are extremely frequent. Neglecting the effect of radiative trapping, radiative and collisional de-excitation balance for a critical density of $n_{cr,J} \equiv A_J/\gamma_J(T_{kin})$ (neglecting the effects of stimulated emission), where T_{kin} is the kinetic gas temperature. Thus for $n \gg n_{cr,J}$ and excitation temperatures $T_{ex,J} \gg E_J/k \approx 5.53 J(J+1)/2$ K, the upper level of the $J \rightarrow J-1$ transition is populated and the molecule emits brightly. In these expressions, A_J is the Einstein coefficient for spontaneous emission (only transitions with $|\Delta J| = 1$ are allowed): $A_J = 64\pi^4 v_J^3 \mu^2 J/(3hc^3 g_J) (A_1 \approx 7.11 \times 10^{-8} \text{ s}^{-1})$. The parameter $\gamma_J(T)$ is the corresponding collisional coefficient (the sum of all collisional rate coefficients for transitions with upper level J), which is a weak function of temperature. For CO, $\gamma_1 \sim 3.26 \times 10^{-11} \text{ cm}^3 \text{ s}^{-1}$ for collisions with H₂ at $T_{kin} \approx 30$ K (Yang et al. 2010). $T_{ex,J}$ refers to the excitation temperature, defined as the temperature needed to recover the relative populations of the J and $J-1$ levels from the Boltzmann distribution. In general, $T_{ex,J}$ is different for different transitions.

The critical density for the CO $J = 1 \rightarrow 0$ transition is $n(\text{H}_2)_{cr,1} \sim 2,200 \text{ cm}^{-3}$. Higher transitions require rapidly increasing densities and temperatures to be excited, as $n_{cr,J} \propto J^3$ and

$E_J \propto J^2$. The high optical depth of the CO emission relaxes these density requirements, as radiative trapping reduces the effective density required for excitation by a factor of $\sim 1/\tau_J$ (the precise factor corresponds to an escape probability and is dependent on geometry).

The Rayleigh-Jeans brightness temperature, T_J , measured by a radio telescope for the $J \rightarrow J-1$ transition is

$$T_J \approx 5.53J(1 - e^{-\tau_J}) \left(\frac{1}{e^{\frac{5.53J}{T_{ex,J}}} - 1} - \frac{1}{e^{\frac{5.53J}{2.73(z+1)}} - 1} \right) \text{K}. \quad (6)$$

The final term accounts for the effect of the cosmic microwave background at the redshift, z , of interest. Note that frequently the Rayleigh-Jeans brightness temperature is referred to as the radiation temperature. Observations with single-dish telescopes usually yield antenna temperatures corrected by atmospheric attenuation (T_A^*), or main beam temperatures (T_{MB}), such that $T_{MB} = \eta_{MB} T_A^*$, where η_{MB} is the main beam efficiency of the telescope at the frequency of the observation (see Kutner & Ulich 1981 for further discussion). The Rayleigh-Jeans brightness temperature T_J is identical to T_{MB} for compact sources, whereas extended sources may couple to the antenna with a slightly different efficiency.

Extragalactic results, and measurements with interferometers, are frequently reported as flux densities rather than brightness temperatures. The relations between flux density (in Janskys) and Rayleigh-Jeans brightness temperature (in Kelvins) in general, and for CO lines, are

$$S_J \cong 73.5 \times 10^{-3} \lambda^{-2} \theta^2 T_J \approx 10.9 \times 10^{-3} J^2 \theta^2 T_J, \quad (7)$$

where θ is the half-maximum at full width of the telescope beam (in arcseconds), and λ is the wavelength of a transition (in millimeters).

The Rayleigh-Jeans brightness temperature, T_J , excitation temperature, $T_{ex,J}$, and kinetic temperature, T_{kin} , are distinct but related. The ^{12}CO transitions usually have $\tau_J \gg 1$, making the Rayleigh-Jeans brightness temperature a probe of the excitation temperature, $T_J \sim T_{ex,J}$, for $T_{ex,J} \gg 5.53J$ K. In general $T_{ex,J}$ can be shown to be in the range of $T_{cmb} \leq T_{ex,J} \leq T_{kin}$. At densities much higher than $n_{cr,J}$, the population of the levels J and lower approach a Boltzmann distribution and become thermalized at the gas kinetic temperature, $T_{ex,J} \approx T_{kin}$. The corresponding Rayleigh-Jeans brightness can be computed using Equation 6. When $T_{ex,J} < T_{kin}$, usually $T_{ex,J}/T_{ex,J-1} < 1$ for lines arising in the same parcel of gas, and the excitation of the J level is subthermal (note that this is not equivalent to $T_J/T_{J-1} < 1$, as is sometimes used in the literature).

2. THEORETICAL BASIS

At its core, the X_{CO} factor represents a valiant effort to use the bright but optically thick transition of a molecular gas impurity to measure total molecular gas masses. How and why does X_{CO} work?

2.1. Giant Molecular Clouds

Because the $^{12}\text{CO } J = 1 \rightarrow 0$ transition is generally optically thick, its brightness temperature is related to the temperature of the $\tau_{\text{CO}} = 1$ surface, not the column density of the gas. Information about the mass of a self-gravitating entity, such as a molecular cloud, is conveyed by its line width, which reflects the velocity dispersion of the emitting gas.

A simple and exact argument can be made for virialized molecular clouds; that is, clouds where twice the internal kinetic energy equals the potential energy. Following Solomon et al. (1987), the

virial mass M_{vir} of a giant molecular cloud (GMC) in solar mass is

$$M_{vir} = \frac{3(5-2k)}{G(3-k)} R \sigma^2, \quad (8)$$

where R is the projected radius (in parsecs), σ is the 1D velocity dispersion (in kilometers per second; $\sigma_{3D} = \sqrt{3}\sigma$), G is the gravitational constant ($G \approx 1/232 \text{ M}_{\odot}^{-1} \text{ pc km}^2 \text{ s}^{-2}$), and k is the power-law index of the spherical volume density distribution, $\rho(r) \propto r^{-k}$. The coefficient in front of $R\sigma^2$ is only weakly dependent on the density profile of the virialized cloud and corresponds to approximately 1,160, 1,040, and 700 for $k = 0, 1$, and 2 , respectively (MacLaren, Richardson & Wolfendale 1988; Bertoldi & McKee 1992). Unless otherwise specified, we adopt $k = 1$ for the remainder of the discussion. This expression of the virial mass is fairly robust if other terms in the virial theorem (McKee & Zweibel 1992, Ballesteros-Paredes 2006), such as magnetic support, can be neglected (for a more general expression applicable to spheroidal clouds and a general density distribution, see Bertoldi & McKee 1992). As long as molecular gas is dominating the mass enclosed in the cloud radius and the cloud is approximately virialized, M_{vir} is a good measure of the H_2 mass.

Empirically, molecular clouds are observed to follow a size–line width relation (Larson 1981, Heyer et al. 2009) such that approximately

$$\sigma = CR^{0.5}, \quad (9)$$

with $C \approx 0.7 \text{ km s}^{-1} \text{ pc}^{-0.5}$ (Scoville et al. 1987, Solomon et al. 1987, Roman-Duval et al. 2010). This relation is an expression of the equilibrium supersonic turbulence conditions in a highly compressible medium, and it is thought to apply under very general conditions (see section 2.1 of McKee & Ostriker 2007 for a discussion). In fact, within our current ability to measure these two quantities, such a relation is also approximately followed by extragalactic GMCs in galaxy disks (e.g., Rubio, Lequeux & Boulanger 1993; Bolatto et al. 2008; Hughes et al. 2010).

Note that insofar as the size dependence of Equation 9 is close to a square root, the combination of Equations 8 and 9 yields that $M_{vir} \propto \sigma^4$, and molecular clouds that fulfill both relations have a characteristic mean surface density, Σ_{GMC} , at a value related to the coefficient of Equation 9 so that $\Sigma_{\text{GMC}} = M_{vir}/\pi R^2 \approx 331C^2$ for our chosen density profile $\rho \propto r^{-1}$. We return to the question of Σ_{GMC} in the Milky Way in Section 4.4.

Because the CO luminosity of a cloud, L_{CO} , is the product of its area (πR^2) and its integrated surface brightness ($T_B \sqrt{2\pi} \sigma$), then $L_{\text{CO}} = \sqrt{2\pi^3} T_B \sigma R^2$, where T_B is the Rayleigh-Jeans brightness temperature of the emission (see Section 1.2). Using the size–line width relation (Equation 9) to substitute for R implies that $L_{\text{CO}} \propto T_B \sigma^5$. Employing this relation to replace σ in $M_{vir} \propto \sigma^4$, we obtain a relation between M_{vir} and L_{CO} ,

$$M_{vir} \approx M_{mol} \approx 200 \left(\frac{C^{1.5} L_{\text{CO}}}{T_B} \right)^{0.8}. \quad (10)$$

That is, for GMCs near virial equilibrium with approximately constant brightness temperature, T_B , we expect an almost linear relation between virial mass and luminosity. The numerical coefficient in Equation 10 is only a weak function of the density profile of the cloud. Then using the relation between C and Σ_{GMC} we obtain the following expression for the conversion factor,

$$\alpha_{\text{CO}} \equiv \frac{M_{mol}}{L_{\text{CO}}} \approx 6.1 L_{\text{CO}}^{-0.2} T_B^{-0.8} \Sigma_{\text{GMC}}^{0.6}. \quad (11)$$

Equations 10 and 11 rely on a number of assumptions. We assume (a) virialized clouds with (b) masses dominated by H_2 that (c) follow the size–line width relation and (d) have approximately

constant temperature. Equation 11 applies to a single, spatially resolved cloud, as Σ_{GMC} is the resolved surface density.

We defer the discussion of the applicability of the virial theorem to Section 4.1.1 and the effect of other mass components to Section 2.3. The assumption of a size–line width relation relies on our understanding of the properties of turbulence in the ISM. The result $\sigma \propto \sqrt{R}$ follows our expectations for a highly compressible turbulent flow, with a turbulence injection scale at least comparable to GMC sizes. The existence of a narrow range of proportionality coefficients, corresponding to a small interval of GMC average surface densities, is less well understood (for an alternative view on this point, see Ballesteros-Paredes et al. 2011). In fact, this narrow range could be an artifact of the small dynamic range of the samples (Heyer et al. 2009). Based on observations of the Galactic center (Oka et al. 2001) and starburst galaxies (e.g., Rosolowsky & Blitz 2005), Σ_{GMC} likely does vary with environment. Equation 11 implies that any such systematic changes in Σ_{GMC} may also lead to systematic changes in X_{CO} , though in actual starburst environments the picture is more complex than implied by Equation 11. Section 7 reviews the case of bright, dense starbursts in detail.

This calculation also implies a dependence of X_{CO} on the physical conditions in the GMC, density, and temperature. Combining Equations 8 and 9 with $M_{\text{vir}} \propto \rho R^3$, where ρ is the gas density, yields $\sigma \propto \rho^{-0.5}$. Meanwhile, because CO emission is optically thick, the observed luminosity depends on the brightness temperature, T_B , as well as the line width, so that $L_{\text{CO}} \propto \sigma T_B$. Substituting in the relationship between density and line width,

$$\alpha_{\text{CO}} \propto \frac{\rho^{0.5}}{T_B}. \quad (12)$$

The brightness temperature, T_B , depends on the excitation of the gas (Equation 6) and the filling fraction of emission in the telescope beam, f_b . For high density and optical depth the excitation temperature approaches the kinetic temperature. Under those conditions, Equation 12 also implies $\alpha_{\text{CO}} \propto \rho^{0.5} (f_b T_{\text{kin}})^{-1}$.

Thus, even for virialized GMCs we expect that the CO-to- H_2 conversion factor will depend on environmental parameters such as gas density and temperature. To some degree, these dependencies may offset each other. If denser clouds have higher star-formation activity and are consequently warmer, the opposite effects of ρ and T_B in Equation 12 may partially cancel, yielding a conversion factor that is closer to a constant than we might otherwise expect.

We also note that the relation between mass and luminosity expressed by Equation 10 is not exactly linear, which is the reason for the weak dependence of α_{CO} on L_{CO} or M_{mol} in Equation 11. As a consequence, even for GMCs that obey this simple picture, α_{CO} will depend (weakly) on the mass of the cloud considered, varying by a factor of approximately four over three orders of magnitude in cloud mass.

2.2. Galaxies

This simple picture for how the CO luminosity can be used to estimate masses of individual virialized clouds is not immediately applicable to entire galaxies. An argument along similar lines, however, can be laid out to suggest that under certain conditions there should be an approximate proportionality between the integrated CO luminosity of entire galaxies and their molecular mass. This is known as the mist model, for reasons that are made clear below. Following Dickman, Snell & Schloerb (1986), the luminosity due to an ensemble of nonoverlapping CO-emitting clouds is $L_{\text{CO}} \propto \sum_i a_i T_B(a_i) \sigma_i$, where a_i is the area subtended by cloud i , and $T_B(a_i)$ and σ_i are its brightness temperature and velocity dispersion, respectively. Under the assumption that

the brightness temperature is mostly independent of cloud size, and that there is a well-defined mean, T_B , then $T_B(a_i) \approx T_B$. We can rewrite the luminosity of the cloud ensemble as $L_{\text{CO}} \approx \sqrt{2\pi} T_B N_{\text{clouds}} \langle \pi R_i^2 \sigma(R_i) \rangle$, where the brackets indicate expectation value and N_{clouds} is the number of clouds within the beam, and we have used $a_i = \pi R_i^2$. Similarly, the total mass of gas inside the beam is $M_{\text{mol}} \approx N_{\text{clouds}} \langle 4/3 \pi R_i^3 \rho(R_i) \rangle$, where $\rho(R_i)$ is the volume density of a cloud of radius R_i . Using our definition from Equation 2 and dropping the i indices, it is then clear that

$$\alpha_{\text{CO}} \equiv \frac{M_{\text{mol}}}{L_{\text{CO}}} \approx \sqrt{\frac{8}{9\pi}} \frac{\langle R^3 \rho(R) \rangle}{T_B \langle R^2 \sigma(R) \rangle}. \quad (13)$$

If the individual clouds are virialized, they will follow Equation 8, or equivalently $\sigma = 0.0635 R \sqrt{\rho}$. Substituting into Equation 13 we find

$$\alpha_{\text{CO}} \propto \frac{\langle R^3 \rho \rangle}{T_B \langle R^3 \rho^{0.5} \rangle}, \quad (14)$$

which is analogous to Equation 12 (obtained for individual clouds). As Dickman, Snell & Schloerb (1986) discuss, it is possible to generalize this result if the clouds in a galaxy follow a size–line width relation and they have a known distribution of sizes. Assuming individually virialized clouds, and using the size–line width relation (Equation 9), we can rewrite Equation 13 as

$$\alpha_{\text{CO}} = 7.26 \frac{\sqrt{\Sigma_{\text{GMC}}} \langle R^2 \rangle}{T_B \langle R^{2.5} \rangle}, \quad (15)$$

where we have introduced the explicit dependence of the coefficient of the size–line width relation on the cloud surface density, Σ_{GMC} . This equation is the analog of Equation 11.

In the context of these calculations, CO works as a molecular mass tracer in galaxies because its intensity is proportional to the number of clouds in the beam, and because through virial equilibrium the contribution from each cloud to the total luminosity is approximately proportional to its mass, as discussed for individual GMCs. This is the essence of the mist model: Although each particle (cloud) is optically thick, the ensemble acts optically thin as long as the number density of particles is low enough for the clouds to avoid shadowing each other in spatial-spectral space.

Besides the critical assumption of nonoverlapping clouds, which could be violated in environments of very high density leading to optical depth problems that may render CO underluminous, the other key assumption in this model is the virialization of individual clouds, already discussed for GMCs in the Milky Way. The applicability of a uniform value of α_{CO} across galaxies relies on three assumptions that should be evident in Equation 15: a similar value for Σ_{GMC} , similar brightness temperatures for the CO emitting gas, and a similar distribution of GMC sizes that determines the ratio of the expectation values $\langle R^2 \rangle / \langle R^{2.5} \rangle$. Very little is known currently on the distribution of GMC sizes outside the Local Group (Blitz et al. 2007, Fukui & Kawamura 2010), and although this is a potential source of uncertainty, in practical terms this ratio is unlikely to be the dominant source of galaxy-to-galaxy variation in α_{CO} .

2.3. Other Sources of Velocity Dispersion

Because CO is optically thick, a crucial determinant of its luminosity is the velocity dispersion of the gas, σ . In our discussion for individual GMCs and ensembles of GMCs in galaxies, we have assumed that σ is ultimately determined by the sizes (through the size–line width relation) and virial masses of the clouds. It is especially interesting to explore what happens when the velocity dispersion of the CO emission is related to an underlying mass distribution that includes other components besides molecular gas. Following the reasoning by Downes, Solomon & Radford (1993) (see also Maloney & Black 1988, Downes & Solomon 1998) and the discussion in Section 2.1, we can write a cloud

luminosity L_{CO} relation for a fixed T_B as $L_{\text{CO}}^* = L_{\text{CO}}\sigma^*/\sigma$, where the asterisk indicates quantities where the velocity dispersion of the gas is increased by other mass components, such as stars. Assuming that both the molecular gas and the total velocity dispersion follow the virial velocity dispersion due to a uniform distribution of mass, $\sigma = \sqrt{GM^*/5R}$, then $L_{\text{CO}}^* = L_{\text{CO}}\sqrt{M^*/M_{\text{mol}}}$, where M^* represents the total mass within a radius R . Substituting $L_{\text{CO}} = M_{\text{mol}}/\alpha_{\text{CO}}$ yields the result $\alpha_{\text{CO}}L_{\text{CO}}^* = \sqrt{M_{\text{mol}}M^*}$.

Therefore, the straightforward application of α_{CO} to the observed luminosity L_{CO}^* yields an overestimate of the molecular gas mass, which in this simple reasoning is the harmonic mean of the real molecular mass and the total enclosed mass. If the observed velocity dispersion is more closely related to the circular velocity, as may be in the center of a galaxy, then $\sigma^* \approx \sqrt{GM^*/R}$ and the result of applying α_{CO} to L_{CO}^* will be an even larger overestimate of M_{mol} . The appropriate value of the CO-to- H_2 conversion factor to apply under these circumstances in order to correctly estimate the molecular mass is

$$\alpha_{\text{CO}}^* = \frac{M_{\text{mol}}}{L_{\text{CO}}^*} = \alpha_{\text{CO}} \sqrt{\frac{M_{\text{mol}}}{\mathcal{K}M^*}}, \quad (16)$$

where \mathcal{K} is a geometrical correction factor accounting for the differences in the distributions of the gas and the total mass, so that $\mathcal{K} \equiv (\sigma^*/\sigma)^2$. In the extreme case of a uniform distribution of gas responding to the potential of a rotating disk of stars in a galaxy center, $\mathcal{K} \sim 5$. Everything else being equal, in a case where $M^* \sim 10 M_{\text{mol}}$, the straight application of a standard α_{CO} in a galaxy center may lead to overestimating M_{mol} by a factor of about seven.

Note that for this correction to apply, the emission has to be optically thick throughout the medium. Otherwise any increase in line width is compensated for by a decrease in brightness, keeping the luminosity constant. Thus, this effect is only likely to manifest itself in regions that are already rich in molecular gas. Furthermore, it is possible to show that an ensemble of virialized clouds that experience cloud-cloud shadowing cannot explain a lower X_{CO} simply because there is a maximum attainable luminosity. Therefore we expect X_{CO} to drop in regions where the CO emission is extended throughout the medium and not confined to collections of individual self-gravitating molecular clouds. This situation is likely present in ULIRGs, where average gas volume densities are higher than the typical density of a GMC in the Milky Way, suggesting a pervading molecular ISM (e.g., Scoville, Yun & Bryant 1997). Indeed, the reduction of X_{CO} in mergers and galaxy centers has been modeled in detail by Shetty et al. (2011b) and Narayanan et al. (2011, 2012) and directly observed (see Sections 5.2, 5.3, 7.1, and 7.2).

2.4. Optically Thin Limit

Although commonly the emission from the $^{12}\text{CO } J = 1 \rightarrow 0$ transition is optically thick, under conditions such as highly turbulent gas motions or otherwise large velocity dispersions (for example, stellar outflows and perhaps also galaxy winds) emission may turn optically thin. Thus it is valuable to consider the optically thin limit on the value of the CO-to- H_2 conversion factor. Using Equation 5, the definition of optically thin emission $\{I_J = \tau_J[B_J(T_{\text{ex}}) - B_J(T_{\text{cmb}})]\}$, where B_J is the Planck function at the frequency ν_J of the $J \rightarrow J-1$ transition, T_{ex} is the excitation temperature, and T_{cmb} is the temperature of the cosmic microwave background, and the definition of antenna temperature T_J [$I_J = (2k\nu_J^2/c^2)T_J$], then the integrated intensity of the $J \rightarrow J-1$ transition can be written as

$$W(\text{CO}) = T_J \Delta v = \frac{8\pi^3 \nu_J}{3k} \mu^2 \frac{J}{g_J} f_{\text{cmb}} N_J. \quad (17)$$

The factor f_{cmb} accounts for the effect of the cosmic microwave background on the measured intensity, $f_{cmb} = 1 - (e^{bv_J/kT_{ex}} - 1)/(e^{bv_J/kT_{cmb}} - 1)$. Note that $f_{cmb} \sim 1$ for $T_{ex} \gg T_{cmb}$.

The column density of H_2 associated with this integrated intensity is simply $N(H_2) = \frac{1}{Z_{CO}} \sum_{J=0}^{\infty} N_J$, where Z_{CO} is the CO abundance relative to molecular hydrogen, $Z_{CO} = CO/H_2$. For a Milky Way gas phase carbon abundance, and assuming all gas-phase carbon is locked in CO molecules, $Z_{CO} \approx 3.2 \times 10^{-4}$ (Sofia et al. 2004). Note, however, that what matters is the integrated Z_{CO} along a line of sight, and CO may become optically thick well before this abundance is reached (for example, **Figure 1**). Indeed, Sheffer et al. (2008) analyze Z_{CO} in Milky Way lines of sight, finding a steep $Z_{CO} \approx 4.7 \times 10^{-6} [N(H_2)/10^{21} \text{ cm}^{-2}]^{2.07}$ for $N(H_2) > 2.5 \times 10^{20} \text{ cm}^{-2}$ with an order of magnitude scatter (see also Sonnentrucker et al. 2007).

When observations in only a couple of transitions are available, it is useful to assume local thermodynamic equilibrium (LTE) applies and that the system is described by a Boltzmann distribution with a single temperature. In that case, the column density is $N(CO) = Q(T_{ex}) e^{E_1/kT_{ex}} N_1/g_1$, where E_1 is the energy of the $J = 1$ state ($E_1/k \approx 5.53$ K for CO), and $Q(T_{ex}) = \sum_{J=0}^{\infty} g_J e^{-E_J/kT_{ex}}$ corresponds to the partition function at temperature T_{ex} , which can be approximated as $Q(T_{ex}) \sim 2kT_{ex}/E_1$ for rotational transitions when $T_{ex} \gg 5.5$ K (Penzias 1975; note this is accurate to $\sim 10\%$ even down to $T_{ex} \sim 8$ K). Using Equation 17, we can then write

$$X_{CO} = \frac{N(H_2)}{W(CO)} \approx \frac{1}{Z_{CO}} \frac{6b}{8\pi^3 \mu^2 f_{cmb} E_1/k} \left(\frac{T_{ex}}{E_1/k} \right) e^{\frac{E_1/k}{T_{ex}}}. \quad (18)$$

Consequently, adopting $Z_{CO} = 10^{-4}$ and using a representative $T_{ex} = 30$ K, we obtain

$$X_{CO} \approx 1.6 \times 10^{19} \frac{T_{ex}}{30 \text{ K}} e^{\frac{5.53 \text{ K}}{T_{ex}} - 0.184} \text{ cm}^{-2} (\text{K km s}^{-1})^{-1}, \quad (19)$$

or $\alpha_{CO} \approx 0.34 M_{\odot} (\text{K km s}^{-1} \text{ pc}^2)^{-1}$. These are an order of magnitude smaller than the typical values of X_{CO} and α_{CO} in the Milky Way disk, as we discuss in Section 4. Note that they are approximately linearly dependent on the assumed Z_{CO} and T_{ex} (for $T_{ex} \gg 5.53$ K). For a similar calculation that also includes an expression for non-LTE, see Papadopoulos et al. (2012).

2.5. Insights from Cloud Models

A key ingredient in further understanding X_{CO} in molecular clouds is the structure of molecular clouds themselves, which plays an important role in the radiative transfer. This is important both for the photodissociating and heating UV radiation and for the emergent intensity of the optically thick CO lines.

The CO $J = 1 \rightarrow 0$ transition arises well within the photodissociation region (PDR) in clouds associated with massive star formation, or even illuminated by the general diffuse ISRF (Maloney & Black 1988; Wolfire, Hollenbach & Tielens 1993). At those depths, gas heating is dominated by the grain photoelectric effect whereby stellar far-UV photons are absorbed by dust grains and eject a hot electron into the gas. The main parameter governing grain photoelectric heating is the ratio $\chi T_{kin}^{0.5}/n_e$, where χ is a measure of the far-UV field strength and n_e is the electron density. This process produces hotter gas and higher excitation in starburst galaxies. At the high densities of extreme starbursts, the gas temperature and CO excitation may also be enhanced by collisional coupling between gas and warm dust grains.

Early efforts to model the CO excitation and luminosity in molecular clouds using a large velocity gradient model were carried out by Goldreich & Kwan (1974). The CO luminosity–gas mass relation was investigated by Kutner & Leung (1985) using microturbulent models and by Wolfire, Hollenbach & Tielens (1993) using both microturbulent and macroturbulent models.

In microturbulent models, the gas has a (supersonic) isotropic turbulent velocity field with scales smaller than the photon mean free path. In the macroturbulent case, the scale size of the turbulence is much larger than the photon mean free path, and the emission arises from separate Doppler-shifted-emitting elements. Microturbulent models produce a wide range of CO $J = 1 \rightarrow 0$ profile shapes, including centrally peaked, flat topped, and severely centrally self-reversed, whereas most observed line profiles are centrally peaked. Macroturbulent models, however, only produce centrally peaked profiles if there are a sufficient number of clumps within the beam with densities $n \gtrsim 10^3 \text{ cm}^{-3}$ in order to provide the peak brightness temperature. Falgarone et al. (1994) demonstrated that a turbulent velocity field can produce both peaked and smooth line profiles, and they are much closer to observations than macroturbulent models.

Wolfire, Hollenbach & Tielens (1993) use PDR models in which the chemistry and thermal balance were calculated self-consistently as a function of depth into the cloud. The microturbulent PDR models are very successful in matching and predicting the intensity of low- J CO lines and the emission from many other atomic and molecular species (Hollenbach & Tielens 1997, 1999). For example, the nearly constant ratio of $[\text{CII}]/\text{CO } J = 1 \rightarrow 0$ observed in both Galactic and extragalactic sources (Crawford et al. 1985, Stacey et al. 1991) was first explained by PDR models as arising from high-density ($n \gtrsim 10^3 \text{ cm}^{-3}$) and high-UV field ($\chi \gtrsim 10^3$) sources in which both the $[\text{CII}]$ and CO are emitted from the same PDR regions in molecular cloud surfaces. These models show that the dependence on CO luminosity with incident radiation field is weak. This is because as the field increases, the $\tau_{\text{CO}} = 1$ surface is driven deeper into the cloud, where the dominant heating process, grain photoelectric heating, is weaker. Thus, the dissociation of CO in higher fields regulates the temperature where $\tau_{\text{CO}} = 1$.

PDR models have the advantage that they calculate the thermal and chemical structure in great detail, so that the gas temperature is determined where the CO line becomes optically thick. We note, however, that although model gas temperatures for the CO $J = 1 \rightarrow 0$ line are consistent with observations, the model temperatures are typically too cool to match the observed high- J CO line emission (e.g., Habart et al. 2010). The model density structure is generally simple (constant density or constant pressure), and the velocity is generally considered to be a constant based on a single microturbulent velocity. More recent dynamical models combine chemical and thermal calculations with full hydrodynamic simulations.

3. A MODERN THEORETICAL PERSPECTIVE

In recent years, there has been much progress in updating PDR models. There has also been progress in combining hydrodynamic simulations, chemical modeling, and radiation transfer codes.

3.1. Photodissociation Regions

Because CO production mainly occurs through ion-neutral chemistry (van Dishoeck & Black 1988), the ionization structure through the PDR is important in setting the depth of the CO formation. Recombination of metal ions on polycyclic aromatic hydrocarbons (PAHs) can modify the abundance of free electrons. For a typical GMC with $n \sim 10^3 \text{ cm}^{-3}$ illuminated by a radiation field ~ 10 times the strength of the Galactic interstellar radiation field (ISRF) in the vicinity of the Sun, the $\tau_{\text{CO}} = 1$ surface is at a depth of $A_V \sim 1$ when PAHs are included. Without PAHs the electron abundance stays high, and the ion-neutral chemistry is slowed due to H_3^+ recombination. Consequently, the $\tau_{\text{CO}} = 1$ surface is pushed deeper into the cloud ($A_V \sim 2$). The PAH rates are estimated by Wolfire et al. (2008) by considering the C^0/C^+ ratio in diffuse lines of sight, but

there is considerable uncertainty both in the rates (Liszt 2011) and in the PAH abundance and their variation with cloud depth.

Bell et al. (2006) carry out a parameter study of X_{CO} using PDR models with constant microturbulent line width. The calculated X_{CO} versus A_V plots have a characteristic shape with high X_{CO} at low A_V , dropping to a minimum value at $A_V \sim 2\text{--}4$ and then slowly rising for increasing A_V . The X_{CO} dependence at low A_V arises from molecular gas with low CO abundance. After the CO line intensity becomes optically thick, X_{CO} slowly rises again as $N(\text{H}_2)$ increases. Increasing density up to the critical density of CO $J = 1 \rightarrow 0$ [$n(\text{H}_2)_{\text{cr},1} \sim 2200 \text{ cm}^{-3}$] enhances the CO excitation and causes X_{CO} to drop. In addition, the minimum moves closer to the cloud surface as does the $\tau_{\text{CO}} = 1$ surface. An increase in X_{CO} by a factor of more than 100 is found when decreasing dust and metallicity to 1% of the local Galactic ISM, reflecting the larger column of H_2 at a given A_V . Bell, Viti & Williams (2007) suggest that the appropriate X_{CO} value to use in various extragalactic environments can be estimated from the minimum in the X_{CO} versus A_V plot.

Wolfire, Hollenbach & McKee (2010) use an updated version of their own PDR models, including a self-consistent calculation for the median density expected from a turbulent density distribution. The models provide a theoretical basis for predicting the molecular mass fraction outside of the CO-emitting region in terms of incident radiation field and gas metallicity. They assume that the median density is given by $\langle n \rangle_{\text{med}} = \bar{n} \exp(\mu)$, where \bar{n} is the volume-averaged density distribution $\bar{n} \propto 1/r$, and $\mu = 0.5 \ln(1 + 0.25\mathcal{M}^2)$ (Padoan, Jones & Nordlund 1997). The sound speed that enters in the Mach number, \mathcal{M} , is calculated from the PDR model output while the turbulent velocity is given by the size–line width relation (Equation 9).

3.2. Numerical Simulations

As an alternative to PDR models with simple geometries and densities, hydrodynamical models can be used to calculate the line width and density but with only limited spatial resolution and approximate chemistry and thermal balance. Glover & Mac Low (2007a,b) carry out simulations of the formation of molecular clouds using a modified version of the magnetohydrodynamical code ZEUS-MP. They include a time-dependent chemistry, in particular for H_2 formation and destruction, and thermal balance. Glover et al. (2010) enhance the code to account for CO chemistry in a turbulent GMC. A turbulent picture of a GMC is not one with well-defined clumps surrounded by an interclump medium but one with a continuous density distribution and constant mixing between low- and high-density regions. The CO abundance varies within the cloud depending on the gas density and penetration of the dissociating radiation field. Calculations of X_{CO} are carried out by Glover & Mac Low (2011) and Shetty et al. (2011a,b). Shetty and colleagues include non-LTE CO excitation and line transfer in the LVG approximation. These researchers carry out 3D turbulent simulations in a box of fixed size (20 pc) as well as simulations of turbulence generated with uniform power between wave numbers $1 \leq k \leq 2$ but with various initial densities and metallicities. For their standard cloud model, the saturation amplitude of the 1D velocity dispersion is 2.4 km s^{-1} . Each line of sight has different CO intensity as well as CO and H_2 column density, depending on the past and present physical conditions along it. Thus, for a given $N(\text{H}_2)$ there is a range in X_{CO} values (see Shetty et al. 2011a, their figures 5 and 6). The dispersion generally increases for clouds with lower density and lower metallicity.

Shetty et al. (2011a) show in their figure 7 the calculated mean X_{CO} in different A_V bins for several initial densities and metallicities. The variation in X_{CO} with A_V is qualitatively similar to that shown in Bell et al. (2006) for microturbulent models. Lower densities and metallicities drive X_{CO} to higher values due to lower CO excitation and CO/ H_2 ratios, respectively. At $A_V \gtrsim 7$ the models with different initial densities converge as the CO line becomes optically thick. The

minimum in X_{CO} occurs at larger A_V in the hydrodynamic simulations compared to the one-sided PDR models, likely due to the dissociating radiation incident on all sides of the box and due to its greater penetration along low-density lines of sight. A range in density $n = 100\text{--}1,000\text{ cm}^{-3}$ and metallicity $Z = 0.1\text{--}1\text{ }Z_{\odot}$ produces a range of only $X_{\text{CO},20} \sim 2\text{--}10$. Thus, although there can be large variations in X_{CO} along different lines of sight in the cloud, the emission-weighted X_{CO} is close to the typical Galactic value (Section 4). In addition, the low-metallicity case has higher X_{CO} at low A_V but approaches the Galactic value for higher density (higher A_V) lines of sight. Although the models were run with constant box size, the dependence on A_V suggests that clouds of sufficiently small size such that CO does not become optically thick have higher X_{CO} . The results seem to confirm the suggestion by Bell et al. (2006) that the mean X_{CO} value should be near the minimum when plotted as X_{CO} versus A_V .

Shetty et al. (2011b) investigate the results of varying the temperature, CO abundance, and turbulent line width. They find only a weak dependence on temperature with $X_{\text{CO}} \propto T_{\text{kin}}^{-0.5}$ for $20\text{ K} < T_{\text{kin}} < 100\text{ K}$, and thus over the range of temperatures typically found in Galactic clouds X_{CO} is not expected to vary significantly due to temperature. At low (fixed) CO abundance ($n_{\text{CO}}/n_{\text{H}_2} \sim 10^{-6}$), the line does not become optically thick, and thus $W(\text{CO})$ follows $N(\text{H}_2)$ with constant X_{CO} up to at least $\log N(\text{H}_2) = 22.5$. Varying the turbulent line width increases the CO line intensity as expected because decreasing the self-absorption allows more CO line emission to escape the cloud. They also find, however, a decreasing brightness temperature and, over the range of velocity dispersion $\sigma = 2\text{--}20\text{ km s}^{-1}$, $W(\text{CO})$ changes as $W(\text{CO}) \propto \sigma^{0.5}$ instead of changing linearly. The higher turbulent velocities create dense shocks but also larger voids of low-density material. The competing effects produce a dependence on σ that is slower than linear. Increasing the column density as well as the line width might produce a model result closer to $W(\text{CO}) \propto \sigma$.

An interesting result is that X_{CO} is not sensitive to the internal velocity profile within the cloud but only to the total line width, however that might be generated. A cloud need not obey a power-law size–line width relation to have the same X_{CO} as one with a Gaussian distribution and identical dispersion velocity. Thus, clouds need not be virialized nor obey a size–line width relation to have the same X_{CO} . The modeled X_{CO} converges for high A_V clouds, thus the X_{CO} factor is not expected to vary from cloud to cloud as long as there is a large enough column density. Shetty et al. (2011b) conclude that a nearly constant X_{CO} is the result of the limited range in column densities, temperatures, and line widths found in Galactic molecular clouds and that applying a constant X_{CO} is approximately correct to within a factor of approximately two.

Global models of X_{CO} using hydrodynamic simulations to investigate the variation due to galactic environment are carried out by Feldmann, Gnedin & Kravtsov (2012) and Narayanan et al. (2011, 2012). A significant problem in numerical simulations is how to handle the physical conditions and/or line emission within regions smaller than the spatial grid. Feldmann, Gnedin & Kravtsov (2012) use high-resolution ($\sim 0.1\text{ pc}$) simulations from Glover & Mac Low (2011) for sub-grid solutions to cosmological simulations of 60-pc resolution. These models used constant $T_{\text{kin}} = 10\text{ K}$, LTE excitation for CO, with either constant CO line width or one proportional to $\Sigma_{\text{mol}}^{0.5}$. By comparing results at their highest resolutions with those at 1 kpc and 4 kpc, Glover & Mac Low assess the effects of spatial averaging on X_{CO} . The averaging tends to reduce the variation of X_{CO} on $N(\text{H}_2)$ and UV radiation field intensity. At greater than kiloparsec scales, and H_2 column densities between 10^{21} cm^{-2} and 10^{23} cm^{-2} , X_{CO} changes by only a factor of two. They find essentially no variation in X_{CO} with UV field strength between 0.1 and 100 times the Galactic ISRF. Feldmann, Gnedin & Kravtsov (2012) do find a significant variation with metallicity, with a scaling $X_{\text{CO}} \propto Z^{-0.5}$ for virial line widths. Note that this relation is much shallower than found by, for example, Genzel et al. (2012; see also Section 8.2). The researchers suggest that low-metallicity high-redshift galaxies may not obey the same gas surface density to star-formation relation observed in local disks.

The results of Narayanan et al. (2011, 2012) are discussed in Section 7.2. Here we note that their effective resolution of ~ 70 pc requires adopting subgrid cloud properties. Although the surfaces of GMCs more massive than $\sim 7 \times 10^5 M_\odot$ are resolved, their internal structure is not. The resulting line and continuum transfer, and temperature and chemical structure, can only be approximate. The resolution problem also enters in simulations of individual clouds. We showed in Section 1 that CO becomes optically thick within a column $N(\text{H}_2) \approx 2\text{--}3 \times 10^{20} \text{ cm}^{-2}$. Thus, for subparsec resolution (~ 0.1 pc) and density greater than $n \gtrsim 10^3 \text{ cm}^{-3}$, the physical conditions (temperature, density, and abundances) are averaged over the line-forming region and the calculated emitted intensity can be in error. The resolution problem is much more severe for H_2 dissociation. Self-shielding of H_2 starts within a column of only $N(\text{H}_2) \sim 10^{14} \text{ cm}^{-2}$ (de Jong, Boland & Dalgarno 1980). Thus, with a resolution of ~ 0.1 pc and density of $n \gtrsim 10 \text{ cm}^{-3}$, the optical depth to dissociating radiation is already $\tau \gtrsim 10^4$ in a resolution element. A complementary approach is to apply a state-of-the-art PDR code with well-resolved H_2 formation to the output of hydrodynamic simulations (Levrier et al. 2012). With increasing computing power the issues of resolution will continue to improve. We suggest that high priority should be placed on creating large-scale galactic simulations that are well matched to small-scale simulations with resolved cloud structure. The former provide environmental conditions and cloud boundary conditions while the latter provide the chemistry and line emission in a realistic turbulent cloud. Expanding the library of GMC models with a range of column densities, line widths, and external heating, and thoroughly checking them against observations, would be most helpful.

4. X_{CO} IN THE MILKY WAY

The Galaxy is the only source where it is possible to determine the CO-to- H_2 conversion factor in a variety of ways. It thus provides the prime laboratory to investigate the calibration and the variations of the proportionality between CO emission and molecular mass.

In the following sections we discuss three types of X_{CO} determinations: (*a*) employing virial masses, a technique that requires the ability to spatially resolve molecular clouds to measure their sizes and kinematics; (*b*) taking advantage of optically thin tracers of column density, such as dust or certain molecular and atomic lines; and (*a*) using the diffuse γ -ray emission arising from the pion production process that takes place when cosmic rays interact with ISM protons. Gamma-ray techniques are severely limited by sensitivity and are only applicable to the Milky Way and the Magellanic Clouds. The good level of agreement between these approaches in our own Galaxy is the foundation of the use of the CO-to- H_2 conversion factor in other galaxies.

4.1. X_{CO} Based on Virial Techniques

The application of the virial theorem to molecular clouds has been discussed by a number of researchers, and recently reviewed by McKee & Ostriker (2007). Here, we just briefly summarize the fundamental points. The virial theorem can be expressed in the Lagrangian (fixed mass) or Eulerian (fixed volume) forms, the latter particularly applicable to turbulent clouds, where mass is constantly exchanged with the surrounding medium. In the somewhat simpler Lagrangian form, the virial equilibrium equation is

$$2(K - K_s) + B + W = 0, \quad (20)$$

where K is the volume integral of the thermal plus kinetic energy, K_s is the surface pressure term, B is the net magnetic energy including volume and surface terms (which cancel for a completely uniform magnetic field), and W is the net gravitational energy, which is determined by the

self-generated gravitational potential if the acceleration due to mass external to the cloud can be neglected. In the simple case of a uniform, unmagnetized sphere, virial equilibrium implies $2K + W = 0$. It is useful to define the virial parameter, a_{vir} , which corresponds to the ratio of total kinetic energy to gravitational energy (Bertoldi & McKee 1992), so that $a_{\text{vir}} \equiv 5 R \sigma^2 / GM$.

4.1.1. Are clouds virialized? In this context, gravitationally bound objects have $a_{\text{vir}} \simeq 1$. Whether interstellar clouds are entities in virial equilibrium, even in a time or ensemble-averaged sense (McKee 1999), is a matter of current debate. Observational evidence can be interpreted in terms of systems out of equilibrium with rapid star formation and subsequent disruption in a few million years (e.g., Elmegreen 2000), an evolutionary progression and a typical lifetime of a few tens of millions of years, long enough for clouds to become virialized (e.g., Blitz & Shu 1980, Fukui & Kawamura 2010), or a lifetime of hundreds of millions of years (e.g., Scoville & Hersch 1979). Roman-Duval et al. (2010) find a median $a_{\text{vir}} \approx 0.5$ for clouds in the inner Galaxy, suggesting that they are bound entities where M_{vir} represents a reasonable measure of the molecular mass, although casting doubt on the assumption of exact virial equilibrium. Wong et al. (2011) estimate a very large scatter in a_{vir} in the Large Magellanic Cloud, but do lack an independent mass tracer so their results rest on the assumption of a fixed X_{CO} . Observations in the outer Galaxy show another angle of the situation. Heyer, Carpenter & Snell (2001) find that clouds with $M_{\text{mol}} > 10^4 M_{\odot}$ are self-gravitating, whereas small clouds with masses $M_{\text{mol}} < 10^3 M_{\odot}$ are overpressured with respect to their self-gravity; that is, they have $a_{\text{vir}} \gg 1$ and are out of equilibrium. Given the observed mass function, however, such clouds represent a very small fraction of the molecular mass of the Milky Way.

In any case, observed GMC properties can be understood as a consequence of approximate energy equipartition, which observationally is very difficult to distinguish from virial equilibrium (Ballesteros-Paredes 2006). Clouds with an excess of kinetic energy, $a_{\text{vir}} \gg 1$, perhaps due to ongoing star formation or supernovae, would be rapidly dissipated, whereas clouds with a dearth of kinetic energy, $a_{\text{vir}} \ll 1$, would collapse at the free-fall velocity, which is within 40% of the equipartition velocity dispersion and challenging to distinguish from turbulent motions in observations. Furthermore, the resulting star formation will inject energy into the cloud acting to restore the balance. Thus from the standpoint of determining cloud masses over large samples, the assumption of virial equilibrium, even if not strictly correct, is unlikely to be very wrong.

4.1.2. Observational results. The most significant study of the relation between virial mass and L_{CO} (the mass-luminosity relation) in the Milky Way is that conducted by Solomon et al. (1987), which encompasses 273 clouds and spans several orders of magnitude in cloud luminosity and mass. It is dominated by clouds located in the inner Galaxy, in the region of the so-called Molecular Ring, a feature in the molecular surface density of the Milky Way peaking at $R_{\text{GC}} \approx 4$ kpc galactocentric radius. It uses kinematic distances with an old value of the distance to the Galactic Center, $R_{\odot} = 10$ kpc. We report new fits after a 0.85 scaling in all distances and sizes and 0.72 in luminosities to bring them into agreement with the modern distance scale ($R_{\odot} = 8.5$ kpc). The virial mass computations assume $\rho(r) \propto r^{-1}$ (see Section 2.1).

Solomon et al. (1987) find a very strong correlation between M_{vir} and L_{CO} , such that $M_{\text{vir}} = 37.9 L_{\text{CO}}^{0.82}$ with a typical dispersion of 0.11 dex for M_{vir} . Note the excellent agreement with the expected mass-luminosity relation in Equation 10 using a typical CO brightness temperature of $T_B \approx 4$ K (Maloney 1990). For a cloud at their approximate median luminosity, $L_{\text{CO}} \approx 10^5 \text{ K km s}^{-1} \text{ pc}^2$, this yields $\alpha_{\text{CO}} = 4.6 M_{\odot} (\text{K km s}^{-1} \text{ pc}^2)^{-1}$ and $X_{\text{CO},20} = 2.1$. Because the relation is not strictly linear α_{CO} will change by $\sim 60\%$ for an order of magnitude change in

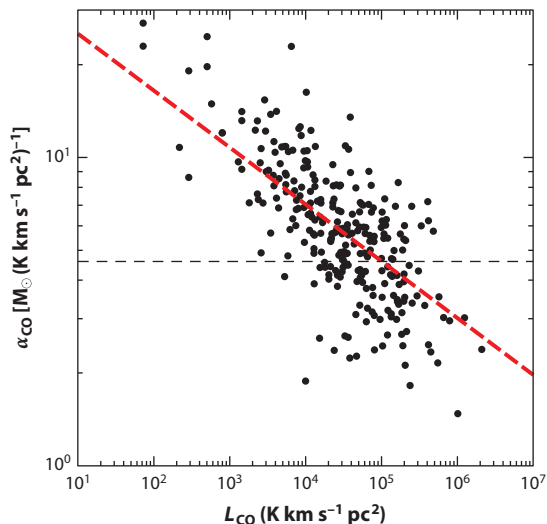


Figure 2

Relation between virial α_{CO} and CO luminosity for giant molecular clouds in the Milky Way (Solomon et al. 1987). We have corrected the numbers in the original table to reflect the updated distance to the Galactic Center of 8.5 kpc. The dependence of α_{CO} on L_{CO} arises from the fact that the correlation between M_{vir} and L_{CO} has a nonlinear slope ($M_{\text{vir}} \propto L_{\text{CO}}^{0.815 \pm 0.013}$), following the expectations from Equation 10 for approximately constant brightness temperature. This results in $\alpha_{\text{CO}} \approx 4.61(L_{\text{CO}}/10^5)^{-0.185}$, denoted by the red thick dashed line (the dispersion around this relation is ± 0.15 dex). The nominal value at $L_{\text{CO}} = 10^5 \text{ K km s}^{-1} \text{ pc}^2$ is illustrated by the black thin dashed line.

luminosity (**Figure 2**). Therefore, GMCs with lower luminosities (and masses) will have somewhat larger mass-to-light ratios and conversion factors than more luminous GMCs.

Independent analysis using the same survey by Scoville et al. (1987) yields a very similar mass-luminosity relation. After accounting for the different coefficients used for the calculation of the virial mass, the relation is $M_{\text{vir}} = 33.5 L_{\text{CO}}^{0.85}$. For an $L_{\text{CO}} \approx 10^5 \text{ K km s}^{-1} \text{ pc}^2$ cloud this yields $\alpha_{\text{CO}} = 6.0 M_{\odot} (\text{K km s}^{-1} \text{ pc}^2)^{-1}$ and $X_{\text{CO},20} = 2.8$ (this work uses $R_{\odot} = 8.5 \text{ kpc}$). Interestingly, there is no substantial difference in the mass-luminosity relation for GMCs with or without HII regions (Scoville & Good 1989), although the latter tend to be smaller and of lower mass, and have on average half of the velocity-integrated CO brightness of their strongly star-forming counterparts. The resulting difference in T_B could have led to a displacement in the relation, according to the simple reasoning leading to Equation 10, but it appears not to be significant.

4.1.3. Considerations and limitations. Besides the already discussed applicability of the virial theorem, there are a number of limitations to virial studies. Some are practical, whereas others are fundamental to the virial technique. On the practical side, virial studies are sensitive to cloud definitions and biases induced by signal-to-noise ratios. These impact the values of both R and σ used to compute the mass. In noise-free measurements isolated cloud boundaries would be defined using contours of zero emission, when in reality it is necessary to define them using a higher contour [for example, Solomon et al. (1987) use a $T_B \sim 4 \text{ K}$ CO brightness contour]. Scoville et al. (1987) discuss the impact of this correction, studying the curve of growth for R and σ as the definition contour is changed in high signal-to-noise observations. Moreover, isolated clouds are rare and it is commonly necessary to disentangle many partially blended features along

the line of sight. To measure a size, clouds need to be resolved, and if appropriate the telescope beam size needs to be deconvolved to establish the intrinsic cloud size. This is a major concern in extragalactic studies, but even Galactic data sets are frequently undersampled, which affects the reliability of the R and L_{CO} determinations. Given these considerations, it is encouraging that two comprehensive studies using independent analyses of the same survey come to values of α_{CO} that differ by only $\sim 30\%$ for clouds of the same luminosity.

A fundamental limitation of the virial technique is that CO needs to accurately sample the full potential and size of the cloud. For example, if because of photodissociation or other chemistry CO is either weak or absent from certain regions, its velocity dispersion may not accurately reflect the mass of the cloud. This is a particular concern for virial measurements in low-metallicity regions (see Section 6), although most likely it is not a limitation in the aforementioned determinations of X_{CO} in the inner Galaxy.

4.2. Column Density Determinations Using Dust and Optically Thin Lines

Perhaps the most direct approach to determining the H_2 column density is to employ an optically thin tracer. This tracer can be a transition of a rare CO isotopologue or other chemical species (e.g., for CH, see Magnani et al. 2003). It can also be dust, usually optically thin in emission at FIR wavelengths, and used in absorption through stellar extinction studies.

4.2.1. CO isotopologues. A commonly used isotopologue is ^{13}CO . Its abundance relative to ^{12}CO is down by a factor approaching the $^{12}\text{C}/^{13}\text{C} \approx 69$ isotopic ratio at the Solar Circle ($^{12}\text{C}/^{13}\text{C} \approx 50$ at $R_{\text{GC}} \approx 4$ kpc, the galactocentric radius of the Molecular Ring) as long as chemical fractionation and selective photodissociation effects can be neglected (Wilson 1999). Given this abundance ratio and under the conditions in a dark molecular cloud, ^{13}CO emission may not always be optically thin, as $\tau_1 \sim 1$ requires $A_V \sim 5$.

The procedure consists of inverting the observed intensity of the optically thin tracer to obtain its column (or surface) density. In the case of isotopologues, this column density is converted to the density of CO using the (approximate) isotopic ratio. Inverting the observed intensity requires knowing the density and temperature structure along the line of sight, which is a difficult problem. If many rotational transitions of the same isotopologue are observed, it is possible to model the line-of-sight column density using a number of density and temperature components. In practice, an approximation commonly used is LTE, the assumption that a single excitation temperature describes the population distribution among the possible levels along the line of sight. It is also frequently assumed that ^{12}CO and ^{13}CO share the same T_{ex} , which is particularly justifiable if collisions dominate the excitation ($T_{\text{ex}} = T_{\text{kin}}$, the kinetic temperature of the gas). Commonly used expressions for determining $N(^{13}\text{CO})$ under these assumptions can be found in, for example, Pineda et al. (2010b). Note, however, that if radiative trapping plays an important role in the excitation of ^{12}CO , T_{ex} for ^{13}CO will generally be lower due to its reduced optical depth (e.g., Scoville & Sanders 1987).

Dickman (1978) characterized the CO column density in over 100 lines of sight toward 38 dark clouds, focusing on regions where the LTE assumption is unlikely to introduce large errors. The combination of LTE column densities with estimates of A_V performed using star counts yields $A_V \approx (4.0 \pm 2.0) \times 10^{-16} N(^{13}\text{CO}) \text{ cm}^2 \text{ mag}$. Comparable results were obtained in detailed studies of Taurus by Frerking, Langer & Wilson (1982; note the nonlinearity in their expression) and Perseus by Pineda, Caselli & Goodman (2008), the latter using a sophisticated extinction determination (Lombardi & Alves 2001). Extinction can be converted into molecular column density through the assumption of an effective gas-to-dust ratio. Bohlin, Savage & Drake (1978)

determined a relation between column density and reddening (selective extinction), such that $[N(\text{H I}) + 2N(\text{H}_2)]/E(B - V) \approx 5.8 \times 10^{21} \text{ atoms cm}^{-2} \text{ mag}^{-1}$ in a survey of interstellar Ly α absorption carried out using the *Copernicus* satellite toward 75 lines of sight, mostly dominated by H I. For a standard Galactic interstellar extinction curve with $R_V \equiv A_V/E(B - V) = 3.1$, this results in

$$N_H \equiv N(\text{H I}) + 2N(\text{H}_2) \approx 1.9 \times 10^{21} \text{ cm}^{-2} A_V. \quad (21)$$

A much more recent study using *Far Ultraviolet Spectroscopic Explorer* observations finds essentially the same relation (Rachford et al. 2009). In high surface density molecular gas R_V may be closer to 5.5 (Chapman et al. 2009), and Equation 21 may yield a 40% overestimate (Evans et al. 2009). Using Equation 21, the approximate relation between $^{13}\text{CO } J = 1 \rightarrow 0$ and molecular column density is $N(\text{H}_2) \approx 3.8 \times 10^5 N(^{13}\text{CO})$. Pineda, Caselli & Goodman (2008) find a similar result in a detailed study of Perseus, with an increased scatter for $A_V \gtrsim 5$. Goldsmith et al. (2008) use these results together with an averaging method to increase the dynamic range of their ^{13}CO and ^{12}CO data, a physically motivated variable $^{12}\text{CO}/^{13}\text{CO}$ ratio, and a large velocity gradient excitation analysis, to determine H_2 column densities in Taurus. They find that $X_{\text{CO},20} \approx 1.8$ recovers the molecular mass over the entire region mapped while there is a marked increase in the region of low column density, where X_{CO} increases by a factor of five where $N(\text{H}_2) < 10^{21} \text{ cm}^{-2}$. As a cautionary note about the blind use of ^{13}CO LTE estimates, however, Heiderman et al. (2010) find that this relation between H_2 and ^{13}CO underestimates $N(\text{H}_2)$ by factors of four to five compared with extinction-based results in the Perseus and Ophiuchus molecular clouds.

4.2.2. Extinction mapping. Extinction mapping by itself can be directly employed to determine X_{CO} . It fundamentally relies on the assumption of spatially uniform extinction properties for the bands employed, and on the applicability of Equation 21 to convert extinction into column density.

Frerking, Langer & Wilson (1982) determined $X_{\text{CO},20} \approx 1.8$ in the range of $4 \lesssim A_V \lesssim 12$ in ρ Oph, whereas the same researchers found constant $W(\text{CO})$ for $A_V \gtrsim 2$ in Taurus. Lombardi, Alves & Lada (2006) studied the Pipe Nebula and found a best fit X_{CO} in the range of $X_{\text{CO},20} \approx 2.9\text{--}4.2$, but only for K-band extinctions $A_K > 0.2$ (equivalent to $A_V > 1.8$; Rieke & Lebofsky 1985). A simple fit to the data ignoring this nonlinearity yields $X_{\text{CO},20} \sim 2.5$. The Pineda, Caselli & Goodman (2008) study of Perseus finds $X_{\text{CO},20} \approx 0.9\text{--}3$ over a number of regions. The relation between CO and H_2 , however, is mostly linear for $A_V \lesssim 4$, becoming saturated at larger line-of-sight extinctions.

Pineda et al. (2010b) extend the aforementioned Goldsmith et al. (2008) study of Taurus by characterizing the relation between reddening (from the Two Micron All Sky Survey, 2MASS) and CO column density (derived from ^{13}CO) to measure $X_{\text{CO},20} \approx 2.1$. They find that the relation between A_V and CO flattens for $A_V \gtrsim 10$ (Figure 3), a fact that they attribute to freeze-out of CO onto dust grains causing the formation of CO and CO_2 ice mantles. Including a correction for this effect results in a linear relation to $A_V \gtrsim 23$. For $A_V \lesssim 3$ the column density of CO falls below the linear relationship, likely due to the effects of photodissociation and chemical fractionation. Along similar lines, Heiderman et al. (2010) find that in Ophiuchus and Perseus CO can underpredict H_2 with respect to A_V for $\Sigma_{\text{mol}} > 200 M_\odot \text{ pc}^{-2}$ by as much as $\sim 30\%$.

Paradis et al. (2012) recently used a high-latitude extinction map derived from 2MASS data using an extension of the NICER methodology (Dobashi et al. 2008, 2009) to derive X_{CO} in a sample of nearby clouds with $|b| > 10^\circ$. They find $X_{\text{CO},20} \approx 1.67 \pm 0.08$ with a somewhat higher value $X_{\text{CO},20} \approx 2.28 \pm 0.11$ for the inner Galaxy region where $|l| < 70^\circ$. They report an excess in extinction over the linear correlation between total gas and A_V at $0.2 \lesssim A_V \lesssim 1.5$, which is

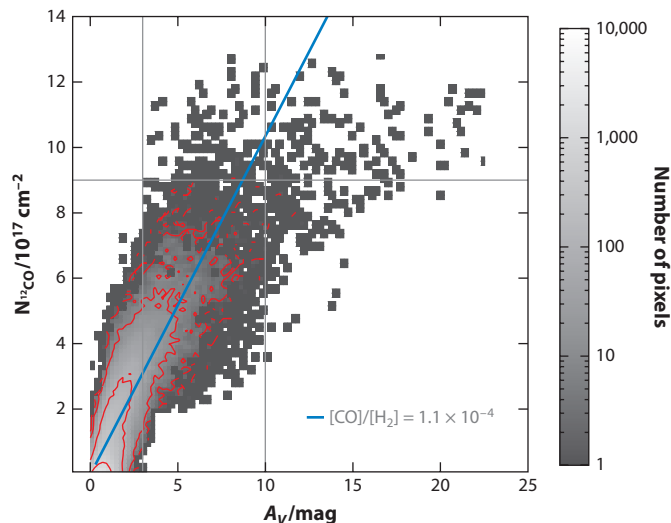


Figure 3

Relation between CO column density and extinction in the Taurus molecular cloud (Pineda et al. 2010b). The figure shows the pixel-by-pixel relation between gas-phase CO column density (obtained from ^{13}CO) and A_V . The blue line illustrates the average linear relation for $3 \lesssim A_V \lesssim 10$, $N(^{12}\text{CO}) \approx 1.01 \times 10^{17} A_V \text{ cm}^{-2}$ (implying $\text{CO}/\text{H}_2 \approx 1.1 \times 10^{-4}$ for the assumed isotopic ratio). The linearity is clearly broken for $A_V \gtrsim 10$. Pineda et al. (2010b) show that linearity is restored to high A_V after applying a correction for CO freeze-out into dust grain mantles.

suggestive of a gas phase that is not well traced by either 21-cm or CO emission. We return to this in Section 4.2.4.

4.2.3. Dust emission. The use of extinction mapping to study $N(\text{H}_2)$ is mostly limited to nearby Galactic clouds because it needs a background stellar distribution, minimal foreground confusion, and the ability to resolve individual stars to determine their reddening. Most interestingly, the FIR emission from dust can also be employed to map the gas distribution. Indeed, dust is an extraordinarily egalitarian acceptor of UV and optical photons, indiscriminately processing them and reemitting in the FIR. In principle, the dust spectral energy distribution can be modeled to obtain its optical depth, $\tau_d(\lambda)$, which should be proportional to the total gas column density under the assumption of approximately constant dust emissivity per gas nucleon, fundamentally the product of the gas-to-dust ratio and dust optical properties.

How valid is this assumption? An analysis of the correlation between τ_d and HI was carried out at high Galactic latitudes by Boulanger et al. (1996), who found a typical dust emissivity per H nucleon of

$$\delta_{\text{DGR}} \equiv \tau_d / N_H \approx 1.0 \times 10^{-25} (\lambda / 250 \mu\text{m})^{-\beta} \text{ cm}^2, \quad (22)$$

with $\beta = 2$, in excellent accord with the recent value for high-latitude gas derived using *Planck* observations (Planck Collaboration XXIV et al. 2011, who prefer $\beta = 1.8$). They also identified a break in the correlation for $N(\text{HI}) \gtrsim 5 \times 10^{20} \text{ cm}^{-2}$, which is suggestive of an increasingly important contribution from H_2 to N_H , in agreement with results from *Copernicus* (Savage et al. 1977). There is evidence that the coefficient in Equation 22 changes in molecular gas. It may increase by factors of two to three at very high column densities (Schnee et al. 2008, Flagey et al. 2009, Planck Collaboration XXV et al. 2011), likely due to grain growth or perhaps solid-state

effects at low temperatures (e.g., Mény et al. 2007). Note, however, that recent work using *Planck* in the Galactic plane finds $\delta_{\text{DGR}} \approx (0.92 \pm 0.05) \times 10^{-25} \text{ cm}^2$ at $250 \mu\text{m}$, with no significant variation with Galactic radius (Planck Collaboration XXI et al. 2011). This δ_{DGR} is almost identical to that observed in dust mixed with mostly atomic gas at high latitudes, suggesting that the aforementioned emissivity variations are very localized.

This excellent correlation between τ_d and N_{H} is the basis for a number of studies that use dust emission to determine H_2 column densities. Most notably, Dame, Hartmann & Thaddeus (2001) employed the Columbia survey of molecular gas in the Galactic plane together with the Dwingeloo-Leiden HI survey and the *Infrared Astronomical Satellite* (IRAS) temperature-corrected $100\text{-}\mu\text{m}$ spectral density map by Schlegel, Finkbeiner & Davis (1998). With these data, $N(\text{H}_2)$ can be obtained using

$$N(\text{H}_2) = [\tau_d / \delta_{\text{DGR}} - N(\text{HI})] / 2, \quad (23)$$

which simply states that the dust optical depth (τ_d) is a perfect tracer of the total column density of gas when the emissivity per nucleon (δ_{DGR}) is known. As we discussed above, δ_{DGR} can be straightforwardly determined on lines of sight dominated by atomic gas, for example. The comparison of the molecular column density so derived with the observed $W(\text{CO})$ yields $X_{\text{CO},20} \approx 1.8 \pm 0.3$, which is valid for $|b| > 5^\circ$ on large scales across the Galaxy. This study also finds evidence for a systematic increase in X_{CO} by factors of \sim two to three at high Galactic latitude ($b > 20^\circ$), in regions with typical $N(\text{H}_2) \lesssim 0.5 \times 10^{20} \text{ cm}^{-2}$ on $\sim 0.5^\circ$ angular scales.

The excellent *Planck* data set has afforded a new view on this topic (**Figure 4**). Planck Collaboration XIX et al. (2011) produced a new τ_d map for the Milky Way and a new determination of X_{CO} using Equation 23 for lines of sight with $|b| > 10^\circ$. They obtain $X_{\text{CO},20} = 2.54 \pm 0.13$, which is somewhat larger than that found by the previous study. This difference is likely methodological and may involve, for example, the use of different FIR wavelengths as well as local versus global calibrations of δ_{DGR} .

4.2.4. CO-faint molecular gas and diffuse lines of sight. Most interestingly, Planck Collaboration XIX et al. (2011) observe a tight linear correlation between τ_d and $N(\text{HI}) + 2X_{\text{CO}} W(\text{CO})$ for $A_V \lesssim 0.4$ and $2.5 \lesssim A_V \lesssim 10$, with an excess in τ_d in the intermediate range (**Figure 5**). This excess can be understood in terms of a component of H_2 (or possibly a combination of H_2 and cold, opaque HI) that emits weakly in CO and is prevalent at $0.4 \lesssim A_V \lesssim 2.5$ (the explanation is not unique because the methodology cannot distinguish it from a change in dust emissivity in that narrow A_V regime, but such a possibility appears unlikely). This molecular component arises from the region in cloud surfaces where gas is predominantly H_2 but most carbon is not in CO molecules because the extinction is too low, essentially the PDR surface (see Section 6.1 and **Figure 1**). This component is frequently referred to as CO-dark molecular gas or sometimes simply dark gas (Grenier, Casandjian & Terrier 2005; Wolfire, Hollenbach & McKee 2010). In this review, we refer to it as CO-faint, which is a more accurately descriptive name. The existence of molecular gas with low CO abundance has been noted previously in theoretical models (e.g., van Dishoeck & Black 1988), in observations of diffuse gas and high-latitude clouds (e.g., Lada & Blitz 1988), and in observations of irregular galaxies (e.g., Madden et al. 1997). In this context, the results by Planck Collaboration XIX et al. (2011) are in qualitative agreement with already discussed observations that show an increase in X_{CO} at low molecular column densities (e.g., Goldsmith et al. 2008, Paradis et al. 2012).

The *Planck* observations are also in qualitative agreement with the analysis by Grenier, Casandjian & Terrier (2005), who correlated the diffuse γ -ray emission over the entire sky with templates derived from HI, CO, and dust, finding a component of gas not traced by CO evident in local

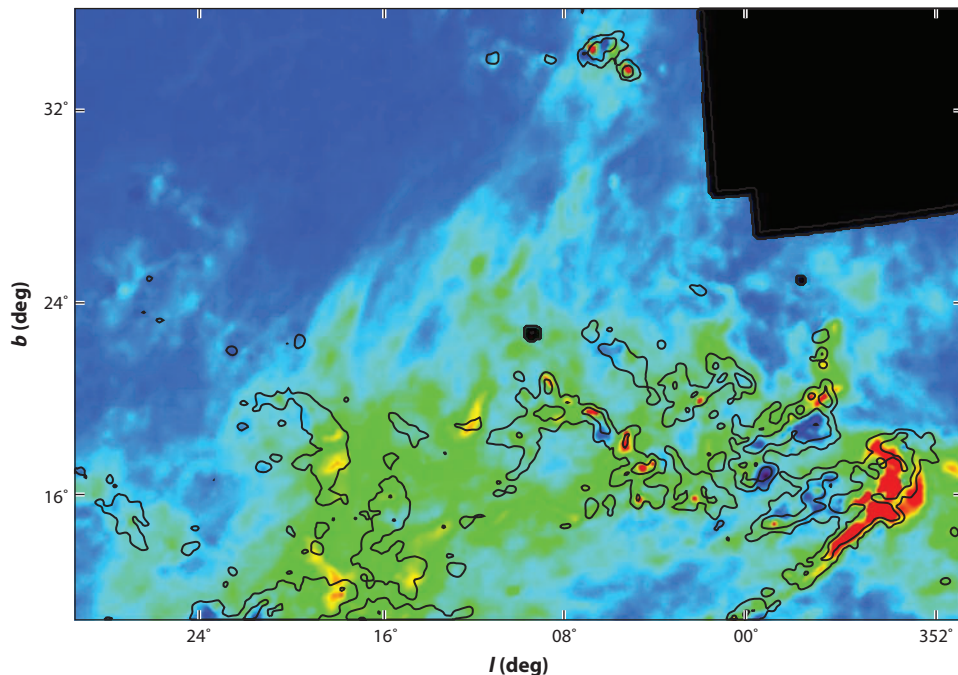


Figure 4

Planck results in the Aquila-Ophiuchus flare (Planck Collaboration XIX et al. 2011). The figure shows molecular gas column density with a color range $N(\text{H}_2) \approx -1.5 \times 10^{21} \text{ cm}^{-2}$ (dark blue) to $3.5 \times 10^{21} \text{ cm}^{-2}$ (red). The black contours illustrate the CO emission from the Columbia survey, with values $I_{\text{CO}} \approx 2, 10, 20 \text{ K km s}^{-1}$. The black region lacks CO information.

clouds at high latitudes. Their analysis finds that this component is as important, by mass, as the CO-bright H_2 component in several of these clouds, and increasingly more important for smaller cloud masses. The recent analyses based on *Fermi* data by Abdo et al. (2010c) and Ackermann et al. (2012d) are also qualitatively compatible with these results, finding that the CO-faint component amounts to 40%–400% of the CO-bright mass in the Cepheus, Polaris, Chamaleon, R Cr A, and Cassiopeia clouds (small local molecular clouds).

The ionized carbon FIR fine-structure emission provides an additional probe of molecular gas at low A_V . Large-scale $[\text{CII}]$ observations of the ($^2\text{P}_{3/2} \rightarrow ^2\text{P}_{1/2}$) fine-structure transition in the Milky Way and external galaxies suggest it is due to a combination of emission from the cold neutral medium (CNM) and from PDRs located in the surfaces of GMCs (Shibai et al. 1991, Stacey et al. 1991, Bennett et al. 1994). The contribution from $[\text{CII}]$ in the diffuse ionized gas, however, could also be important (Madden et al. 1993, Heiles 1994), particularly along certain lines of sight (Velusamy et al. 2012).

In regions where most of the emission arises in PDRs, $[\text{CII}]$ has the potential to trace the CO-faint molecular regime at low A_V . Langer et al. (2010) analyze 16 lines of sight in the plane of the Galaxy and find that in about half of them the observed $[\text{CII}]$ intensity can be entirely explained as being due to carbon in atomic gas in the CNM. The other half, however, exhibits $[\text{CII}]/N(\text{H})$ ratios that are too large to be due to atomic gas and may have molecular to atomic ratios as large as $N(\text{H}_2)/N(\text{H}) \sim 6$. Although the very brightest $[\text{CII}]$ components investigated arise from dense ($n > 10^5 \text{ cm}^{-3}$) PDRs exposed to intense radiation fields, most of the $[\text{CII}]$

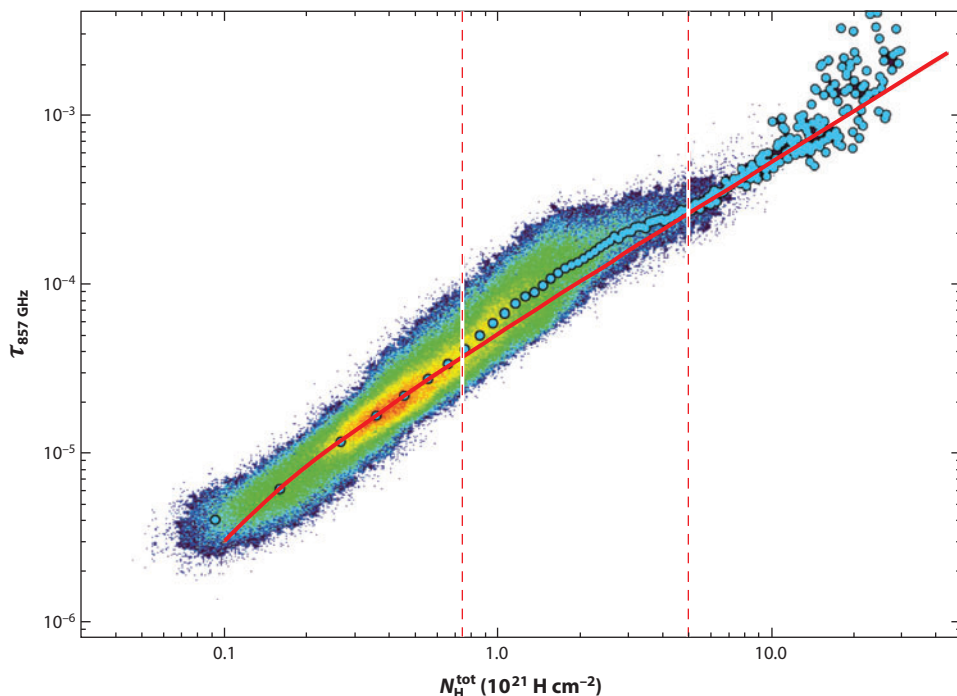


Figure 5

Correlation between τ_d at 350 μm and total hydrogen column density N_{H} for $X_{\text{CO},20} = 2.3$ (for $|b| > 10^\circ$; Planck Collaboration XIX et al. 2011). The color scale represents the logarithm of the number of lines of sight, and the blue dots represent the result of N_{H} binning. The red dashed lines indicate $A_V = 0.37$ and $A_V = 2.5$. The red solid line represents the best linear fit for low N_{H} . Note that it is also a good fit to the $A_V \gtrsim 2.5$ points. The excess in the binned correlation over the red line for $0.37 \lesssim A_V \lesssim 2.5$ is either an indication of CO-faint molecular gas (possibly a combination of high optical-depth HI with CO-faint H₂) or a change in the dust emissivity over this A_V regime.

emission in these molecular lines of sight can be explained as originating in the surfaces of modestly dense GMCs [$n \sim (3 - 300) \times 10^3 \text{ cm}^{-3}$] exposed to at most a few times the local ISRF at the Solar Circle (Pineda et al. 2010a). Following the reasoning in Velusamy et al. (2010) and Langer et al. (2010), a very approximate relation between [CII] emission and CO-faint H₂ is $N(\text{H}_2) \sim 1.46 \times 10^{20} W([\text{CII}]) - 0.35 N(\text{HI}) \text{ cm}^{-2}$, for $W([\text{CII}])$ in K km s⁻¹ (see Equation 7 to convert between Janskys and Kelvins). We caution that the coefficients correspond to the Milky Way carbon abundance and are very dependent on the assumed physical conditions, particularly the densities [we use $n(\text{HI}) \sim 200 \text{ cm}^{-3}$, $n(\text{H}_2) \sim 300 \text{ cm}^{-3}$, and $T_{\text{HI}} \sim T_{\text{H}_2} \sim 100 \text{ K}$].

Liszt, Pety & Lucas (2010) measure X_{CO} in diffuse gas by first estimating the total hydrogen column from dust continuum emission (using the map by Schlegel, Finkbeiner & Davis 1998), and subtracting the observed HI column density (c.f., Equation 23). They select lines of sight with HCO⁺ absorption spectra against bright extragalactic continuum sources. The CO emission, together with the measured H₂ column, provides a measure of X_{CO} . Surprisingly, Liszt, Pety & Lucas (2010) and Liszt & Pety (2012) find mean values in diffuse gas similar to those in GMCs. There are large variations, however, about the mean with low X_{CO} (bright CO) produced in warm $T \sim 100 \text{ K}$ diffuse gas and high X_{CO} (faint CO) produced at low $N(\text{H}_2)$ column densities. The researchers argue that these variations mainly reflect the CO chemistry and its dependence

on UV radiation field, density, and total column density, rather than the H_2 column density. We note that the observed CO column densities cannot be produced in steady-state PDR models (e.g., Sonnentrucker et al. 2007). Enhanced CO production might occur through the CH^+ channel driven by nonthermal ion-neutral reactions (Federman et al. 1996, Visser et al. 2009) or by pockets of warm gas and ion-neutral reactions in turbulent dissipation regions (Godard, Falgarone & Pineau des Forets 2009). Density fluctuations in a turbulent median might also increase the CO production (Levrier et al. 2012). Thus, although the mean X_{CO} diffuse cloud value is similar to GMCs, the CO emission from diffuse gas cannot be easily interpreted as a measure of the molecular column except perhaps in a statistical sense.

4.3. X_{CO} Based on Gamma-Ray Observations

Diffuse γ -ray emission in the Galaxy is chiefly due to three processes: neutral pion production and subsequent decay in collisions between cosmic rays and interstellar matter, bremsstrahlung emission due to scattering of cosmic-ray electrons by interstellar matter, and inverse Compton scattering of low-energy photons by cosmic-ray electrons. The first of these processes is the dominant production channel for diffuse γ -rays with energies above 200 MeV, although at high Galactic latitude there is an increasingly important inverse Compton component (Bloemen 1989). Interestingly, the fact that interactions between cosmic rays and nucleons give rise to diffuse γ -ray emission can be used to count nucleons in the ISM, and indeed the use of X_{CO} to represent the ratio $N(\text{H}_2)/W(\text{CO})$ was introduced for the first time in γ -ray work using observations from the COS B satellite (Lebrun et al. 1983).

Accounting for the pion decay and bremsstrahlung processes, and neglecting the contribution from ionized gas, the basic idea behind modeling the emission is to use a relation $I_\gamma = \sum \epsilon_{\gamma, \text{HI}}(R_i)[N(\text{HI})_i + 2 Y_{\text{CO}} W(\text{CO})_i]$ (Bloemen 1989). Here, I_γ is the diffuse γ -ray emission along a line of sight, ϵ_γ is the HI gas emissivity (a function of Galactocentric radius R), and Y_{CO} is a parameter that takes into account that emissivity in molecular clouds may be different than in atomic gas, due to cosmic-ray exclusion or concentration, $X_{\text{CO}} = Y_{\text{CO}} \epsilon_{\gamma, \text{HI}}/\epsilon_{\gamma, \text{H}_2}$ (Gabici, Aharonian & Blasi 2007; Padovani, Galli & Glassgold 2009). This situation is analogous to that presented in dust emission techniques, where emissivity changes in the molecular and atomic components will be subsumed in the resulting value of X_{CO} .

Recent analyses use the approach $I_\gamma \approx q_{\text{HI}}N(\text{HI}) + q_{\text{CO}}W(\text{CO}) + q_{\text{EBV}}E(B - V)_{\text{res}} + \dots$, where the first three terms account for emission that is proportional to the HI, the CO-bright H_2 , and a CO-faint H_2 component that is traced by dust reddening or emission residuals (the additional terms not included account for an isotropic γ -ray background and the contribution from point sources, e.g., Abdo et al. 2010c). The dust residual template consists of a dust map (e.g., Schlegel, Finkbeiner & Davis 1998) with a linear combination of $N(\text{HI})$ and $W(\text{CO})$ fitted and removed.

4.3.1. Observational results. A discussion of the results of older analyses can be found in Bloemen (1989). Here, we refer to a few of the more recent results using the *Compton Gamma Ray Observatory* and *Fermi* satellites.

Strong & Mattox (1996) analyzed the EGRET all-sky survey obtaining $X_{\text{CO}, 20} \approx 1.9 \pm 0.2$. Similar results were obtained by Hunter et al. (1997) for the inner Galaxy, and by Grenier, Casandjian & Terrier (2005) for clouds in the Solar Neighborhood (see also Section 4.2.4). Strong et al. (2004) introduce in the analysis a Galactic gradient in X_{CO} in an attempt to explain the discrepancy between the derived $\epsilon_\gamma(R)$ and the distributions of supernova remnants and pulsars, which trace the likely source of cosmic rays in supernovae shocks. Matching the emissivity to

the pulsar distribution requires a significant change in X_{CO} between the inner and outer Galaxy ($X_{\text{CO},20} \approx 0.4$ for $R \sim 2.5$ kpc to $X_{\text{CO},20} \approx 10$ for $R > 10$ kpc).

The sensitivity of *Fermi* has been a boon for studies of diffuse γ -ray emission in our Galaxy. Abdo et al. (2010c) and Ackermann et al. (2011, 2012b,c) analyze the emission in the Solar Neighborhood and the outer Galaxy. Taken together, they find a similar X_{CO} for the Local arm and the interarm region extending out to $R \sim 12.5$ kpc, $X_{\text{CO},20} \sim 1.6$ – 2.1 depending on the assumed HI spin temperature. The very local high-latitude clouds in the Gould Belt have a lower $X_{\text{CO},20} \approx 0.9$ and appear not to represent the average properties at the Solar Circle (Ackermann et al. 2012b,a).

It is important to note, however, that the *Fermi* studies follow the convention $X_{\text{CO}} \equiv q_{\text{CO}}/2q_{\text{HI}}$ with the parameters defined in the previous section. Thus, their definition of X_{CO} does not include the CO-faint envelope that is traced by the dust residual template: it only accounts for the H_2 that is emitting in CO. This is different from the convention adopted in the dust studies discussed in the previous section, where all the H_2 along a line of sight is associated with the corresponding CO. Ackermann et al. (2012b) report $X_{\text{CO},20} \approx 0.96, 0.99,$ and 0.63 for Chameleon, R Cr A, and the Cepheus/Polaris Flare region, respectively, using the *Fermi* convention. The ratio of masses associated with the CO and the dust residual template (reported in their table 4) suggests that we should correct these numbers by factors of approximately 5, 2, and 1.4, respectively, to compare them with the dust modeling. This correction results in $X_{\text{CO},20} \approx 4.8, 2,$ and 0.9 , bringing these clouds in much better (albeit not complete) agreement with the results of dust modeling and the expectation that they be underluminous—not overluminous—in CO due to the presence of a large CO-faint molecular component.

4.3.2. Considerations and limitations. We have already mentioned a limitation on γ -ray studies of X_{CO} , i.e., the degree to which they may be affected by the rejection (or generation) of cosmic rays in molecular clouds. A major limitation of γ -ray determinations is also the poor angular resolution of the observations. Another source of uncertainty has become increasingly apparent with *Fermi*, which resolves the Magellanic Clouds in γ -ray emission (Abdo et al. 2010a,b). In the Clouds, the distribution of emission does not follow the distribution of gas. Indeed, the emission is dominated by regions that are not peaks in the gas distribution, but may correspond to sites of cosmic-ray injection (e.g., Murphy et al. 2012), suggesting that better knowledge of the cosmic-ray source distribution and diffusion will have an important impact on the results of γ -ray studies.

Ackermann et al. (2012d) carry out a thorough study of the impact of systematics on the global γ -ray analyses that include a cosmic-ray generation and propagation model, frequently used to infer Galactic X_{CO} gradients. They find that the X_{CO} determination can be very sensitive to assumptions such as the cosmic-ray source distribution and the HI spin temperature, as well as the selection cuts in the templates (in particular, the dust template). Indeed, the value in the outer Galaxy in their analysis is extremely sensitive to the model cosmic-ray source distribution. The magnitude of a Galactic X_{CO} gradient turns out to also be very sensitive to the underlying assumptions (see Ackermann et al. 2012d, their figure 25). What appears to be a robust result is a uniformly low value of X_{CO} near the Galactic center ($R \sim 0$ – 1.5 kpc). This was already pointed out by much earlier γ -ray studies (Blitz et al. 1985). These researchers also conclude that including the dust information leads to an improvement in the agreements between models and γ -ray data, even on the Galactic plane, suggesting that CO-faint gas is a ubiquitous phenomenon.

4.4. Synthesis: Value and Systematic Variations of X_{CO} in the Milky Way

There is a reassuring degree of uniformity among the values of X_{CO} obtained through the variety of methodologies available in the Milky Way. Representative results from analyses using virial

Table 1 Representative X_{CO} values in the Milky Way disk

Method	$X_{\text{CO}}/10^{20} \text{cm}^{-2}$ (K km s^{-1}) $^{-1}$	References
Virial	2.1	Solomon et al. (1987)
	2.8	Scoville et al. (1987)
Isotopologues	1.8	Goldsmith et al. (2008)
Extinction	1.8	Frerking, Langer & Wilson (1982)
	2.9–4.2	Lombardi, Alves & Lada (2006)
	0.9–3.0	Pineda, Caselli & Goodman (2008)
	2.1	Pineda et al. (2010b)
	1.7–2.3	Paradis et al. (2012)
Dust emission	1.8	Dame, Hartmann & Thaddeus (2001)
	2.5	Planck Collaboration XIX et al. (2011)
γ -rays	1.9	Strong & Mattox (1996)
	1.7	Grenier, Casandjian & Terrier (2005)
	0.9–1.9 ^a	Abdo et al. (2010c)
	1.9–2.1 ^a	Ackermann et al. (2011, 2012c)
	0.7–1.0 ^a	Ackermann et al. (2012a,b)

^aNote difference in X_{CO} convention (Section 4.3).

masses, CO isotopologues, dust extinction, dust emission, and diffuse γ -ray radiation hover around a typical value for the disk of the Milky Way, $X_{\text{CO}} \approx 2 \times 10^{20} \text{cm}^{-2} (\text{K km s}^{-1})^{-1}$ (**Table 1**). This fact, combined with the simple theoretical arguments outlined in Section 2 as to the physics behind the H_2 -to-CO conversion factor, as well as the results from elaborate numerical simulations discussed in Section 3.2, strongly suggests that we know the mass-to-light calibration for GMCs in the disk of the Milky Way to within ± 0.3 dex certainly, and probably with an accuracy closer to ± 0.1 dex (30%). This is an average number, valid over large scales. Individual GMCs will scatter around this value by a certain amount, and individual lines of sight will vary even more.

There are, however, some systematic departures from this value in particular regimes, as suggested by the simple theoretical arguments. As pointed out by several studies, the Galactic center region appears to have an X_{CO} value 3–10 times lower than the disk. In addition to the aforementioned γ -ray results (Blitz et al. 1985, Strong et al. 2004, Ackermann et al. 2012d), a low X_{CO} in the center of the Milky Way was obtained by analysis of the dust emission (Sodroski et al. 1995) and the virial mass of its clouds (Oka et al. 1998, 2001). We discuss in Section 5 that this is not uncommonly observed in the centers of other galaxies. It is likely due to a combination of enhanced excitation (clouds are hotter) and the dynamical effects discussed in Section 2.3.

Departures may occur in some nearby, high-latitude clouds, for example, the Cepheus/Polaris Flare region. A critical step to understanding the magnitude or even existence of such discrepancies is to derive X_{CO} for diffuse γ -ray observations using conventions matched to other fields. We have attempted some estimate of the correction in the Chameleon, R CrA, and the Cepheus/Polaris Flare. In Cepheus/Polaris, even after trying to account for the difference in X_{CO} convention, the γ -ray studies find a low X_{CO} value, suggesting that those local clouds are overluminous in CO by a factor of \sim two or maybe that their dust emissivity is different. Low values are not consistent with results from dust emission techniques (Dame, Hartmann & Thaddeus 2001; Planck Collaboration XIX et al. 2011). However, they are known to be turbulent to very small (~ 0.01 pc)

scales (Miville-Deschênes et al. 2010), and turbulent dissipation may play a role in exciting CO (Ingalls et al. 2011).

Finally, observations of X_{CO} in the outer galaxy are still sparse, although some of them suggest high values of X_{CO} (for example, Brand & Wouterloot 1995; Heyer, Carpenter & Snell 2001). This can be understood in terms of an increasing dominance of the CO-faint molecular gas associated probably with decreasing metallicities in the outer disk (see, Section 6). In nearby, resolved molecular clouds there is compelling evidence that a regime of high X_{CO} exists at low extinctions and column densities (e.g., Goldsmith et al. 2008, Pineda et al. 2010b), where most of the carbon in the gas phase is not locked in CO molecules.

It seems clear that CO becomes a poor tracer of H_2 at low column densities. Most studies agree that this phenomenon occurs for $A_V \lesssim 2$ (Goldsmith et al. 2008, Planck Collaboration XIX et al. 2011). How much molecular gas exists in this regime is still a subject of study, but it seems to represent a substantial, perhaps even dominant, fraction of the H_2 near the Solar Circle (Grenier, Casandjian & Terrier 2005; Wolfire, Hollenbach & McKee 2010; Planck Collaboration XIX et al. 2011). It is, however, unlikely to be a large fraction of the total molecular mass of the Galaxy, which is dominated by clouds in the inner galaxy. Nonetheless, this CO-faint phase almost surely constitutes most of the molecular gas in low-metallicity systems.

Using these conclusions, what is the characteristic surface density of a GMC, Σ_{GMC} , in the Milky Way? The precise value, or even whether it is a well-defined quantity, is a matter of study. Using the survey by Solomon et al. (1987) updated to the new distance scale and assuming $X_{\text{CO},20} = 2$, we find a distribution of surface densities with $\Sigma_{\text{GMC}} \approx 150^{+95}_{-70} \text{ M}_{\odot} \text{ pc}^{-2}$ ($\pm 1\sigma$ interval). Using instead the distribution of $331\sigma^2/R$ to evaluate surface density (see discussion after Equation 9), we obtain $\Sigma_{\text{GMC}} \approx 200^{+130}_{-80} \text{ M}_{\odot} \text{ pc}^{-2}$. Heyer et al. (2009) use ^{13}CO observations of these clouds, finding $\Sigma_{\text{GMC}} \approx 40 \text{ M}_{\odot} \text{ pc}^{-2}$ over the same cloud areas but concluding that it is likely an underestimate by at least a factor of two due to non-LTE and optical depth effects ($\Sigma_{\text{GMC}} \approx 144 \text{ M}_{\odot} \text{ pc}^{-2}$ using a more restrictive ^{13}CO contour instead of the original ^{12}CO to define surface area; Roman-Duval et al. 2010). Real clouds have a range of surface densities. Heiderman et al. (2010) analyze extinction-based measurements for 20 nearby clouds, calculating their distribution of Σ_{mol} . It is clear that many of these clouds do not reach the characteristic Σ_{GMC} of clouds in the inner Galaxy; for the most part the clouds with low mass tend to have low surface densities. Nonetheless, several of the most massive clouds do have $\Sigma_{\text{GMC}} \gtrsim 100 \text{ M}_{\odot} \text{ pc}^{-2}$. The mass-weighted (area-weighted) Σ_{GMC} are 160, 150, 140, and 110 (140, 140, 100, and 90) $\text{M}_{\odot} \text{ pc}^{-2}$ for Serpens-Aquila, Serpens, Ophiuchus, and Perseus, respectively, according to Heiderman et al. (2010, see their table 2). By comparison, $\Sigma_{\text{GMC}} \approx 85 \text{ M}_{\odot} \text{ pc}^{-2}$ for a sample of nearby galaxies, many of them dwarf (Bolatto et al. 2008). Note that Σ_{GMC} is likely to be a function of the environment. In the Galactic Center, for example, Oka et al. (1998, 2001) report a size–line width relation where the coefficient C is five times larger than that observed in the Milky Way disk, suggesting a Σ_{GMC} that is 25 times larger (see also Rosolowsky & Blitz 2005).

5. X_{CO} IN NORMAL GALAXIES

The distance of even the nearest galaxies renders CO the primary tracer of molecular gas outside the Milky Way, a situation that will improve but not reverse with ALMA. Other galaxies therefore represent the key application of X_{CO} . They also offer a wider range of environments than the Milky Way and a simpler mapping between local ISM conditions, especially metallicity, and line of sight. As a result, for more than two decades, observations of the nearest galaxies have been used to test and extend calibrations of X_{CO} as a function of metallicity and other local ISM properties. Here we review the techniques available to derive X_{CO} in normal galaxies, meaning star-forming

dwarf, spiral, or elliptical galaxies. We discuss specific efforts to understand the behavior of X_{CO} as a function of metallicity in Section 6 and the special case of overwhelmingly molecular starburst galaxies, such as the local LIRGs and ULIRGs, in Section 7. Section 8 considers X_{CO} in galaxies at high redshift.

Only a subset of the techniques used to determine X_{CO} in the Milky Way can be applied to other galaxies. In each case, the limited sensitivity and resolution of millimeter, submillimeter, and IR facilities complicate the calculation. Direct estimates rely almost exclusively on the use of virial mass measurements (Section 4.1), dust emission employed as an optically thin tracer of the total gas reservoir (Section 4.2), or modeling of multiple CO lines. Ideally such modeling includes optically thin isotopologues, but studies of high-redshift systems must often make do with a few (or only one) ^{12}CO line ratios (Section 8).

5.1. Extragalactic Virial Mass Estimates

Since the late 1980s, millimeter telescopes have been able to resolve CO emission from nearby galaxies into discrete molecular clouds. From such observations, one can estimate the line width, size, and luminosity of these objects and proceed as in Section 4.1 (see the recent review by Fukui & Kawamura 2010).

Resolution and sensitivity have limited virial mass measurements to the nearest galaxies, those in the Local Group and its immediate environs. The Magellanic Clouds ($d \sim 50$ kpc) are close enough that single-dish telescopes resolve individual clouds (e.g., Rubio, Lequeux & Boulanger 1993; Mizuno et al. 2001; Israel et al. 2003; Fukui et al. 2008; Hughes et al. 2010; Wong et al. 2011). Millimeter-wave interferometers resolve populations of GMCs in other Local Group galaxies—M31, M33, NGC 6822, and IC 10 ($d \sim 1$ Mpc) (e.g., Vogel, Boulanger & Ball 1987; Wilson & Scoville 1990; Wilson 1995; Rosolowsky et al. 2003; Leroy et al. 2006; Blitz et al. 2007; Fukui & Kawamura 2010).

Early measurements beyond the Local Group focused on very nearby dwarf galaxies ($d \sim 3$ Mpc) (Taylor et al. 1999; Walter et al. 2001, 2002; Bolatto et al. 2008) or considered structures more massive than GMCs in more distant galaxies (giant molecular associations, or GMAs, e.g., Vogel, Kulkarni & Scoville 1988; Rand & Kulkarni 1990). The nearest spiral galaxies tend to be more distant ($d \sim 6$ Mpc), so that ~ 1 -arcsec resolution is required to resolve massive GMCs. Only recently, millimeter-wave interferometers have begun to achieve this resolution with the requisite sensitivity by investing large amounts of time into dedicated observations of bright regions of the nearest massive spiral galaxies (Donovan Meyer et al. 2012, 2013; Rebolledo et al. 2012). This has allowed the first cloud-scale virial mass measurements of populations of clouds in spiral galaxies beyond the Local Group.

5.1.1. X_{CO} from extragalactic virial mass analyses. Broadly, virial mass measurements across a wide range of environments yield $X_{\text{CO},20} \approx 1$ –4, consistent with Milky Way results and very similar to X_{CO} derived from dust-based techniques applied to high-mass nearby galaxies. Bolatto et al. (2008) find $X_{\text{CO},20} \approx 3.5^{+1.8}_{-1.2}$ in 12 nearby systems. In the highest-resolution studies of the Large Magellanic Cloud (LMC) to date, Israel et al. (2003), Hughes et al. (2010), Wong et al. (2011), and Pineda et al. (2010b) all find $X_{\text{CO},20} \approx 4$. Considering NGC 6946, one of the nearest molecule-rich spiral galaxies, Donovan Meyer et al. (2012) report $X_{\text{CO},20} \approx 1.2$ and Rebolledo et al. (2012) find $X_{\text{CO},20} \sim 2$. In M33, Rosolowsky et al. (2003) show $X_{\text{CO},20} \sim 2$ independent of radius and metallicity. In M31, Rosolowsky (2007) calculate $X_{\text{CO},20} \approx 4$ assuming virial equilibrium.

Figure 6 shows the relationship between virial mass and CO luminosity for a subset of these measurements. A good correlation extends across three orders magnitude in luminosity and roughly a dozen systems. As in the Milky Way, there may be evidence for a slightly sublinear

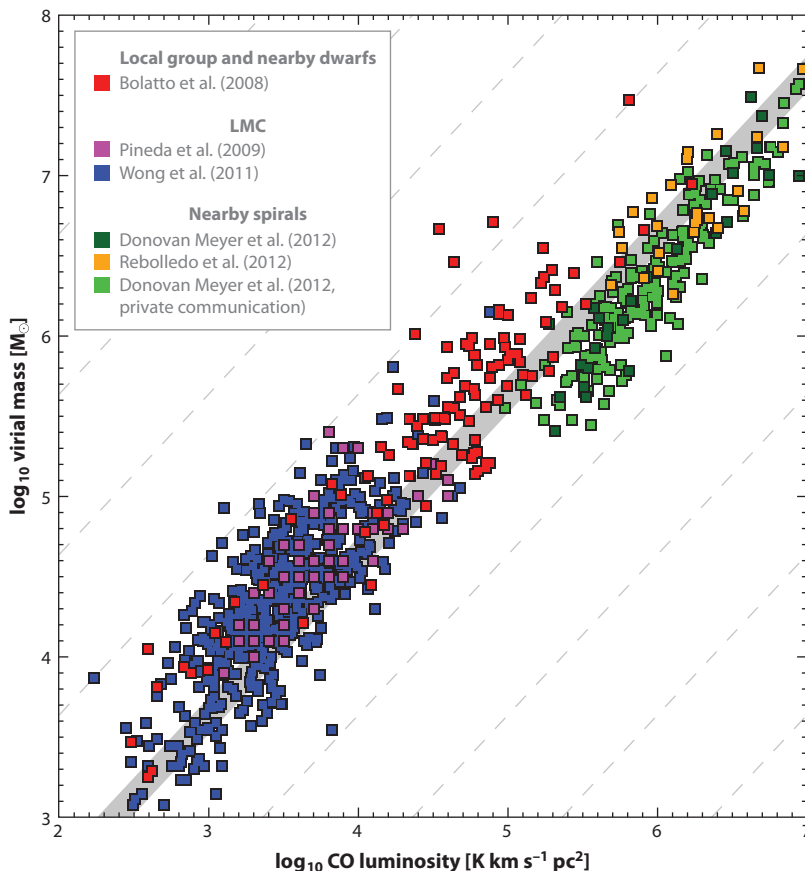


Figure 6

Relation between virial mass (y -axis) and CO luminosity (x -axis) for extragalactic giant molecular clouds. We show virial masses measured from selected high spatial resolution CO observations of nearby galaxies: the compilation of Bolatto et al. (2008, including M31, M33, and nine dwarf galaxies), high-resolution studies of the Large Magellanic Cloud (LMC) by Pineda et al. (2009) and Wong et al. (2011), and high-resolution studies of the nearby spiral NGC 6946 by Donovan Meyer et al. (2012) and Rebolledo et al. (2012), as well as NGC 4826 and NGC 4736 by Donovan Meyer et al. (2013). Dashed lines show fixed X_{CO} , with the typical Milky Way value being $X_{\text{CO},20} = 2$ and $\pm 30\%$ indicated by the gray region. Virial mass correlates with luminosity, albeit with large scatter, across more than three orders of magnitude in extragalactic systems. The median across all displayed data is $X_{\text{CO},20} = 2.8$ with 0.4 dex scatter, and the best fit relation has a power-law index of 0.90 ± 0.05 , reflecting that most Local Group clouds show $X_{\text{CO},20} \sim 4$, while both studies of the bright spiral NGC 6946 find a lower $X_{\text{CO},20} \approx 1$ –2.

slope (see Sections 2.1 and 4.1 and **Figure 2**), though this may also reflect methodological or environmental differences among the galaxies studied. Across the ensemble of points, we plot the median $X_{\text{CO},20} = 2.9$ with 0.4 dex scatter (slightly larger than a factor of two).

Surprisingly at first, these Galactic X_{CO} values obtained from virial masses extend to low-metallicity, irregular galaxies. In the low-metallicity Small Magellanic Cloud (SMC, with $12 + \log[\text{O}/\text{H}] \approx 8.0$; Dufour, Shields & Talbot 1982), Bolatto et al. (2003) and Israel et al. (2003) find $X_{\text{CO},20} \approx 4$, which is consistent with the Milky Way value. Rosolowsky et al. (2003) find no dependence of X_{CO} on metallicity in M33. Leroy et al. (2006) find an approximately Galactic X_{CO}

in the Local Group dwarf IC 10 ($12 + \log[\text{O}/\text{H}] \approx 8.17$; Lequeux et al. 1979). Wilson (1994) found $X_{\text{CO},20} \lesssim 6.6$ in NGC 6822 ($12 + \log[\text{O}/\text{H}] \approx 8.20$; Lequeux et al. 1979). Most of the galaxies studied by the aforementioned Bolatto et al. (2008) are dwarf irregulars with subsolar metallicity. In each case, we highlight the results for the highest resolution study of the galaxy in question. We discuss the effects of varying spatial resolution in the next section. Overall, these studies show that high spatial resolution virial mass measurements suggest roughly Galactic X_{CO} irrespective of metallicity.

Virial masses have also been measured for very large structures, GMAs or superclouds (Vogel, Kulkarni & Scoville 1988; Wilson et al. 2003), although it is unclear the degree to which they are virialized or even bound. Wilson et al. (2003) consider ~ 500 -pc-scale structures in the Antennae Galaxies and find the X_{CO} to be approximately Galactic (see also Ueda et al. 2012; Wei, Keto & Ho 2012), but this conflicts with results from spectral line modeling (see Section 7). Phrasing their results largely in terms of boundedness, Rand & Kulkarni (1990) and Adler et al. (1992) find $X_{\text{CO},20} \sim 3$ and $X_{\text{CO},20} \sim 1.2$, respectively, to be needed for virialized GMAs in M51. Studies of other galaxies, for example M83 (Rand, Lord & Higdon 1999), suggest that not all GMAs are gravitationally bound and that the mass spectrum of GMAs varies systematically from galaxy to galaxy or between arm and interarm regions (Rand & Kulkarni 1990; Rand, Lord & Higdon 1999; Wilson et al. 2003), complicating the interpretation of these large-scale measurements.

5.1.2. Caveats on virial mass-based X_{CO} estimates. As we show in Section 5.2, the approximately constant Galactic X_{CO} implied by virial masses on small scales at low metallicity appears to contradict the finding from dust-based measurements and other scaling arguments (for example, Blanc et al. 2013), which consistently indicate that X_{CO} increases with decreasing metallicity. This discrepancy most likely arises because virial mass measurements sample the gas that is bright in CO, whereas dust-based measurements include all H_2 along the line of sight. As discussed below (Section 6), decreasing dust shielding at low metallicities causes CO to be preferentially photodissociated relative to H_2 , creating a massive reservoir of H_2 in which C^+ and C rather than CO represent the dominant forms of gas-phase carbon. Because this reservoir is external to the CO-emitting surface, it will not be reflected in the CO size or its line width (unless the surface pressure term is important). Thus, we expect that high-resolution virial mass measurements preferentially probe X_{CO} in the CO-bright region.

The range of values discussed above, $X_{\text{CO},20} \sim 1\text{--}4$, is significant. Does it indicate real variations in X_{CO} ? Measuring cloud properties involves several methodological choices (Section 4.1). Different methods applied to the same Milky Way data shift results by $\sim 30\%$, and biases of $\sim 40\%$ are common in extragalactic data (e.g., Rosolowsky & Leroy 2006). As we discuss below, the X_{CO} obtained by virial mass analysis seems to depend on the physical resolution of the observations. Ideally, results will be compared to control measurements that have been extracted and analyzed in an identical way, ideally at matched spectral and spatial resolution and sensitivity (e.g., Pineda et al. 2009). Many studies now employ the CPROPS algorithm (Rosolowsky & Leroy 2006), which is designed to account for sensitivity and resolution biases in a systematic way, allowing ready cross-comparison among data sets. This is not a perfect substitute, however, for matched analyses. Our assessment is that in lieu of such careful comparison, differences of $\pm 50\%$ in X_{CO} should still be viewed as qualitatively similar.

We raised the issue of spatial scale in the discussion of systematics and implicitly in the discussion of GMAs. Virial mass-based X_{CO} exhibits a complex dependence on the spatial scale of the observations. For dwarf galaxies it seems that, even using similar methodology and accounting for resolution biases, studies with finer spatial resolution systematically return lower X_{CO} than coarser resolution studies. For example, Hughes et al. (2010) find $X_{\text{CO},20} \approx 4$ in the LMC (as do Israel

et al. 2003, Pineda et al. 2009, and Wong et al. 2011) compared to $X_{\text{CO},20} \approx 7$ found by Fukui et al. (2008) using similar methodology but with about three times coarser linear resolution. In the SMC, Mizuno et al. (2001) find $X_{\text{CO},20} \approx 14$, whereas higher resolution studies find X_{CO} as low as $X_{\text{CO},20} \sim 2\text{--}4$ for the smallest resolved objects (Israel et al. 2003, Bolatto et al. 2003). Contrasting the interferometer measurements of Wilson (1994) and the coarser single-dish observations of Gratier et al. (2010) reveals a similar discrepancy in NGC 6822. In one of the first studies to consider this effect, Rubio, Lequeux & Boulanger (1993) explicitly fit a dependence for X_{CO} in the SMC as a function of spatial scale, finding $X_{\text{CO}} \propto R^{0.7}$ (see also the multiscale analyses in Bolatto et al. 2003, Leroy et al. 2009).

This scale dependence may reflect one of several scenarios. First, low-resolution observations can associate physically distinct clouds that are not bound, causing a virial mass analysis to over-predict X_{CO} . Alternatively, the ensemble of clouds conflated by a coarser beam may indeed be bound. In the case of a heavily molecular ISM like the Antennae Galaxies or the arm regions of M51, most of the material in the larger bound structure may be molecular and a virial mass measurement may yield a meaningful, nearly Galactic conversion factor for objects much bigger than standard GMCs. For a low-metallicity irregular galaxy, the best case for low-resolution virial mass measurements is that large complexes are virialized and that the low A_V gas between the bright clouds is H_2 associated with $[\text{CII}]$. We caution, however, that this is only one of many possible scenarios.

We suggest that the sensitivity of virial mass measurements to extended CO-free envelopes of H_2 is ambiguous at best. In that sense, the uniformity in X_{CO} derived from virial masses probably reflects fairly uniform conditions in CO-bright regions of molecular clouds (Bolatto et al. 2008). The spatial scale at which virialized structures emerge in galaxies is unclear. Given these ambiguities and the assumptions involved in the calculation of virial masses, we emphasize the need for careful comparison to matched data to interpret virial results.

5.2. Extragalactic Dust-Based Estimates of X_{CO}

Dust is expected and observed to be well mixed with gas, and dust emission remains optically thin over most regions of normal galaxies. Following the approach outlined in Section 4.2, dust emission offers a tool to estimate X_{CO} . Modeling IR or millimeter emission yields an estimate of the dust optical depth, τ_d . Using Equation 23, X_{CO} can be estimated from τ_d , HI , CO , and the dust emissivity per H atom (Equation 22). Conventions in the literature vary, with τ_d sometimes combined with a dust mass absorption coefficient and used as a dust mass, and δ_{DGR} alternately cast as the emissivity per H atom or a dust-to-gas mass ratio. Regardless of convention, the critical elements are a linear tracer of the dust surface density and a calibration of the relation between this tracer and gas column density.

Thronson (1988) and Thronson et al. (1988) first suggest and apply variations on this technique to nearby galaxies. Israel (1997a) uses data from IRAS to carry out the first comprehensive dust-based extragalactic X_{CO} study. He considers individual regions in eight (mostly irregular) galaxies and derives τ_d from a combination of 60- and 100- μm continuum data. Israel (1997b) estimates δ_{DGR} , the dust emissivity per H atom, from comparison of τ_d and HI in regions within the galaxy of interest but chosen to lie well away from areas of active star formation, thus assumed to be atomic-dominated. This internally derived estimate of δ_{DGR} represents a key strength of the approach: δ_{DGR} is derived self-consistently from comparison of HI and τ_d and does not rely on assuming a dust-to-gas ratio. This leads to the cancellation of many systematic errors (e.g., see Israel 1997b, Leroy et al. 2007), leaving only variations in δ_{DGR} and τ_d within the target to affect the determination of X_{CO} in Equation 23.

5.2.1. Dust-based estimates in normal disk galaxies. *Spitzer* and *Herschel* allowed the extension of the dust approach to more massive, more distant, and more normal galaxies. Draine et al. (2007) compare galaxy-integrated IR spectral energy distribution (SED) modeling to CO and HI luminosities for a large sample. They argue that $X_{\text{CO},20} \approx 4$ (over entire galaxies) yields the most sensible gas-to-dust ratio results in their sample. Leroy et al. (2011) perform a self-consistent treatment of the Local Group galaxies M31 and M33, LMC, NGC 6822, and SMC. They find $X_{\text{CO},20} \approx 1\text{--}4.5$ for regions of M31, M33, and the LMC (the higher metallicity galaxies in the sample). Smith et al. (2012) use *Herschel* observations to solve for X_{CO} , finding $X_{\text{CO},20} \approx 2$ in M31.

Other dust tracers such as millimeter-wave continuum emission and visual extinction have been used to arrive at X_{CO} estimates, although usually by assuming or scaling a Galactic calibration with the associated systematic uncertainties. Guelin et al. (1993) use 1.2-mm continuum observations of the edge-on spiral NGC 891 to estimate $X_{\text{CO},20} \sim 1$. Both Nakai & Kuno (1995) and Guelin et al. (1995) study X_{CO} in M51, the former using extinction estimates from $\text{H}\alpha/\text{H}\beta$, the latter using millimeter-wave continuum emission. Nakai & Kuno (1995) arrive at $X_{\text{CO},20} \approx 0.9 \pm 0.1$ with a factor of ~ 2 variation with galactocentric radius, whereas Guelin et al. (1995) find $X_{\text{CO},20} \sim 0.6$. Zhu et al. (2009) employs 850- μm data to check the X_{CO} derived from spectral line modeling in NGC 3310 and NGC 157, finding good agreement with $X_{\text{CO},20} \approx 1.3\text{--}3.0$ in the disks of their targets and a much lower X_{CO} in the center of NGC 157.

Sandstrom et al. (2013) carry out the most comprehensive extragalactic study of X_{CO} to date. They combine high-quality CO $J = 2 \rightarrow 1$ maps with *Herschel* and *Spitzer* dust continuum and high-resolution HI data. Building on the method used by Leroy et al. (2011), they break apart galaxies into regions several squared kiloparsecs in size and within each region they simultaneously solve for δ_{DGR} and X_{CO} . This yields resolved, self-consistent X_{CO} measurements across 22 galaxy disks. Their methodology requires good signal-to-noise CO detections and so restricts robust X_{CO} measurements to reasonably CO-bright parts of galaxies, typically half of the optical disks. There, these researchers find $X_{\text{CO},20} \approx 1.4\text{--}1.8$ with a $1\text{-}\sigma$ scatter among individual solutions of 0.4 dex. [The weighting used to derive the average X_{CO} affects the mean value. Weighting all high-quality solutions equally, Sandstrom et al. (2013) find mean $X_{\text{CO},20} \approx 1.4$ and median $X_{\text{CO},20} \approx 1.2$. Weighting instead by CO intensity, they find $X_{\text{CO},20} \approx 1.8$.]

Figure 7a shows X_{CO} derived by Sandstrom et al. (2013) as a function of galactocentric radius for their whole sample. **Figure 7b** shows X_{CO} for each region normalized to the average value for the galaxy, highlighting the internal radial structure. This study finds clear central X_{CO} depressions for a number of galaxies. The value of X_{CO} in galaxy centers relative to their disks spans a range from no change to a factor of five below the galaxy average. The researchers note that these low central X_{CO} values tend to coincide with high stellar masses and enhanced CO brightness, suggesting that the effects discussed for starbursts in Section 7 may also be at play in the central parts of many galaxies, including the Milky Way (Section 4).

Thus in the disks of normal star-forming galaxies, a dust-based approach yields $X_{\text{CO},20} \approx 1\text{--}4$ on kiloparsec scales. For comparison, in the Milky Way extinction yields $X_{\text{CO},20} \approx 1.7\text{--}2.3$ and dust emission yields $X_{\text{CO},20} \approx 1.8\text{--}2.5$ (see Section 4.2 and **Table 1**). Thus, broadly, dust analyses strongly support a Milky Way conversion factor in the disks of normal, massive disk galaxies, but methodological differences and, presumably, real changes in X_{CO} with environment produce a factor of two spread among studies and galaxies.

5.2.2. Dust-based estimates in dwarf irregular galaxies. Dust-based determinations of X_{CO} in low-metallicity dwarf irregular galaxies consistently yield values much higher than Galactic, and also generally higher than virial estimates. Israel (1997a) finds in the SMC the lowest-metallicity target, a notably high $X_{\text{CO},20} \approx 120 \pm 20$. Boselli, Lequeux & Gavazzi (2002) carry out a similar

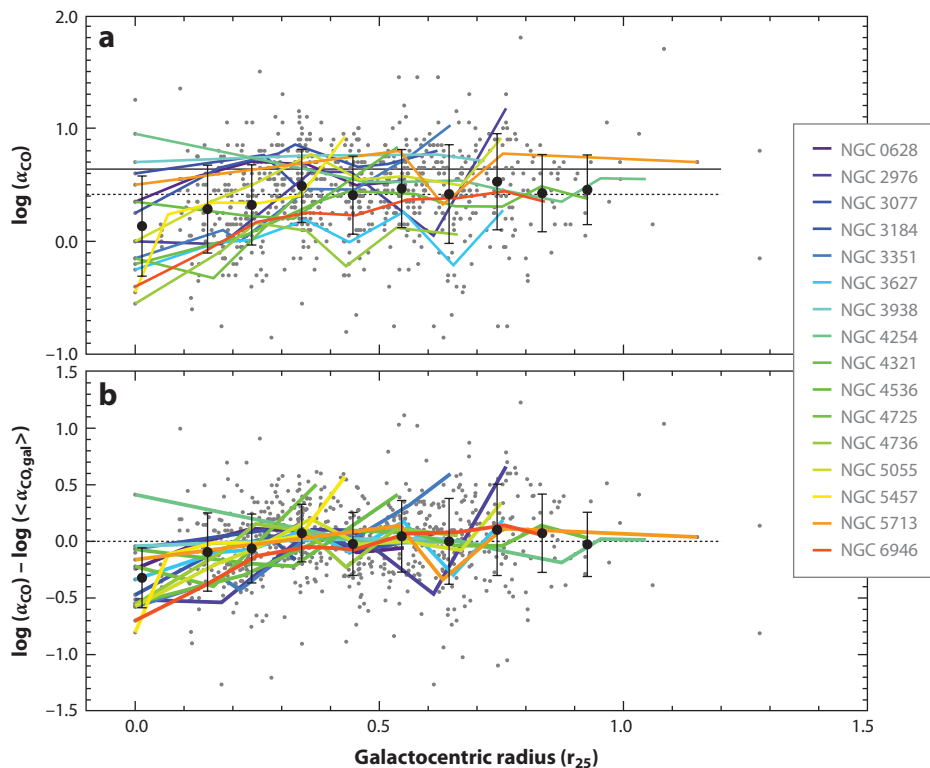


Figure 7

Dust-based α_{CO} determination across the disks of 22 galaxies (Sandstrom et al. 2013). (a) Shows the results for the individual regions (gray points), averages in radial bins for each galaxy (color lines), and the average trend for all data as a function of radius (black circles with error bars showing the scatter in that bin). The black solid line corresponds to $X_{\text{CO},20} = 2$, and the dotted line shows the average, weighting all solution pixels equally ($X_{\text{CO},20} = 1.2$). Weighting by galaxy or CO intensity rather than the line of sight, the mean is $X_{\text{CO},20} \approx 1.4$ – 1.8 for low-inclination galaxies. (b) Shows each galaxy normalized by its mean X_{CO} to highlight the fact that many galaxies exhibit low X_{CO} in their centers.

calculation and also find systematically higher X_{CO} at low metallicity. Subsequent studies leveraging the sensitivity, resolution, and wavelength coverage of *Spitzer* and *Herschel* qualitatively support this conclusion. Leroy et al. (2007, 2009), and Bolatto et al. (2011) follow Israel (1997a) and Stanimirovic et al. (2000) in analyzing the SMC. They find $X_{\text{CO},20} \approx 40$ – 120 using measurements that isolate individual clouds and estimate δ_{DGR} locally. Gratier et al. (2010) consider NGC 6822 using a similar technique, also finding high $X_{\text{CO},20} \approx 40$ on large scales. Attempting to minimize systematics and making very conservative assumptions, Leroy et al. (2011) still find $X_{\text{CO},20} \approx 10$ and 40 for NGC 6822 and the SMC, respectively, which is significantly higher than they find for the higher metallicity M31, M33, and the LMC.

In the Magellanic Clouds, *Herschel* and millimeter-wave bolometer cameras have mapped individual molecular clouds. Roman-Duval et al. (2010) find an increase in X_{CO} in the poorly shielded outer regions of LMC clouds. Rubio et al. (2004) and Bot et al. (2007, 2010) find unexpectedly bright millimeter-wave emission in SMC clouds. Bot et al. (2010) show that the emission suggests a factor of four higher masses than returned by a virial analysis, even on very small scales and even assuming a very conservative rescaled Milky Way dust mass emissivity coefficient.

Therefore, dust-based X_{CO} estimates indicate high conversion factors in low-metallicity, irregular systems. This agrees with some other methods of estimating X_{CO} but not with virial mass results, particularly on small scales, as discussed above (in Section 5.1). We discuss the discrepancy further below (in Section 6). The simplest explanation is that virial masses based on CO emission do not sample the full potential well of the cloud in low-metallicity systems, where CO is selectively photodissociated relative to H_2 at low extinctions.

5.2.3. Caveats on dust-based X_{CO} estimates. Because dust traces the total gas in the system with little bias (at least compared to molecules), this technique represents potentially the most direct way to estimate X_{CO} in other galaxies. We highlight two important caveats: the possibility of other invisible gas components and variations in the emissivity.

As described, the method traces all gas not accounted for by HI 21-cm observations and assigns it to H_2 . The good qualitative and quantitative association between H_2 derived in this manner and CO emission suggests that H_2 does represent the dominant component (e.g., Dame, Hartmann & Thaddeus 2001; Leroy et al. 2009), but opaque HI and ionized gas may still host dust that masquerades as H_2 using Equation 23. Both components could potentially represent significant mass reservoirs. Their impact on dust-based X_{CO} estimates depends on the methodology. Any smooth component evenly mixed with the rest of the ISM will divide out of a self-consistent analysis. Moreover, the warm ionized medium exhibits a large scale height compared to the cooler gas discussed here and may be subject to dust destruction without replenishment (e.g., see Draine 2009). Planck Collaboration XXI et al. (2011) find that dust associated with their ionized gas template represents a minor source of emission. However, absorption-line experiments from our Galaxy and others suggest that $\sim 20\%$ HI may be missed due to opacity effects (Heiles & Troland 2003) and observations of M31 suggest that it may lie in a filamentary, dense component (Braun et al. 2009), making it perhaps a more likely contaminant in X_{CO} determinations. Nonetheless, the close agreement between X_{CO} derived from dust and other determinations in our Galaxy strongly suggests that contamination from dust mixed with other invisible components, particularly the ionized gas, represents a minor correction.

Concerning the second caveat, the methodology relies on either blindly assuming or self-consistently determining the dust emissivity per hydrogen, δ_{DGR} . This is a combination of the dust-to-gas mass ratio and the mass absorption coefficient of dust at IR wavelengths. In blind determinations, a linear scaling of Equation 22 with metallicity is usually assumed. In self-consistent X_{CO} determinations, δ_{DGR} is measured locally through the ratio of the dust tracer to HI somewhere within the galaxy (for example, in an HI-dominated region) and ideally close to or inside the region where X_{CO} is estimated. This makes self-consistent determinations very robust. Even the most robust analyses, however, still assume δ_{DGR} to be constant over some region of a galaxy and along a line of sight, and between the atomic and molecular phases. The δ_{DGR} , however, may change across galaxies and between phases due to metallicity gradients, varying balance of dust creation and destruction, or changes in dust grain properties.

As discussed in Section 4.2, recent *Planck* results suggest only mild localized variations in the emissivity per H nucleon across the Milky Way. Observations of other galaxies do show that δ_{DGR} depends on metallicity (Draine et al. 2007, Muñoz-Mateos et al. 2009). Large-scale ISM density may also be important; δ_{DGR} appears depressed in the low-density SMC Wing and the outer envelopes of dwarf galaxies (Bot et al. 2004, Draine et al. 2007, Leroy et al. 2007). The balance of the dust production and destruction mechanisms is complex: Basic accounting implies that most dust mass buildup occurs in the ISM (Dwek 1998, Draine 2009, and references therein), suggesting an increase in δ_{DGR} in denser regions of the ISM where this accumulation must take place. Independent of dust mass buildup, if grains become more efficient emitters for their mass

at moderate densities (through the formation of fluffy aggregates, for example) then the effective δ_{DGR} will be higher at high densities. Though not strongly favored by the overall *Planck* results, which suggest that emissivity variations are localized, a number of researchers point to evidence for an environmental dependency of the dust emissivity (e.g., Cambr  s, Jarrett & Beichman 2005; Bot et al. 2007).

In our opinion, these caveats concerning emissivity will lead a dust-based approach to preferentially overpredict the amount of H_2 present and consequently X_{CO} , as dust associated with the molecular ISM will have a higher dust-to-gas ratio or be better at emitting in the FIR. Nonetheless, we still see the dust-based approach as the most reliable way of producing extragalactic X_{CO} estimates. Placing stronger quantitative constraints on these systematics requires further work. The *Planck* results noted above, and the close agreement in the Milky Way of dust-based X_{CO} with other techniques, suggest that emissivity variations are not a major concern.

5.3. Extragalactic Spectral Line Modeling

Observations of multiple CO lines or a combination of CO and other chemical species allows one to constrain the physical conditions that give rise to CO emission. When these observations include optically thinner tracers like ^{13}CO , these constraints can be particularly powerful. Due to sensitivity considerations, most multiline data sets have been assembled for bright regions like galaxy centers (or starbursts, Section 7). From these data we have constraints on X_{CO} in bright regions with very different systematics than either virial or dust-based techniques.

Generally, these results indicate that X_{CO} lower than $X_{\text{CO},20} = 2$ is common but not ubiquitous in the bright, central regions of galaxies. This is in qualitative agreement with the independent Sandstrom et al. (2013) dust-based results already mentioned. For example, Israel, Tielas & Baas (2006) use large velocity gradient (LVG) modeling of multiple ^{12}CO , ^{13}CO , and $[\text{CII}]$ lines in the central region of M51. They find $X_{\text{CO},20} \approx 0.25\text{--}0.75$ in the central regions, in good agreement with earlier work by Garcia-Burillo, Combes & Gerin (1993). Israel (2009a,b) extends this work to the centers of ten bright and starburst galaxies, finding $X_{\text{CO},20} \sim 0.1\text{--}0.3$ (see also Israel et al. 2003, Israel & Baas 2001), again significantly lower than Galactic. Based on maps of the $^{12}\text{CO}/^{13}\text{CO}$ ratio across NGC 3627, Watanabe et al. (2011) argue for a similar central depression in X_{CO} , with dynamical effects associated with a galactic bar leading to broader line widths and optically thinner ^{12}CO emission. Using optically thin tracers and dust emission, Meier & Turner (2001, 2004) find that $X_{\text{CO},20} \approx 1\text{--}0.5$ in the centers of IC 342 and NGC 6946. Lower conversion factors are not a universal result, however. Utilizing high-resolution data, Schinnerer et al. (2010) found X_{CO} much closer to Galactic in the arms of M51, $X_{\text{CO},20} \approx 1.3\text{--}2.0$. They attribute the difference with previous studies to the implicit emphasis on GMCs in their high-resolution data, speculating that it removes a diffuse CO-bright component that would drive X_{CO} to lower values.

In addition to degeneracy inherent in the modeling, these line ratio-based techniques suffer from the fundamental bias of the virial mass technique. They are only sensitive to regions where CO is bright and so may miss any component of CO-faint H_2 . A handful of observations of low-metallicity dwarf galaxies have attempted to address this directly by combining CO and $[\text{CII}]$ observations, with $[\text{CII}]$ employed as a tracer of the CO-faint molecular regime (Maloney & Black 1988, Stacey et al. 1991). Poglitsch et al. (1995) find that the $[\text{CII}]$ -to-CO ratio in the 30 Doradus region of the LMC is $\sim 60,000$, roughly an order of magnitude higher than is observed in Milky Way star-forming regions or other star-forming spirals (e.g., Stacey et al. 1991). Israel et al. (1996) and Israel & Maloney (2011) also find high values elsewhere in the LMC and SMC, with large scatter in the ratio. Madden et al. (1997) find that regions in the Local Group dwarf IC 10 also exhibit very high $[\text{CII}]$ 158- μm emission compared to CO, 2–10 times that found in the Milky

Way. They argue that [CII] emission cannot be readily explained by the available ionized or H I gas and is, thus, an indicator of H₂ where CO is photodissociated. Hunter et al. (2001) present ISO measurements for several more dwarf irregular galaxies, showing that at least three of these systems also exhibit very high [CII]-to-CO emission ratios. Cormier et al. (2010) present a *Herschel* map of the 158- μ m [CII] line in NGC 4214, again showing very high [CII]-to-CO ratios ($\sim 20,000$ – $70,000$) that cannot be explained by emission from [CII] associated with ionized gas. Inferring physical conditions from the [CII] line requires modeling. When such calculations are carried out, they generally imply a massive layer on the PDR in which the dominant form of hydrogen is H₂ while carbon remains ionized as C⁺ (e.g., Madden et al. 1997, Pak et al. 1998).

Thus, detailed spectral line studies of CO-bright sources often, but not always, suggest lower X_{CO} in the bright central regions of galaxies. Meanwhile, at low metallicities, [CII] observations suggest an important reservoir of H₂ not traced by CO.

5.4. Synthesis: X_{CO} in Normal Galaxies

Taken together, the picture offered by extragalactic X_{CO} determinations in normal galaxy disks resembles that in the Milky Way writ large (Section 4.4). Virial masses, dust-based estimates, and spectral line modeling all suggest $X_{\text{CO},20} \approx 1$ – 4 in the disks of normal spiral galaxies. Systematics clearly still affect each determination at the 50% level, with physical effects likely adding to produce the factor-of-two dispersion. Given this, applying a Milky Way $X_{\text{CO}} = 2 \times 10^{20} \text{ cm}^{-2} (\text{K km s}^{-1})^{-1}$ with an uncertainty of ~ 0.3 dex appears a good first-brush approach for normal star-forming galaxies. This applies to galaxies where the CO emission is dominated by self-gravitating clouds or cloud complexes with masses dominated by H₂.

Several very strong lines of evidence, as well as simple arguments, show that X_{CO} increases sharply in systems with metallicities below $12 + \log[\text{O}/\text{H}] \approx 8.4$ (approximately one-half solar; Asplund et al. 2009). High spatial resolution virial estimates find approximately Galactic X_{CO} in low-metallicity clouds, but they are not sensitive to extended CO-faint H₂ envelopes, only to CO-bright regions. We expand on the dependence of X_{CO} on metallicity in Section 6. We caution about the usefulness of virial estimates on large spatial scales, particularly in low-metallicity galaxies. But even in normal galaxies, concerns exist about whether molecular cloud complexes and associations are bound and dominated by H₂ on large scales.

Finally, in the central parts of galaxies spectral line modeling suggests that X_{CO} is often, but not always, depressed in a manner similar to that seen in the Galactic center and in molecule-rich starbursts. Dust observations are consistent with this picture, revealing central depressions in X_{CO} in some galaxies. Broader line widths, increased excitation, and the emergence of a diffuse molecular medium likely contribute to more CO emission per unit mass, decreasing X_{CO} . We expand on this topic when we consider starbursts in Section 7.

6. X_{CO} AT LOW METALLICITIES

CO emission is frequently very faint or nonexistent in gas-rich, actively star-forming low-metallicity galaxies. This is true in absolute luminosity terms, with CO emission almost completely absent in low-mass dwarf irregular galaxies below metallicity of $12 + \log \text{O}/\text{H} \approx 8.0$ (Elmegreen, Morris & Elmegreen 1980; Tacconi & Young 1987; Taylor, Kobulnicky & Skillman 1998). Even when it is detected, as in the case of the very nearby SMC, CO is faint (Israel et al. 1986). CO is also faint in a normalized sense. The CO-to-FIR ratios in blue, vigorously star-forming dwarf galaxies are clearly lower than in spiral galaxies (Tacconi & Young 1987, Young et al. 1996), and the same applies to other star-formation rate tracers such as H α (Young et al. 1996). The CO

per unit starlight is also depressed in very low-mass dwarfs (e.g., Young & Scoville 1991), and the ratio of CO to HI is markedly decreasing for later morphological type (Young & Knezek 1989).

Very importantly for CO emission, the low metal abundance in these systems implies lower C and O abundances and low dust-to-gas ratios (e.g., Draine et al. 2007, Muñoz-Mateos et al. 2009). Both of these factors will exert a strong effect on the relative distributions of H₂ and CO. Dust serves as the site of H₂ formation and also provides much of the far-UV shielding necessary to prevent molecules that are not strongly self-shielding, such as CO, from photodissociating. Note that galaxy mass is strongly correlated not only with metallicity, but also with a number of other parameters that may affect the equilibrium abundance of H₂, such as spiral density waves and interstellar pressure, further complicating the picture of the relation between CO luminosity and molecular mass. The critical question is whether low CO luminosities indicate a true deficit of H₂ or merely the suppression of CO emission in low-metallicity environments.

Theoretical considerations, described below, lead us to expect a change in X_{CO} at low metallicities. Several strong lines of observational evidence, described in Section 5, also suggest that X_{CO} increases sharply in irregular, low-metallicity systems. Dust-based X_{CO} estimates, which are sensitive to the total gas present, return high values in such targets. The [CII]-to-CO ratio seems dramatically higher in dwarf irregular galaxies than in spiral galaxies, supporting the hypothesis of a reservoir of H₂ at low A_V where most carbon is locked in [CII] rather than CO. The star-formation rate (SFR)-to-CO ratio also increases, offering circumstantial evidence for star-forming gas not traced by CO.

6.1. Theoretical Expectations for Low-Metallicity Gas

Naively, one would expect that lower C and O would imply consequently fainter CO emission. Because CO is optically thick, however, its luminosity is determined by the emitting area and its brightness temperature and velocity spread. The dependence of X_{CO} on metallicity hinges fundamentally on how the relative sizes of the [CII] and CO-emitting regions change with lower heavy element and dust abundance (**Figure 8**; also see the discussion of cloud structure in Section 2.5). Maloney & Black (1988) carried out one of the first thorough analyses of the problem. Here we note the physical drivers for the location of bright CO emission and then discuss the implications for low metallicity.

The relative distributions of CO and H₂ will be a detailed function of the balance of formation and destruction of CO, processes discussed for diffuse and dense material by van Dishoeck & Black (1986, 1988) (see also Wolfire, Hollenbach & McKee 2010, their appendices B and C). CO formation proceeds mainly through the production of OH via ion-neutral reactions initiated by cosmic-ray ionization. Once OH is formed, the chemistry proceeds via ion-neutral reactions to form HCO⁺ followed by the dissociative recombination of HCO⁺ to form CO. The formation rates of CO thus depend on the abundance of C times the abundance of O. Because the rate of formation depends on the abundance of OH, the rate of destruction of OH by far-UV photons represents an additional limiting factor in setting the CO abundance (see, e.g., Wolfire, Hollenbach & McKee 2010, their appendix C).

At depths where the CO line originates, the destruction of CO proceeds mainly via photodissociation by far-UV radiation. These dissociations occur via line transitions between the ground state and predissociated excited electronic states. That is, the majority of the transitions to these excited electronic states result in dissociation rather than CO in bound, excited levels. The longest wavelength dissociating transition lies at $\lambda \approx 1,076 \text{ \AA}$. Thus, the dissociation of CO in the ISM occurs in the narrow far-UV band between $\lambda \approx 1,076 \text{ \AA}$ and the Lyman limit at $\lambda \approx 912 \text{ \AA}$. These dissociation bands for CO overlap the Lyman bands of H₂ and the Lyman lines of HI. Thus,

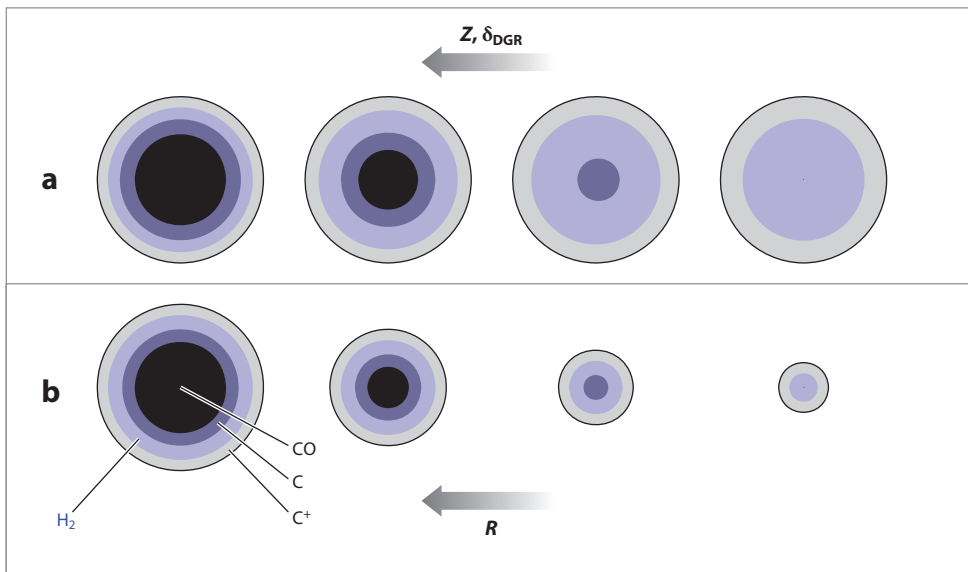


Figure 8

Effect of metallicity on CO and H₂ in a spherical clump immersed in a uniform radiation field. Blue shading indicates the region where the gas is molecular, according to Equation 25. Increasingly darker shading shows the regions where carbon is found as C⁺, C, or CO. Panel *a* illustrates the effect of decreasing metallicity and dust-to-gas ratio on the distribution of C⁺, CO, and H₂. Mostly because of the increase in N_{H} required to attain a given A_V , the CO-emitting region is pushed further into the clump until, for a fixed cloud size, it disappears at low enough metallicities. Panel *b* illustrates the effect of changing the clump size or column density at a fixed metallicity (adapted from Bolatto, Jackson & Ingalls 1999; Wolfire, Hollenbach & McKee 2010).

HI and H₂ can shield CO. Because CO dissociates in-line transitions, similar to H₂, it can also self-shield at sufficiently large CO column densities. In addition to gas opacity, dust absorption and scattering will attenuate the dissociating radiation field.

A simple expression illustrates the dependence of the CO dissociation rate on these various processes: $R = \chi R_0 \exp(-\gamma A_V) \Theta \text{ s}^{-1}$. The first two factors reflect the incident radiation field. R_0 is the dissociation rate in free space for a radiation field with a particular shape and χ is a scaling factor that measures the strength of the radiation field. The exponential factor reflects shielding by dust, with A_V the line-of-sight extinction into the cloud. The factor γ includes both cloud geometry and the translation from A_V into extinction at the dissociating wavelengths, accounting for absorption and scattering by grains in the far-UV. The parameter Θ accounts for shielding by HI and H₂ gas and CO self-shielding.

For a Draine (1978) ISRF, $R_0 = 2.6 \times 10^{-10} \text{ s}^{-1}$ (Visser et al. 2009); R_0 will vary for radiation fields with other shapes. For typical ISM grains and penetration into a plane parallel layer, $\gamma = 3.53$ (van Dishoeck, Jonkheid & van Hemert 2006). The parameter Θ is a monotonically decreasing function of the HI, H₂, and CO column densities and varies between 1 (for no shielding) and 0. A fit to the line overlap and self-shielding function, Θ , can be found in Visser et al. (2009).

Balancing CO formation and destruction, Wolfire, Hollenbach & McKee (2010) find an expression for the depth into a cloud at which $\tau_{\text{CO}} = 1$ for the $J = 1 \rightarrow 0$ transition:

$$A_V(R_{\text{CO}}) \simeq 0.102 \ln \left[3.3 \times 10^7 \left(\frac{\chi}{Zn} \right)^2 + 1 \right]. \quad (24)$$

Here, n is the gas density and χ and Z' are the far-UV field and gas phase abundances in units of the local Galactic values, respectively. $A_V(R_{\text{CO}})$ is the depth in units of magnitudes of visual extinction due to dust at which $\tau_{\text{CO}} = 1$. In this expression, the explicit dependence on dust-to-gas ratio cancels out, but the conversion from A_V to column density will depend on the dust-to-gas ratio.

Variations in X_{CO} will depend on the relative extent of the CO and H₂ layers. Therefore, Wolfire, Hollenbach & McKee (2010) present a similar expression for the depth at which the gas is half molecular,

$$A_V(R_{\text{H}_2}) \simeq 0.142 \ln \left[5.2 \times 10^3 \delta'_{\text{DGR}} \left(\frac{\chi}{\delta'_{\text{DGR}} n} \right)^{1.75} + 1 \right], \quad (25)$$

where δ'_{DGR} is the dust-to-gas ratio relative to the local Galactic value.

The difference between the depth of the H₂ and CO layers is thus: $\Delta A_V = 0.53 - 0.045 \ln \frac{\chi}{n} + 0.107 \ln(\delta'_{\text{DGR}}) - 0.204 \ln(Z')$. For a dust-to-gas ratio that scales as the gas phase metallicity we have

$$\Delta A_V = 0.53 - 0.045 \ln \frac{\chi}{n} - 0.097 \ln(Z'). \quad (26)$$

The equations for $A_V(R_{\text{CO}})$, $A_V(R_{\text{H}_2})$, and ΔA_V all show weak dependencies on χ , δ'_{DGR} , and Z' . Thus, they may be expected to change only weakly with changing local conditions; and at lower metallicity, the location of the $\tau_{\text{CO}} = 1$ surface, the H₂ transition, and the spacing between the two all remain approximately fixed in units of visual extinction due to dust. The ratio of dust to gas also drops with metallicity (Draine et al. 2007). As a consequence of lower dust abundance and approximately constant ΔA_V , the physical depth of the $\tau_{\text{CO}} = 1$ surface shifts deeper into the cloud, producing a larger surface layer of H₂ at low A_V . A correspondingly larger layer of HI also exists beyond $A_V(R_{\text{H}_2})$ but does not bear directly on this review. Thus, with lower metallicity and correspondingly lower dust abundance, CO retreats further into the cloud than H₂. **Figure 8** illustrates the expected interplay of HI, H₂, CO, and C⁺ in a spherical cloud and the impact of changing metallicity (**Figure 8a**) and cloud size or column density (**Figure 8b**).

If $M(R_{\text{H}_2})$ is the molecular mass within the radius where the molecular fraction is 0.5, and $M(\text{CO})$ is the mass within the radius of the $\tau_{\text{CO}} = 1$ surface, then the CO-faint gas fraction can be defined as $f = [M(R_{\text{H}_2}) - M(R_{\text{CO}})]/M(R_{\text{H}_2})$. For a cloud with an r^{-1} density profile, corresponding to $M(r) \propto r^2$, the CO-faint gas mass fraction is given by

$$f = 1 - \exp \left(\frac{-0.76 \Delta A_V}{\delta'_{\text{DGR}} \bar{N}_{22}} \right) = 1 - \exp \left(\frac{-4.0 \Delta A_V}{\bar{A}_V} \right), \quad (27)$$

where ΔA_V is the optical depth in the CO-faint gas layer (Equation 26), \bar{N}_{22} is the mean H column density in the CO portion of the cloud in units of 10^{22} cm^{-2} , and $\bar{A}_V = 5.26 \delta'_{\text{DGR}} \bar{N}_{22}$.

The retreat of the CO-emitting surface was first noted by early studies (Maloney & Black 1988, Lequeux et al. 1994). This shrinking CO core leads to lower beam filling factors, and thus a lower observed CO intensity (e.g., Pak et al. 1998; Bolatto, Jackson & Ingalls 1999). The result is that X_{CO} increases with decreasing metal abundance. Maloney & Black (1988) find nearly equal CO and H₂ cloud sizes at solar metallicity and so note that increasing CO abundance above solar does not substantially change X_{CO} . Recent observational estimates find the fraction of CO-faint molecular gas mass to be $\sim 50\%$ in the Milky Way (see Section 4.2.4). This allows slightly more room for a changing X_{CO} moving to supersolar metallicities. For example, a change from $X_{\text{CO},20} \approx 2$ to ~ 1.3 might be plausible due to the effect of increasing metallicity.

A secondary consideration is that the brightness temperature of CO may also be affected by systematic excitation changes with metallicity. The temperature of the gas represents a balance

between heating and cooling. If grain photoelectric heating dominates at the $\tau_{\text{CO}} = 1$ surface, then to first order both the heating rate (proportional to the dust-to-gas ratio for photoelectric heating) and the cooling rate (proportional to metal abundance for line cooling) will scale similarly with metallicity, yielding no change in gas temperature with metal abundance. It remains unclear, however, whether the photoelectric heating efficiency increases, decreases, or stays the same at low metallicities (e.g., Röllig et al. 2006, Israel & Maloney 2011).

In summary, models predict an increase in X_{CO} for large regions of low-metallicity galaxies due to the contraction of the CO-emitting surface relative to the area where the gas is H_2 for a fixed cloud size. This effect may be offset (or compounded) by a mild increase (or decrease) in brightness temperature brought about by changes in heating sources, chiefly the photoelectric heating effect. Note that the usefulness of CO as a tracer of total H_2 mass will ultimately break down at low enough metallicity, where it will be found only at the highest column densities and in well-shielded environments.

6.2. Metallicity-Dependent Calibrations of X_{CO}

Calibrating X_{CO} as a function of metallicity has represented a key goal of extragalactic CO studies for two decades. The issue remains complicated for several reasons: some practical, some theoretical. We have already discussed the biases and caveats of the different X_{CO} extragalactic estimators. On practical grounds, the faintness of CO in low-luminosity, low-metallicity systems renders observations very difficult. The abscissa in any calibration, metallicity, also remains one of the hardest quantities in extragalactic astronomy to measure with precision. The basic cloud structure arguments presented in Section 6.1 suggest that the sub- and supersolar regimes should be treated differently—or at least that a single power law represents a poor choice across all regimes. We discuss here several existing calibrations of X_{CO} with metallicity and contrast them against the data, presenting a simple tentative formula that includes metallicity effects in Section 9.

Some of the most comprehensive and widely used work comparing X_{CO} to metallicity relies mostly on virial mass-based X_{CO} estimates (e.g., Wilson 1995; Arimoto, Sofue & Tsujimoto 1996; Boselli, Lequeux & Gavazzi 2002; Bolatto et al. 2008). These calibrations should best be viewed as calibrations of X_{CO} within the CO-emitting region and not be used to predict the total H_2 content from CO on large scales. We suggest that the lack of an X_{CO} versus metallicity trend in Bolatto et al. (2008) and the weak trend in Wilson (1995) reflect the uniformity of opaque, bright CO-emitting structures across many types of galaxies. Similarly, the calibrations by Arimoto, Sofue & Tsujimoto (1996) and Boselli, Lequeux & Gavazzi (2002) rely on virial masses to derive X_{CO} as a function of metallicity (and so do those of Obreschkow & Rawlings 2009).

What are the appropriate calibrations to consider for X_{CO} as a function of metallicity? Dust-based approaches such as that used by Israel (1997a) or the alternative approach used by Boselli, Lequeux & Gavazzi (2002) or combined CO, [CII], and dust modeling (Madden et al. 1997, Pak et al. 1998) appear to offer the best, or at least the most accessible, extragalactic approaches. These have the potential to capture the whole H_2 distribution. In the following paragraphs, we employ these observations to test recent theoretical work on the subject (e.g., Glover et al. 2010; Wolfire, Hollenbach & McKee 2010; Feldmann, Gnedin & Kravtsov 2012; Narayanan et al. 2012). Note that, as discussed in Section 6.1, we do not expect X_{CO} to change significantly due to metallicity in the supersolar metallicity regime. Instead, variations due to optical depth, line width, or excitation temperature are likely to dominate.

Figure 9 presents an attempt at such a comparison. We show an ensemble of dust and FIR determinations (Israel 1997a, Madden et al. 1997, Leroy et al. 2007, Gratier et al. 2010, Bolatto et al. 2011, Leroy et al. 2011, Smith et al. 2012) targeting local galaxies along with X_{CO} estimates

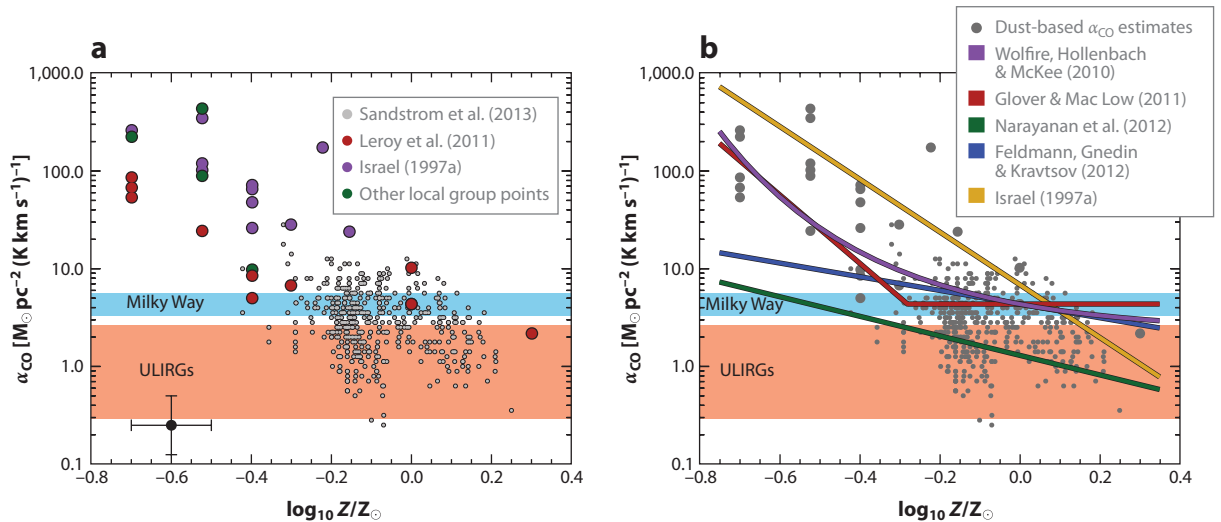


Figure 9

Conversion factor, estimated from dust-based approaches, as a function of gas-phase abundance. (a) Color points show estimates for very nearby galaxies [from Israel (1997a), Madden et al. (1997, based on [CII]), Leroy et al. (2007, 2011), Gratier et al. (2010), Roman-Duval et al. (2010), Bolatto et al. (2011), and Smith et al. (2012)]. Gray points show high-quality solutions from analysis of 22 nearby disk galaxies by Sandstrom et al. (2013), with typical uncertainties illustrated by the error bars near the bottom left corner. Metallicities are from Israel (1997a), Bolatto et al. (2008), and Moustakas et al. (2010) and quoted relative to solar in the relevant system [$12 + \log[\text{O}/\text{H}] = 8.7$ for the first two, $12 + \log[\text{O}/\text{H}] = 8.5$ for the latter, which uses the metallicity calibration by Pilyugin & Thuan (2005)]. Note that significant systematic uncertainty is associated with the x -axis. The color bands illustrate our recommended ranges in α_{CO} for the Milky Way and ULIRGs. (b) Colored lines indicate predictions for X_{CO} as a function of metallicity from the references indicated, normalized to $X_{\text{CO},20} = 2$ at solar metallicity where necessary. For these predictions, we assume that giant molecular clouds have $(\Sigma_{\text{GMC}}) = 100 M_{\odot} \text{pc}^{-2}$, which we translate to a mean extinction through the cloud using Equation 21. Dust-based determinations find a sharp increase in X_{CO} with decreasing metallicity below $Z \sim 1/3 - 1/2 Z_{\odot}$.

determined by Sandstrom et al. (2013) for a sample of 22 nearby disk galaxies. In **Figure 9b**, we plot theoretical predictions for X_{CO} as a function of metal abundance, assuming the dust-to-gas ratio is linearly dependent on metallicity. For Wolfire, Hollenbach & McKee (2010), we plot the equation

$$\frac{X_{\text{CO}}(Z')}{X_{\text{CO}}(Z' = 1)} = \exp \frac{+4.0 \Delta A_V}{Z' \bar{A}_{V,MW}} \exp \frac{-4.0 \Delta A_V}{\bar{A}_{V,MW}}, \quad (28)$$

which is obtained from Equation 27 assuming that the dust-to-gas ratio tracks metallicity. Here Z' is the abundance of heavy elements and dust relative to solar, $X_{\text{CO}}(Z' = 1)$ is the CO-to- H_2 conversion factor at solar metallicity, and $\bar{A}_{V,MW}$ is the mean extinction through a GMC at Milky Way metallicity ($\bar{A}_{V,MW} \approx 5$ for $\Sigma_{\text{GMC}} \approx 100 M_{\odot} \text{pc}^{-2}$). The prediction for Glover & Mac Low (2011) simply adapts their equation 16, which gives X_{CO} as a function of A_V . We assume that the mean extinction through a cloud scales as the metal abundance, $A_V = Z' \bar{A}_{V,MW}$

$$\frac{X_{\text{CO}}(Z')}{X_{\text{CO}}(Z' = 1)} = \begin{cases} 1 & \text{for } Z' \bar{A}_{V,MW} > 3.5 \\ (Z' \bar{A}_{V,MW})^{-3.5} & \text{for } Z' \bar{A}_{V,MW} < 3.5 \end{cases} \quad (29)$$

In the full prediction of Narayanan et al. (2012), X_{CO} depends on a combination of I_{CO} and Z , rather than metallicity alone. We cannot readily place their predictions in this plot. Instead, we plot their equation 6, in which X_{CO} depends on Z' and Σ_{H_2} . For each of these predictions, we assume $\Sigma_{\text{H}_2} = 100 M_{\odot} \text{pc}^{-2}$, translating this to $A_{V,0}$ assuming $R_V = 3.1$ and the dust-to-gas ratio

of Bohlin, Savage & Drake (1978). We also plot the metallicity-only fit by Israel (1997a; note that his fit includes the radiation field, with a definition that renders it heavily degenerate with the dust-to-gas ratio).

Figure 9 shows large scatter, even among determinations using similar techniques for the same galaxy, but provides reasonable evidence for an upturn in X_{CO} with decreasing metallicity below $Z' \sim 1/3 - 1/2$. The fit by Israel (1997a) skirts the upper envelope of measured values, whereas the prediction by Feldmann, Gnedin & Kravtsov (2012) predicts weaker-than-observed variations at very low Z' , though data remain scarce (those points represent only about four galaxies). The sharp nonlinear increases predicted by shielding-oriented models like that of Wolfire, Hollenbach & McKee (2010) or the simulations of Glover & Mac Low (2011) provide the best fits to the existing data.

Less direct approaches to constrain X_{CO} also exist. A recently popular technique is to assume an underlying relationship between star formation and molecular gas and to use this relationship and an estimate of the recent SFR to calculate the H_2 present. Schruba et al. (2012) applied this technique to estimate X_{CO} as a function of metallicity in a sample of nearby galaxies. Genzel et al. (2012) combined a wide set of low- and high-redshift measurements to estimate the dependence of X_{CO} on metallicity. Both studies find a significant dependence of X_{CO} on metallicity but with a wide range of possible power-law exponents, $X_{\text{CO}} \propto Z^1$ to Z^3 . The strength of this approach is that the observations needed to make such estimates are widely accessible. The weakness, of course, is that it requires assuming an underlying relationship between H_2 and star formation. Any true dependence of the star-formation efficiency on metallicity, or any other quantity covariant with metallicity, will be recast as additional variations in X_{CO} .

In the low metallicity, high X_{CO} regime, our knowledge of the distribution function of molecular column density will present a practical limit to the usefulness of CO as a tracer of H_2 . At metallicities perhaps as high as one-half solar, half of the H_2 mass will exist outside the CO-emitting surface, and that fraction will rapidly increase for decreasing metallicity. Thus, application of a CO-to- H_2 conversion factor at very low metallicity ultimately involves extrapolating the total mass of a cloud from only a small inner part; by $Z' \sim 0.1$, this may already be analogous to measuring the total H_2 mass of a Milky Way cloud from HCN emission or some other high-density tracer. In the Milky Way, the fraction of cloud mass in high column density lines of sight can vary dramatically from cloud to cloud (e.g., Kainulainen et al. 2009; Lada, Lombardi & Alves 2010). In the LMC, Israel et al. (1996) found large region-to-region variations in the $[\text{CII}]$ -to-CO ratio. As one moves to increasingly low metallicities, the use of CO emission to quantify the H_2 reservoir becomes more and more extrapolative. Although difficult to quantify, this effect should add significant scatter that increases with decreasing metallicity and will eventually present a practical floor past which CO is not a useful tracer of total H_2 mass.

7. X_{CO} IN STARBURSTS AND OTHER LUMINOUS GALAXIES

Molecular gas in starbursts exists under conditions very different from those found in most normal galaxies. Observations of starbursts suggest widespread gas volume and column densities much higher than those typical of normal disks (e.g., Jackson et al. 1995, Iono et al. 2007). Molecular gas in starbursts is also warmer, exciting higher rotational transitions than those found in less active objects (e.g., Bradford et al. 2003, Ward et al. 2003, Rangwala et al. 2011). In fact, a negative correlation is observed between molecular gas depletion time (a parameter that characterizes how long a galaxy can maintain its current SFR) and excitation (e.g., Paglione, Jackson & Ishizuki 1997). Similarly, a positive correlation exists between gas density and SFR (e.g., Gao & Solomon

2004). These observations show that there is a fundamental relation between the density and temperature of the molecular gas and the existence of starburst activity, such that the gas present in starbursting galaxies or regions has higher densities and temperatures than those prevalent in quiescent systems.

What are the effects of higher temperatures, densities, and column densities on X_{CO} ? To first order, higher gas temperatures yield brighter CO emission, decreasing X_{CO} . Note, however, that while increasing the temperature decreases X_{CO} , increasing the density and surface density of the self-gravitating clouds of gas has the opposite effect, increasing X_{CO} (see Equations 11, 12, and 15). Therefore we expect a certain level of compensation to occur, lessening the impact of environment on the conversion factor as long as most of the CO emission arises from GMCs. In regions where the average gas density is comparable to that of a GMC, however, the entire medium will turn molecular and CO emission will originate from an extended warm phase. These conditions are thought to be prevalent throughout the active regions of the brightest starbursts, such as ULIRGs. In addition, many of these luminous galaxies are mergers or the starbursts occur in regions such as galaxy centers. The gas correspondingly experiences motions in excess of the velocity dispersion due to its self-gravity. The large column densities conspire to make the medium globally optically thick, thus setting up the conditions discussed in Section 2.3. In this situation, the CO emission will be disproportionally luminous, driving X_{CO} to lower values.

We can quantitatively explore this scenario with PDR model calculations (adapted from Wolfire, Hollenbach & McKee 2010), which incorporate self-consistently the chemistry, heating, and radiative transfer. Setting up a typical Milky Way GMC (a virialized structure of size ~ 30 pc with $\Sigma_{\text{mol}} \approx 170 M_{\odot} \text{ pc}^{-2}$ and $M \approx 1 \times 10^5 M_{\odot}$), we reproduce a Galactic X_{CO} . In a ~ 160 -pc virialized cloud with $\Sigma_{\text{mol}} \approx 10^4 M_{\odot} \text{ pc}^{-2}$ and $M \approx 2 \times 10^8 M_{\odot}$ (representing the molecular structures observed in existing high-resolution observations of ULIRGs) under the same Galactic conditions, we obtain $X_{\text{CO},20} \sim 80$ in rough agreement with Equation 11. Increasing the gas velocity dispersion to include $2 \times 10^9 M_{\odot}$ of stars (see Section 2.3), and increasing the UV and cosmic-ray fluxes by 10^3 to account for the larger SFR, decreases the conversion factor to $X_{\text{CO},20} \sim 0.6$. Most of this effect is due to the velocity dispersion: Increasing the UV and cosmic ray fluxes by only 10 with respect to the Galactic case yields $X_{\text{CO},20} \sim 2$, which is still much lower than the starting value of 80.

Narayanan et al. (2011) explore these effects in detail using a series of computational models of disks and merging galaxies. They find that X_{CO} drops throughout the actively star-forming area in merger-driven starbursts due to increased gas temperatures (caused in part by collisional thermal coupling between dust and gas, which occurs at high densities) and the very large velocity dispersion in the gas (in excess of self-gravity), which persists for at least a dynamical time after the burst. The magnitude of the drop in X_{CO} depends on the parameters of the merger, with a large X_{CO} corresponding to a low-peak SFR. Thus, the large drop in X_{CO} occurs in massive mergers during the starburst phase, and X_{CO} settles to normal values when the star-formation activity and the conditions that caused it subside. The simulated normal disk galaxies experience less extreme conditions of density and turbulence, and accordingly possess higher values of X_{CO} except in their centers. The mean values of the CO-to- H_2 factor for the simulated mergers and disks are $X_{\text{CO},20} \approx 0.6$ and 4, respectively, with a very broad distribution for the mergers. In a follow-up study, Narayanan et al. (2012) introduce a calibration of X_{CO} that becomes a function of $W(\text{CO})$ as well as metallicity, Z . This calibration captures the fact that the factors that cause a drop in X_{CO} occur increasingly at higher surface densities. Note, however, that because X_{CO} is a nonlinear function of $W(\text{CO})$ obtained from luminosity-weighted simulations, the calibration must be applied carefully to observations. The observed CO intensity corresponds to the intrinsic intensity multiplied by a filling factor of $f_{\text{beam}} < 1$, whereas the luminosity-weighted $W(\text{CO})$

employed by the model-derived calibration is much closer to the intrinsic CO intensity, which is not directly observed because observations do not completely resolve the source.

In the following sections, we discuss the observational findings in starburst galaxies in the local Universe.

7.1. Luminous Infrared Galaxies

One of the earliest comprehensive studies of the state of the molecular gas and the value of X_{CO} in a LIRG was performed on the prototypical starburst M82. Wild et al. (1992) use multitransition observations and detailed excitation calculations to determine the proportionality between the optically thin C^{18}O emission and the H_2 column density. Bootstrapping from this result, they find that X_{CO} varies across the disk of M82 and is in the range of $X_{\text{CO},20} \approx 0.5$ –1. They attribute this low X_{CO} mostly to high temperatures, as they estimate $T_{\text{kin}} > 40$ K for the bulk of the gas from their modeling. Using a similar technique, Papadopoulos & Seaquist (1999) analyze the inner region of NGC 1068, a well-known starburst with a Seyfert 2 nucleus. They conclude that a diffuse, warm, molecular phase dominates the ^{12}CO emission, whereas the mass is dominated by a denser phase that is better observed in the C^{18}O isotopologue. The $^{12}\text{CO } J = 1 \rightarrow 0$ emission from the diffuse phase has low optical depth ($\tau_1 \sim 1$ –2) and is not virialized; thus, it is overluminous with respect to its mass. They argue that the CO-to- H_2 conversion factor in the nuclear region is $X_{\text{CO},20} \sim 0.2$ –0.4, although the precise value depends critically on the assumed CO abundance.

Along similar lines, Zhu, Seaquist & Kuno (2003) perform a multitransition excitation study of molecular gas in the Antennae pair of interacting galaxies (NGC 4038/9). They find that the H_2 gas mass in their analysis depends critically on the $^{12}\text{CO}/\text{H}_2$ abundance ratio, which is an input to their model. They conclude that $^{12}\text{CO}/\text{H} \sim 0.5$ – 1×10^{-4} , and consequently $X_{\text{CO},20} \sim 0.2$ –0.4 for the center of NGC 4038 and $X_{\text{CO},20} \sim 0.5$ –1 for the overlap region between both galaxies. They argue that the adoption of this smaller-than-standard X_{CO} is consistent with the gas distribution, including H I , in the interacting pair, whereas the very large mass for the overlap region that would result from adopting a standard X_{CO} would be very difficult to reconcile with the gas dynamics. These researchers find that their excitation analysis points to gas with high velocity dispersion, large filling fraction, and low optical depth as the reason for why CO is overluminous in the Antennae. Recently, Sliwa et al. (2012) also find low X_{CO} in their excitation and dynamical analysis of Arp 299 using interferometric data, $X_{\text{CO},20} \approx 0.2$ –0.6.

The broad conclusions of these in-depth studies are in agreement with findings from studies carried over large samples. Yao et al. (2003) survey 60 local IR-luminous (starburst) galaxies spanning FIR luminosities $L_{\text{FIR}} \sim 10^9$ – $10^{12} L_{\odot}$, analyzing their $^{12}\text{CO } J = 1 \rightarrow 0$ and $J = 3 \rightarrow 2$ emission. Using the dust temperature as a proxy for the gas temperature, and assuming coextensive emission and a CO/ H_2 abundance ratio similar to what would be expected if all the gas-phase carbon were locked in CO molecules for Milky Way abundances, they conclude that $X_{\text{CO},20} \sim 0.3$ –0.8 is consistent with the available data.

Papadopoulos et al. (2012) perform a detailed analysis on another large sample of LIRGs, with $L_{\text{FIR}} \gtrsim 10^{11} L_{\odot}$. They find that one-phase radiative transfer models generally match the observations for the lower J transitions of CO with a typical $X_{\text{CO},20} \sim 0.3$ [$\alpha_{\text{CO}} \approx 0.6 \pm 0.2 M_{\odot} (\text{K km s}^{-1} \text{ pc}^2)^{-1}$], a value compatible with previous studies (e.g., Downes & Solomon 1998). Papadopoulos and colleagues conclude that although the gas temperature is partially responsible for the lower X_{CO} , the most important factor is the gas velocity dispersion. They also point to a caveat with this result, which has to do with the possible existence of a dense, bound phase with lower velocity dispersion and a much higher X_{CO} . This phase is associated with dense gas tracers such as high- J CO or heavy rotor molecules (HCN , CS , HCO^+). It has the potential to dominate

the molecular mass of the system and raise the conversion factor to $X_{\text{CO},20} \sim 2-6$. Because the uniqueness of this explanation for the observed excitation is unclear, and the derived masses conflict in some cases with dynamical mass estimates, we consider the results of multicomponent models an interesting topic for further research. Papadopoulos and colleagues also point out that although the global $\text{CO } J = 1 \rightarrow 0$ luminosity is dominated by the warm, low X_{CO} component, it is possible to hide a cold, normal X_{CO} component that could add a significant contribution to the molecular mass of the system. This component would most likely be spatially distinct, for example an extended molecular disk, and thus could be separated in high spatial resolution studies with interferometers.

7.2. Ultraluminous Infrared Galaxies

ULIRGs are extreme cases of dust-enshrouded starbursts and AGN, with FIR luminosities in excess of $L_{\text{FIR}} \sim 10^{12} L_{\odot}$. These objects are the products of gas-rich major mergers and possess very large CO luminosities (Mirabel & Sanders 1988, Sanders & Mirabel 1996). Despite that, their $L_{\text{FIR}}/L_{\text{CO}}$ ratios frequently exceed those found in spiral galaxies, including interacting pairs, and Milky Way GMCs. The fundamental question is how those CO luminosities relate to their molecular gas masses. Understanding X_{CO} in ULIRGs is particularly interesting because they likely provide the best local templates for the most luminous high-redshift submillimeter galaxies, which have very high SFRs compared to other galaxies of similar stellar mass at their redshift (i.e., are off the main sequence; Tacconi et al. 2006, Narayanan et al. 2010).

Studies presented in a series of papers (Downes, Solomon & Radford 1993; Bryant & Scoville 1996, 1999; Solomon et al. 1997; Downes & Solomon 1998) show that the molecular gas masses obtained for ULIRGs using the Galactic disk CO-to- H_2 conversion factor are uncomfortably close to (or exceed) their dynamical masses, suggesting that the Galactic X_{CO} overestimates their total molecular mass. These researchers develop a consistent one-component model that explains the high-resolution observations as rotating, highly turbulent remnants of the merging process. The CO emission is dominated by low-density gas, and although it is optically thick it is only moderately so (for example, see also Iono et al. 2007). This lower molecular mass is consistent with the observed (optically thin) millimeter dust continuum emission for Galactic dust-to-gas ratio. The typical X_{CO} they derive is $X_{\text{CO},20} \sim 0.4$, approximately a factor of five lower than in the Milky Way disk [$\alpha_{\text{CO}} \sim 0.8 M_{\odot} (\text{K km s}^{-1} \text{ pc}^2)^{-1}$, with individual results ranging between 0.3 and 1.3 in table 9 of Downes & Solomon 1998].

Detailed high-resolution studies of individual ULIRGs find similar results. Bryant & Scoville (1996, 1999) study the kinematics of seven LIRGs and ULIRGs, determining interferometric sizes and dynamical masses. They conclude that the use of a Milky Way conversion factor results in molecular masses larger than the dynamical mass of the system in the cores of all seven objects, although in some cases that can be explained away assuming a face on orientation. They find $X_{\text{CO},20} < 0.7$ and $X_{\text{CO},20} < 1.5$ for Mrk 231 and NGC 6240, respectively. Modeling the CO kinematics of Arp 220, including the effects of the stellar components in the dynamics of the nuclear disk, Scoville, Yun & Bryant (1997) find $X_{\text{CO},20} \sim 1$. These estimates are comparable with those from one-component radiative models for the same galaxies, and typically much lower than the two-component results (Downes & Solomon 1998, Papadopoulos et al. 2012).

7.3. Synthesis: X_{CO} in Starbursts

There has been much recent progress, through both observations and modeling, on the determination of X_{CO} in starbursts. Studies of CO excitation in large samples, as well as detailed studies of individual cases, strongly point to lower than Galactic values of X_{CO} , particularly in extreme

starbursts such as ULIRGs. These low values of X_{CO} are driven by a globally molecular medium coupled with high gas temperatures and, more importantly, very high velocity dispersions in the CO-emitting gas due to a combination of merger activity and the stellar potential (Narayanan et al. 2011, Papadopoulos et al. 2012). The standard practice has been to adopt $\alpha_{\text{CO}} \approx 0.8 M_{\odot} (\text{K km s}^{-1} \text{pc}^2)^{-1}$ (Downes & Solomon 1998), a value similar to $\alpha_{\text{CO}} \approx 0.6 \pm 0.2 M_{\odot} (\text{K km s}^{-1} \text{pc}^2)^{-1}$ resulting from recent one-component modeling in a large sample (Papadopoulos et al. 2012). Note, however, that this is an average value and there are likely large galaxy-to-galaxy variations (Narayanan et al. 2011). To first order, these variations should be mostly related to the total surface density of the galaxy, if the gas is bound and experiencing the global gravitational potential (cf. Equation 16). We use this to suggest a tentative X_{CO} correction in Section 9.

Large uncertainties exist in the estimates from observations, stemming from assumptions about $^{12}\text{CO}/\text{H}_2$ and $^{12}\text{CO}/^{13}\text{CO}$ ratios, coextensive emission in the different transitions, and the general need for simplifications in excitation models. Note also, as a persistent caveat, that there is the possibility of hiding significant molecular mass in ULIRGs in a low velocity dispersion, dense component. This possibility, however, seems disfavored in some cases, where high-quality dynamical estimates are available.

8. X_{CO} AT HIGH REDSHIFTS

The improved sensitivity of millimeter- and centimeter-wave instruments has allowed detection of CO emission from an increasingly diverse range of systems out to higher and higher redshifts. Most of the objects observed in CO to date represent the bright, rare end of the luminosity distribution: so-called submillimeter galaxies (SMGs) and quasi-stellar object (QSO) hosts. Some recent studies, however, target rotating disks that lie at the high-mass end of the star-forming blue sequence at their redshift (i.e., have typical SFRs given their stellar mass—we refer to them here as main-sequence galaxies). CO observations thus now begin to sample the regime of main-sequence galaxies (Daddi et al. 2010b, Tacconi et al. 2010) and will expand to lower luminosity systems over the next decade.

Estimating molecular gas masses is frequently the main goal of CO observations at high redshifts. Unfortunately, direct determination of X_{CO} in high-redshift objects remains tremendously challenging. An additional complicating factor is that most high-redshift observations do not measure the $J = 1 \rightarrow 0$ transition of CO but rather higher rotational transitions. Thus, translating these measurements into molecular masses requires, at least in principle, understanding CO excitation in addition to the other physics governing X_{CO} .

At this stage, the modeling of optically thin isotopologues (e.g., Papadopoulos et al. 2012) may offer the best opportunity for direct X_{CO} measurements at high redshift. Such observations have been too costly to undertake and, even with ALMA, may only be practical for the brightest objects. Dust continuum observations offer another route to estimate molecular masses, although their application at high redshift requires understanding dust-to-gas ratios in relation to metallicities—a complex problem that ultimately requires knowledge of the balance of ISM enrichment, dust production, and destruction processes in galaxies. In lieu of direct measurements, the best route is to understand the physical drivers of X_{CO} and to apply knowledge acquired from local galaxies to systems at high redshift.

8.1. Observed CO Line Ratios

The ratio of the $J = 3 \rightarrow 2$ to $J = 1 \rightarrow 0$ transition, $r_{31} \equiv T_3/T_1$, exhibits a wide range of values across galaxies and has been observed at both low and high redshifts. Mauersberger et al. (1999) and Yao et al. (2003) consider r_{31} for large samples of nearby galaxies with IR luminosities

of $9 \lesssim \log(L_{\text{FIR}}) \lesssim 12$. They find a mean $r_{31} \approx 0.63$ – 0.66 (median $r_{31} \sim 0.5$) and a broad distribution of values. No strong correlations between r_{31} and dust temperature or luminosity are evident, but they note that r_{31} increases with increasing concentration and star-formation efficiency [measured as $L_{\text{FIR}}/M(H_2)$, though they note the CO intensity in the denominator]. Iono et al. (2009) examine 15 luminous LIRGs and ULIRGs with $\log(L_{\text{FIR}}) \gtrsim 11.5$ and find mean $r_{31} \approx 0.48$ (median 0.4) integrated over whole galaxies, with a higher mean $r_{31} \approx 0.96$ at the location of peak CO emission. Mao et al. (2010) discuss r_{31} in a sample of over 60 galaxies, finding that barred galaxies and starbursts have the higher averaged r_{31} values ($r_{31} \sim 0.89 \pm 0.11$ for starbursts), followed by AGNs (see their table 4). More recently, Papadopoulos et al. (2011) report the results of a large sample of LIRGs and ULIRGs composed of new observations and literature compilation, where they find mean $r_{31} \approx 0.67$ and $r_{21} \approx 0.91$. By contrast with these samples of active galaxies, the inner portion of the Milky Way has a ratio of $r_{31} \approx 0.28 \pm 0.17$ (Fixsen, Bennett & Mather 1999), denoting a correspondingly lower excitation in a $z = 0$ normal star-forming galaxy.

To first order, r_{31} offers a tool to distinguish excited, star-forming gas similar to that seen in LIRGs and ULIRGs from the gas found in more normal systems like the Milky Way. As emphasized by a number of researchers, however, these line ratios are hardly unambiguous indicators of local conditions. For example, Papadopoulos et al. (2011) show that for their sample of LIRGs and ULIRGs possible densities and temperatures are often poorly constrained, with data allowing high-density ($n \sim 10^4 \text{ cm}^{-3}$) and normal-temperature ($T_{\text{kin}} \sim 20 \text{ K}$) or low-density ($n \sim 300 \text{ cm}^{-3}$) and high-temperature ($T_{\text{kin}} \sim 150 \text{ K}$) solutions. Note as a limitation the assumption of similar filling fractions for galaxy-wide averages in all transitions, whereas high-resolution maps frequently find excitation gradients. It is thus key to appreciate that r_{31} , although useful as a first-order excitation indicator, combines the effects of both excitation and beam filling.

With the improving sensitivity of the available instrumentation, measurements of line ratios including CO $J = 1 \rightarrow 0$ at high redshift are rapidly increasing. For SMGs, the presumed high-redshift simile of local ULIRGs, the measured line ratios resemble those found for local LIRGs and ULIRGs. Harris et al. (2010), Swinbank et al. (2010), and Ivison et al. (2011) report means $r_{31} \approx 0.68$, 0.66 , and 0.55 , respectively, for a handful of SMGs. Carilli et al. (2010) and Bothwell et al. (2013) note that fitting observed SMG spectral line energy distributions requires a cool and a warm component, with most of the mass in the former. Riechers et al. (2011b) find low integrated $r_{41} \approx 0.25$ – 0.6 in two SMGs, noting the existence of excitation gradients, with CO $J = 1 \rightarrow 0$ in a more extended distribution than the higher transition. At the brightest end of the galaxy distribution Riechers et al. (2011a) report $r_{31} \sim 0.96$ – 1.06 for four high-redshift SMGs hosting quasars, suggesting that the excitation in these sources is such that the emission is thermalized to higher rotational transitions (see also Weiss et al. 2007 for a CO excitation discussion of a number of bright SMG and QSO-host high-redshift galaxies).

The lowest galaxy luminosities currently probed by high-redshift CO observations correspond to the high-luminosity end of the star-forming galaxy main sequence. Unlike SMGs or local ULIRGs, these systems are not major mergers. Excitation data remain scarce for these main-sequence disk galaxies. Dannerbauer et al. (2009) observed a *BzK* galaxy at $z \approx 1.5$ and report $r_{32} \sim 0.5$ and $r_{21} \sim 0.6$. Aravena et al. (2010) report $r_{31} \approx 0.61$ and $r_{21} \sim 0.4$ – 1.2 in a few *BzK* galaxies. These observations have large uncertainties, but suggest that the conditions in high- z disk galaxies are not as extreme as those in local ULIRGs. As a counterpoint, Riechers et al. (2010) discuss the CO $J = 1 \rightarrow 0$ detection of two highly magnified ($\mu \sim 30$) low-mass galaxies, where they find $r_{31} \approx 0.72$ and 0.78 with errors of ~ 0.2 , suggesting higher excitation than the previous examples if there is no differential lensing. For further discussion, see the review by Carilli & Walter (2013) in this volume.

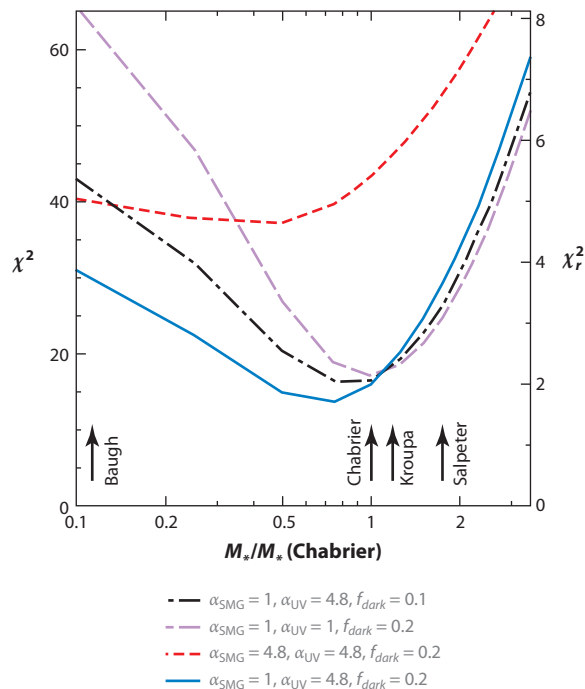


Figure 10

Minimization of the difference between dynamical mass and the sum of the gaseous, stellar, and dark matter components for a sample of nine high- z galaxies with high-quality data, dominated by submillimeter galaxies (SMGs) (Tacconi et al. 2008). χ^2 and reduced χ_r^2 (left and right axes, respectively) are shown here as a function of chosen initial mass function, for different gas (α) and dark matter (f_{dark}) parameters. The analysis distinguishes between α in the SMG subsample (α_{SMG}) and in the elected subsample (α_{UV}) of lower mass galaxies.

8.2. Estimates of X_{CO} in High-Redshift Systems

A number of observational studies have considered the problem of X_{CO} in high-redshift sources, combining line ratio measurements, consistency arguments, and scaling relations to argue for plausible values. Tacconi et al. (2008) discuss the values of X_{CO} applicable to a sample of high- z star-forming galaxies dominated by SMGs but also including lower mass galaxies. Allowing for a dark matter contribution of 10%–20% within a 10-kpc radius, they minimize the χ^2 of the difference between the dynamical mass and the sum of the stellar, gas, and dark matter. They find a Galactic X_{CO} to be strongly disfavored, whereas a smaller, ULIRG-like $X_{\text{CO},20} \approx 0.5$ produces much more satisfactory results for SMGs (Figure 10).

In their SMG sample, Ivison et al. (2011) find $X_{\text{CO},20} \sim 0.9 - 2.3$ to be compatible with the observed star-formation histories and dynamical and stellar masses. They argue for lower $X_{\text{CO},20} \lesssim 0.5$ in most cases, however, based on star-formation efficiency considerations. They decompose the molecular gas into a warm, star-forming phase (with intrinsic $r_{31} \sim 0.9$) and a cold, quiescent phase ($r_{31} \sim 0.3$) and invoke an approximately maximal starburst for the star-forming phase. The maximal starburst, $L_{\text{IR}}/M(\text{H}_2) \approx 500 L_{\odot} M_{\odot}^{-1}$, represents the largest allowed ratio of star formation to H_2 before radiation pressure disperses a starburst (e.g., Thompson, Quataert & Murray 2005).

Although Tacconi et al. (2008) and Ivison et al. (2011) point to similarities between ULIRGs and SMGs, we note that Bothwell et al. (2010) find that several SMGs have gas distributions

(imaged in $J \geq 3$ transitions) more extended than those of local ULIRGs. This may suggest that local ULIRGs may not be the best analogs of SMGs and that some SMGs may not arise from major mergers. The excitation gradients seen by Ivison et al. (2011) and Riechers et al. (2011a) also point to extended quiescent gas reservoirs in SMGs that are not frequently observed in local ULIRGs.

Daddi et al. (2010a) and Genzel et al. (2010) study high-redshift galaxies selected from optically identified objects at $z \sim 1.2$ – 2.2 . These are still massive systems, but drawn from the main sequence at their redshifts rather than major merger-driven starbursts. Kinematically, most of these systems are extended rotating disks, although with larger velocity dispersions than local disks. Daddi et al. (2010b), Genzel et al. (2010), and Tacconi et al. (2010) argue that because their CO emission likely arises from collections of self-gravitating GMCs (as suggested by local estimates of Toomre Q ; Genzel et al. 2011) with modest temperatures $T \sim 20$ – 35 K, these systems have Galactic X_{CO} . Additional constraints come from dynamical measurements that, together with simulations and modeling of the stellar populations, yield a gas mass resulting in $X_{\text{CO},20} \approx 1.7 \pm 0.4$, a value considerably higher than observed in ULIRGs or estimated for SMGs (Daddi et al. 2010a). Note that these researchers also provide a calibration for the dynamical mass estimation in this type of galaxy.

A different approach to quantifying the amount of gas in a galaxy is to try to use the continuum dust emission. Magdis et al. (2011) use this approach in two very well-studied high- z galaxies, a massive SMG at $z \sim 4$ and a main-sequence disk star-forming galaxy at $z \sim 1.5$. They take advantage of the well-characterized SEDs of these objects to calculate their dust masses employing different approaches to dust modeling (traditional modified blackbody as well as the type of models used by Draine et al. 2007). This dust mass is converted into a gas mass (assumed to be dominated by molecular gas) using a metallicity derived through the corresponding SFR-mass-metallicity relation (e.g., Mannucci et al. 2010) and assuming a Galactic dust-to-gas ratio corrected (approximately linearly) by metallicity. The result is $X_{\text{CO},20} \sim 0.4 \pm 0.2$ for the SMG, and $X_{\text{CO},20} \sim 1.9 \pm 1.4$ for the disk galaxy. Magnelli et al. (2012) follow a similar procedure in a mixed sample of 17 high- z galaxies, including merger-like and main-sequence disks, finding values of X_{CO} consistent with Galactic for the main-sequence disks and a factor of several lower for the merger-like galaxies. They also find $X_{\text{CO}} \propto T_{\text{dust}}^{-0.8}$, similar to the result expected from Equation 12.

Although this new use of dust observations at high redshift is promising, we caution that going from dust SEDs to gas masses involves a large chain of assumptions that is fraught with potential problems. At a fundamental level, we are far from understanding the dust creation-destruction balance that sets the dust-to-gas ratio in galaxies (e.g., Draine 2009, Dwek & Cherchneff 2011, and references therein). Moreover, the translation of an SED into a dust mass relies almost entirely on dust grain properties (composition, mass emissivity, size distribution) that have been derived for the Milky Way (Draine & Li 2001, 2007) and are extremely uncertain even for local galaxies (e.g., Galliano et al. 2011). Note that the self-consistent dust-based X_{CO} estimates discussed in Section 5.2 are emphasized precisely because they are free to a large degree from these problems. Nonetheless, this is an interesting approach that reinforces what seems to be the outstanding trend discussed above: ULIRG-like conversion factors for SMG (merger) galaxies and Milky Way-like conversion factors for disks at high redshift.

Genzel et al. (2012) present 44 low-mass high-redshift galaxies, showing that observations are starting to probe the low-metallicity regime at high redshift. These researchers find the effect that we have already discussed for local low-metallicity galaxies in Section 6, where CO is disproportionately faint for the star-formation activity (**Figure 11**). By assuming that these galaxies obey the same gas surface density to star-formation relation observed in local disks (e.g., Leroy et al. 2008), Genzel and colleagues estimate H_2 masses and derive a metallicity-dependent

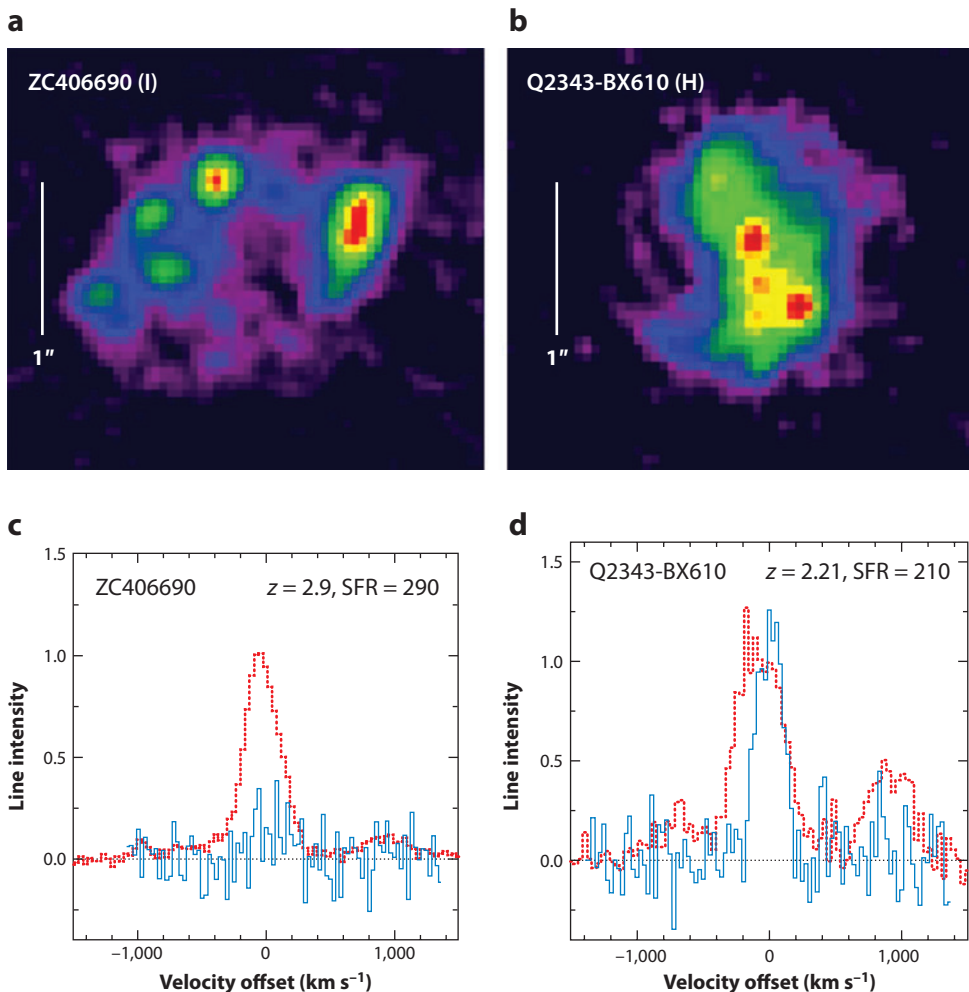


Figure 11

Metallicity effects in high-redshift main-sequence galaxies (Genzel et al. 2012). (*a,b*) Show rest-frame $H\alpha$ images of ZC406690 and Q2343-BX610, two $z \sim 2$ galaxies with similar rotational velocities ($v_{rot} \approx 224$ and 216 km s^{-1} , respectively), star-formation rates ($SFR \approx 480$ and $212 \text{ M}_{\odot} \text{ year}^{-1}$, including extinction correction), and stellar masses ($M_{*} \approx 4.3$ and $17 \times 10^{10} \text{ M}_{\odot}$). (*c,d*) Show the corresponding rest frame optical spectra containing the $H\alpha$ and $[\text{NII}]$ transitions at 6563 \AA and 6585 \AA (red), and the $\text{CO } J = 3 \rightarrow 2$ emission (blue). The galaxy ZC406690 has a low metallicity, indicated by a low $[\text{NII}]/H\alpha$ ratio, and a correspondingly low CO emission despite its large $H\alpha$ flux and star-formation activity.

calibration for X_{CO} at high redshift. They find $X_{\text{CO}} \propto Z^{-1.3} - Z^{-1.8}$, in approximate agreement with local measurements (Leroy et al. 2011, Schruba et al. 2012).

8.3. Synthesis: X_{CO} at High Redshift

Estimates of the appropriate X_{CO} for high-redshift galaxies rely largely on scaling and consistency arguments. Because they probe the physical state of the molecular gas, line ratio measurements represent a particularly powerful tool for such arguments. Given the difficulties in observing

the $J = 1 \rightarrow 0$ line, they also represent a measurement that is critical to understanding how to translate observations of high- J transitions into CO $J = 1 \rightarrow 0$. Studies of local LIRGs and ULIRGs show $r_{31} \gtrsim 0.5$ globally in these sources, and $r_{31} \sim 1$ when focusing on the active regions. Similar ratios are observed in very massive galaxies at high redshifts (SMGs), where $r_{31} \sim 0.5\text{--}0.7$ for integrated fluxes and $r_{31} \sim 1$ is observed in the very compact starbursts surrounding QSOs. CO $J = 1 \rightarrow 0$ data for main-sequence star-forming galaxies at high z remain scarce, making it difficult to ascertain whether they possess large low-excitation reservoirs of molecular gas. As the data quality, resolution, and availability improves, we expect that the simple single-component models used today will evolve into more realistic multicomponent models for the molecular ISM of these sources.

A number of researchers have explored the value of X_{CO} applicable to samples of high-redshift galaxies. The consensus, validated to first order by numerical modeling (e.g., Narayanan et al. 2011), is that massive merger-driven starbursts such as SMGs are most consistent with a low X_{CO} similar to local ULIRGs, whereas blue-sequence galaxy disks most likely have higher X_{CO} values, similar to local disks. This is reasonable in terms of the physics that drive the value of X_{CO} . High-density environments with an extended warm molecular phase not contained in self-gravitating clouds will result in a low X_{CO} , whereas molecular gas contained in collections of self-gravitating GMCs will have an X_{CO} close to the Galactic disk value. We expect the most heavily star-forming of these disks to have higher H_2 temperatures and, consequently, somewhat lower X_{CO} values. Because of the opposing effects of density and temperature in self-gravitating GMCs (for example, Equation 12), however, it appears that values as low as those observed in ULIRGs will only occur when the CO emission is dominated by an extended warm component that is not self-gravitating (e.g., Papadopoulos et al. 2012).

Multiline studies including both low- and high- J transitions allow more rigorous constraints on the density and kinetic temperature of the gas (Papadopoulos et al. 2012). In the near future, multiline studies of CO isotopologues or paired observations of CO and optically thin submillimeter dust emission will offer additional, more direct constraints on X_{CO} , though with their caveats and shortcomings.

An exciting development at high redshift is the emergence of main-sequence normal galaxy surveys that are beginning to sample the lower metallicity regime prevalent at early times. In these samples we see X_{CO} effects that are consistent with those already discussed for local galaxies (see Section 6): metal-poor galaxies are underluminous in CO for their star-formation activity (Genzel et al. 2012). This situation will be increasingly common, and more extreme, as CO surveys sample lower galaxy masses and earlier times: By $z \sim 3\text{--}4$ galaxy metallicities drop by 0.5–0.7 dex for a fixed stellar mass, and the characteristic galaxy mass also becomes lower (Mannucci et al. 2009). Ultimately the best probe of the molecular gas content of these low-metallicity young galaxies may be the fine structure line of [CII] or perhaps the dust continuum.

9. CONCLUSIONS AND OPEN PROBLEMS

9.1. Summary

We have summarized the efforts to measure X_{CO} in the Milky Way and other galaxies, as well as the theoretical arguments and studies that show that CO can be used as a tracer of molecular mass, under certain conditions, through the adoption of a CO-to- H_2 conversion factor.

In the following paragraphs, we offer concise answers to a few key questions that have been developed elsewhere in this review:

- What is the “best” value for the Milky Way X_{CO} ?
- Under what circumstances is the assumption of Galactic X_{CO} likely to be good or bad?

- How well can we calibrate X_{CO} as a function of metallicity?
- What is the most appropriate value of X_{CO} in ULIRGs?
- What can we say about X_{CO} in the distant Universe?
- Can we offer a practical prescription for X_{CO} based on observables?
- What observations and calculations are necessary to move forward?

Measurements in the Milky Way have achieved a very good level of sophistication and consistency, beyond what is possible in external galaxies. We have shown that there is a reassuring degree of uniformity among the large-scale values of X_{CO} obtained through different techniques, particularly in the inner disk ($1 \text{ kpc} \lesssim R \lesssim 9 \text{ kpc}$). We recommend adoption of a constant $X_{\text{CO}} = 2 \times 10^{20} \text{ cm}^{-2} (\text{K km s}^{-1})^{-1}$ [$\alpha_{\text{CO}} = 4.3 M_{\odot} (\text{K km s}^{-1} \text{ pc}^2)^{-1}$] with an uncertainty of ± 0.1 dex (a factor of 1.3) for the inner disk of the Milky Way. The evidence for a large-scale Galactic X_{CO} gradient and its magnitude is, presently, at best unclear, and the simplicity of a constant conversion factor is preferable. Nonetheless, there is convincing evidence that X_{CO} in the Milky Way center region is smaller than in the disk by factors of three to ten, and this is reaffirmed by extragalactic observations that find that a low X_{CO} is not uncommon in other galaxy centers. Following the results obtained by a number of studies, we recommend using $X_{\text{CO}} \approx 0.5 \times 10^{20} \text{ cm}^{-2} (\text{K km s}^{-1})^{-1}$ for $R \lesssim 500 \text{ pc}$ in the Milky Way. The uncertainty is difficult to quantify, but taking the different measurements obtained as well as the results discussed for galaxy centers and starbursts, we recommend ± 0.3 dex (a factor of two). We expect that further CO multitransition modeling, γ -ray, and dust continuum studies will help to better constrain this value as well as that of a possible large-scale Galactic gradient. For the outer Milky Way we expect X_{CO} to increase, in principle, following the same physics underlying its increase in low-metallicity environments, as we discuss below.

It is important to recognize that these are average numbers, strictly valid for GMCs on scales of tens of parsecs. The validity of invoking anything like a constant X_{CO} on a line-of-sight by line-of-sight basis is considerably less defined. Both theoretically and observationally, we have shown that considerable variation can exist on small scales, reflecting local chemistry and physical conditions.

The most mature techniques for normal galaxies remain virial mass measurements and the use of dust as an optically thin tracer. Both techniques have their drawbacks, and we particularly emphasize the ambiguous (at best) sensitivity of virial mass measurements to any extended envelope of H_2 mixed primarily with C^+ rather than CO. At solar metallicities, a wide range of measurements yield $X_{\text{CO},20} \approx 1\text{--}4$, but with large (still greater than about a factor of two) scatter and uncertainties related to the dynamical state of clouds and the environmental dependence of dust properties. In the absence of further characterization or studies, we recommend the conservative approach of adopting $X_{\text{CO}} = 2 \times 10^{20} \text{ cm}^{-2} (\text{K km s}^{-1})^{-1}$ with an uncertainty of ± 0.3 dex (a factor of two) in the disks of normal, solar metallicity galaxies. This applies to galaxies where the CO emission is dominated by self-gravitating H_2 clouds or cloud complexes. This value can approximately be applied down to metallicities of $\sim 0.5 Z_{\odot}$ and in regions where the total gas plus stars surface density is $\lesssim 300 M_{\odot} \text{ pc}^{-2}$. ALMA will greatly expand the application of both dust and virial mass techniques. Other future prospects include modeling of resolved $[\text{CII}]$ emission, now widely available thanks to *Herschel*; the extension of spectral line modeling beyond bright galaxy centers; and further exploitation of galaxy scaling relations.

Several regimes exhibit clear departures from a Galactic X_{CO} . Some, but not all, galaxy centers share a value of X_{CO} lower than disks, qualitatively similar to that observed in overwhelmingly molecular massive starburst galaxies such as ULIRGs. Dust and spectral line modeling of these central regions show depressed X_{CO} values compared to those of galaxy disks, with the depression spanning a wide range of X_{CO} up to an order of magnitude below Galactic. These central X_{CO} depressions are not universal, although they seem correlated with the stellar surface density Σ_*

(Sandstrom et al. 2013), and additional information appears necessary to predict the appropriate X_{CO} for use in any specific galaxy center.

A wide variety of evidence points to high X_{CO} in low-metallicity regions: the absolute and normalized faintness of CO, high [CII]-to-CO ratios, high SFR-to-CO ratios, large dust-based X_{CO} determinations, and theoretical calculations of cloud structure. Virial masses represent a significant exception to this body of evidence. When derived at high spatial resolution, these tend to show little or no enhancement in X_{CO} above the Galactic value, even in low-metallicity systems. We review the theoretical expectations for the shrinking of the opaque CO-emitting surface relative to H_2 as metallicity decreases. We favor a self-consistent use of dust, an optically thin tracer of gas, as the currently most mature methodology to robustly estimate molecular mass at low metallicity. We also highlight the problems with the blind use of a dust-to-gas to metallicity calibration. The present self-consistent dust-based X_{CO} estimates offer support for the picture of rapidly increasing X_{CO} at low metallicity, but still yield a wide range of X_{CO} even for similar techniques applied to the same galaxy. We recommend adopting a shielding-based prescription such as that presented by Wolfire, Hollenbach & McKee (2010) or Glover & Mac Low (2011) to account for the effects of metallicity, with the normalization chosen to match a Galactic X_{CO} at solar metallicity.

The uncertainties involved in any metallicity-dependent correction remain substantial. As a first-order picture, we expect X_{CO} will change slowly for metallicities larger than $12 + \log[\text{O}/\text{H}] \sim 8.4$ (approximately $Z_{\odot}/2$) and considerably more quickly for metallicities that are smaller. By the time X_{CO} reaches ten times the Galactic value, the CO-emitting surface encompasses only $\sim 5\%$ – 10% of the H_2 cloud, suggesting that the utility of CO as a global tracer of H_2 will become more and more marginal as one moves to progressively metal-poorer environments. Rather, CO will in fact be a tracer of high column density peaks and well-shielded regions.

There is general agreement that the processes operating in overwhelmingly molecular and turbulent starbursts, where high gas temperatures are also present, drive X_{CO} to values that can be substantially lower than in solar metallicity galactic disks. Because of the role of velocity dispersion in setting X_{CO} , in the absence of a self-regulating mechanism it is almost certain that there exists a continuum of values rather than a unique X_{CO} value that is applicable in all cases. The typical result of the one-component modeling is $X_{\text{CO}} \sim 0.4 \times 10^{20} \text{ cm}^{-2} (\text{K km s}^{-1})^{-1}$ for massive, turbulent, ultraluminous starbursts. The range around this value is large, at least ± 0.5 dex, with most of it likely representing real physical variation among sources.

The picture of X_{CO} at high redshift is still emerging, and instruments like ALMA will make a crucial contribution to better understanding it. Lacking direct measurements, the best approach is to use knowledge of the physical drivers of X_{CO} developed in local galaxies as well as scaling and consistency arguments. The simplest approach is to identify the brightest, off-main-sequence massive SMGs likely due to starbursting mergers with local ULIRGs, whereas disk, rotation-dominated main-sequence galaxies are to first order more likely similar to local disks dominated by self-gravitating or virialized molecular clouds. This is an area of active research. The picture will become more nuanced as new observations revealing the resolved kinematics of the molecular gas and its excitation are obtained. In particular, observations of main-sequence galaxies at $z \sim 1$ – 2 suggests that metallicity effects will become an increasingly important consideration at high z , as observations push to lower galaxy masses at higher redshifts and consequently more metal-poor environments (Genzel et al. 2012).

9.2. Toward a Single Prescription

Ultimately, we desire a prediction for X_{CO} based on observable properties, for objects ranging from low-metallicity dwarf galaxies to high surface density ULIRGs. In the following paragraphs

we present some steps in that direction, referring to α_{CO} because that is the quantity most often useful for distant galaxies.

Based on the discussions in Sections 6.1 and 7, α_{CO} can be thought of as having two primary dependencies: one related to the temperature and velocity dispersion effects driving a low value in ULIRGs, the other related to the dominance of CO-faint molecular gas driving a high value at low metallicities. Treating the two effects as separable, $\alpha_{\text{CO}} = \alpha_{\text{CO,MW}} f_{\text{COF}} f_{\text{SB}}$, where $\alpha_{\text{CO,MW}}$ represents an overall normalization under Milky Way disk conditions. The factor f_{COF} corresponds to a correction that accounts for the fraction of H_2 mass associated with the outer layers of clouds, where most CO is photodissociated. The factor f_{SB} accounts for changes in α_{CO} due to temperature and velocity dispersion.

Drawing from Section 6.1, f_{COF} may be approximated by applying Equation 27 to a population of identical, fixed surface density clouds,

$$f_{\text{COF}} \approx 0.67 \exp\left(\frac{+0.4}{Z' \Sigma_{\text{GMC}}^{100}}\right). \quad (30)$$

Here, we assume that the dust-to-gas ratio tracks metallicity, Z' is the metallicity normalized to the solar value, and $\Sigma_{\text{GMC}}^{100}$ is the characteristic surface density of molecular clouds in units of $100 \text{ M}_{\odot} \text{ pc}^{-2}$.

The factor f_{SB} is considerably more tentative. The simple theoretical arguments we outline in Section 2, as well as simulations (e.g., Shetty et al. 2011a), suggest that both the gas velocity dispersion and temperature are key parameters. Nonetheless, keep in mind that the fundamental driver of X_{CO} is the fraction of the CO luminosity arising from gas in self-gravitating clouds versus an extended not-self-gravitating component bound by the total mass of the system. Given current observational constraints and our desire to parameterize in terms of measurable quantities, we suggest that the variations between normal disks, galaxy centers, and ULIRGs are mostly captured by a surface density–dependent factor of the form $f_{\text{SB}} \propto \Sigma_{\text{total}}^{-\gamma}$, where Σ_{total} refers to the combined gas plus stellar surface density on kiloparsec scales.

Present constraints remain scarce, but we make an effort to present them in **Figure 12**. The data correspond to the kiloparsec-scale dust-based measurements in nearby disks by Sandstrom et al. (2013), as well as the overlap between the ULIRG samples by Downes & Solomon (1998, from which we take dynamical masses and α_{CO}) and Papadopoulos et al. (2012, from which we take α_{CO} estimates). In this latter case, α_{CO} is derived from one-component (similar to the results by Downes & Solomon) or two-component multitransition fits (which include contributions from a dense phase). The dynamical surface density is dominated by the stellar component, even in ULIRGs (Downes & Solomon 1998). Informed by the theoretical arguments leading to Equation 16, and by the results of detailed modeling (Shetty et al. 2011a), we plot $\alpha_{\text{CO}} \propto \Sigma_{\text{total}}^{-0.5}$ normalizing to our recommended Galactic α_{CO} value at $\Sigma_{\text{total}} = 100 \text{ M}_{\odot} \text{ pc}^{-2}$. Obviously this correction should not extend to surface densities below those of resolved self-gravitating GMCs.

Given the large uncertainties and the small dynamic range of the α_{CO} measurements, this simple prescription seems to reproduce the trends present in the data reasonably well, particularly for the results of one-component models for the ULIRGs (which we consider most mature). The observations may be fit with a smaller γ although with considerable uncertainty (e.g., Sandstrom et al. 2013), which leads us to prefer the theoretically motivated $\gamma \approx 0.5$. Density increases in the self-gravitating molecular material with respect to Milky Way average GMC properties will drive the α_{CO} points up, whereas increases in temperature will drive them down. The sample spans a factor of \sim two in T_{dust} , which should be a reasonable proxy for gas temperature in the ULIRGs. Although we have searched for the signature of temperature effects in the data, we see no discernible correlation with T_{dust} (e.g., Magnelli et al. 2012). The sample likely lacks the

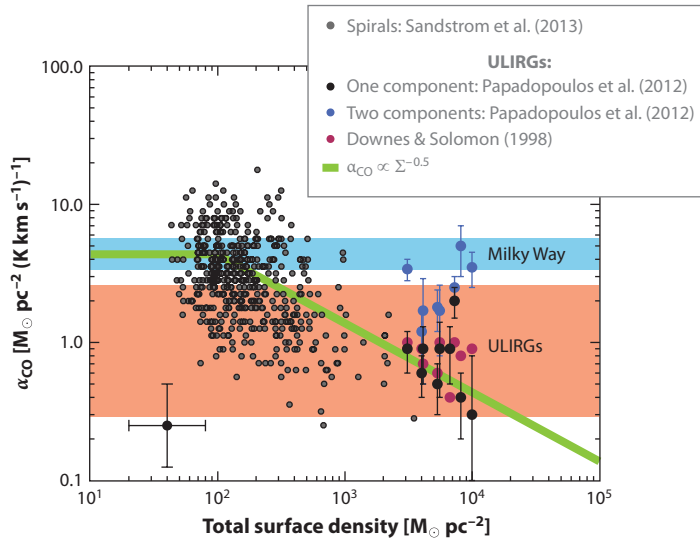


Figure 12

Conversion factor as a function of total surface density for nearby disk galaxies and ultraluminous IR galaxies (ULIRGs). The gray points illustrate the high signal-to-noise solutions for α_{CO} based on dust emission on kiloparsec scales in a sample of nearby disks, with typical errors illustrated in the lower left corner (Sandstrom et al. 2013). The corresponding surface densities are dominated by the stellar component. For the ULIRGs, we plot the α_{CO} determinations by Downes & Solomon (1998, *magenta*) and Papadopoulos et al. (2012; multitransition one-component fits are in *black*, two-component fits are in *blue*, and error bars represent possible range). The abscissa is from the dynamical mass measurements by Downes & Solomon (1998), thus we plot only the overlap of both samples. The color bands illustrate the recommended ranges for Milky Way and ULIRG conversion factors. The $\Sigma^{-0.5}$ line for $\Sigma > 100 \text{ M}_{\odot} \text{ pc}^{-2}$ is a reasonable representation of the overall trends when considering the one-component fits.

necessary dynamic range to pull those effects out of the data. Possibly, as previously discussed, the lack of a temperature correlation could be in part due to cancelations between the opposite effects the density of self-gravitating clouds and their temperature have on X_{CO} . Thus, as a tentative first step for a simple conversion factor prescription, we suggest using

$$\alpha_{\text{CO}} \approx 2.9 \exp\left(\frac{+0.4}{Z' \Sigma_{\text{GMC}}^{100}}\right) \left(\frac{\Sigma_{\text{total}}}{100 \text{ M}_{\odot} \text{ pc}^{-2}}\right)^{-\gamma} \text{ M}_{\odot} (\text{K km s}^{-1} \text{ pc}^2)^{-1}, \quad (31)$$

with $\gamma \approx 0.5$ for $\Sigma_{\text{total}} > 100 \text{ M}_{\odot} \text{ pc}^{-2}$ and $\gamma = 0$ otherwise. Note that we still expect a fair dispersion around this average prescription, representing the variation in local parameters such as temperature and Σ_{GMC} .

There has been an exciting range of theoretical and numerical developments on calculations of X_{CO} in the past few years. The coupling of high-resolution hydrodynamical simulations including chemistry and radiative transfer, with increasingly sophisticated theoretical modeling of PDRs and molecular clouds, and galaxy scale simulations offers an exciting avenue of progress. Numerically derived calibrations, such as those obtained on small scales by Glover & Mac Low (2011) or Shetty et al. (2011a) and on large scales by Narayanan et al. (2012), show much promise. Such simulations are likely to become increasingly reliable as the modeling is able to better incorporate and couple the physics, kinematics, and radiative transfer on the small and large scales. Grounded on observations, simulations may offer the ultimate way to calibrate the CO-to- H_2 conversion factor in a variety of environments.

DISCLOSURE STATEMENT

The authors are not aware of any affiliations, memberships, funding, or financial holdings that might be perceived as affecting the objectivity of this review.

ACKNOWLEDGMENTS

We especially thank the following people for providing extensive comments on earlier versions of this manuscript: Leo Blitz, Neal Evans, Reinhard Genzel, Erik Rosolowsky, Nick Scoville, and Ewine van Dishoeck. We also thank the following people for providing figures, comments, advice, and/or for enduring one of the partial or complete drafts of this manuscript: Jean-Philippe Bernard, Chris Carilli, Thomas Dame, Jennifer Donovan Meyer, Isabelle Grenier, Andrew Harris, Remy Indebetouw, Frank Israel, Guðlaugur Jóhannesson, Douglas Marshall, Desika Narayanan, Eve Ostriker, Padelis Papadopoulos, Jorge Pineda, Karin Sandstrom, Rahul Shetty, Andrew Strong, Linda Tacconi, Stuart Vogel, Fabian Walter, and Zhi-Yu Zhang. A.D.B. wishes to acknowledge partial support from a CAREER grant NSF-AST0955836, from NSF-AST1139998, and from a Research Corporation for Science Advancement Cottrell Scholar award, as well as full support from his wife, Liliana.

LITERATURE CITED

- Abdo AA, Ackermann M, Ajello M, Atwood WB, Baldini L, et al. 2010a. *Astron. Astrophys.* 512:7
- Abdo AA, Ackermann M, Ajello M, Baldini L, Ballet J, et al. 2010b. *Astron. Astrophys.* 523:46
- Abdo AA, Ackermann M, Ajello M, Baldini L, Ballet J, et al. 2010c. *Ap. J.* 710:133–49
- Ackermann M, Ajello M, Allafort A, Antolini E, Baldini L, et al. 2012a. *Ap. J.* 756:4
- Ackermann M, Ajello M, Allafort A, Baldini L, Ballet J, et al. 2012b. *Ap. J.* 755:22
- Ackermann M, Ajello M, Allafort A, Baldini L, Ballet J, et al. 2012c. *Astron. Astrophys.* 538:71
- Ackermann M, Ajello M, Atwood WB, Baldini L, Ballet J, et al. 2012d. *Ap. J.* 750:3
- Ackermann M, Ajello M, Baldini L, Ballet J, Barbiellini G, et al. 2011. *Ap. J.* 726:81
- Adler DS, Lo KY, Wright MCH, Rydbeck G, Plante RL, Allen RJ. 1992. *Ap. J.* 392:497–508
- Aravena M, Carilli C, Daddi E, Wagg J, Walter F, et al. 2010. *Ap. J.* 718:177–83
- Arimoto N, Sofue Y, Tsujimoto T. 1996. *Publ. Astron. Soc. Jpn.* 48:275–84
- Asplund M, Grevesse N, Sauval AJ, Scott P. 2009. *Annu. Rev. Astron. Astrophys.* 47:481–522
- Ballesteros-Paredes J. 2006. *MNRAS* 372:443–49
- Ballesteros-Paredes J, Hartmann LW, Vázquez-Semadeni E, Heitsch F, Zamora-Avilés MA. 2011. *MNRAS* 411:65–70
- Bell TA, Roueff E, Viti S, Williams DA. 2006. *MNRAS* 371:1865–72
- Bell TA, Viti S, Williams DA. 2007. *MNRAS* 378:983–94
- Bennett CL, Fixsen DJ, Hinshaw G, Mather JC, Moseley SH, et al. 1994. *Ap. J.* 434:587–98
- Bertoldi F, McKee CF. 1992. *Ap. J.* 395:140–57
- Blanc GA, Schrubba A, Evans NJ II, Jogee S, Bolatto AD, et al. 2013. *Ap. J.* 764:117
- Blitz L, Bloemen JBGM, Hermsen W, Bania TM. 1985. *Astron. Astrophys.* 143:267–73
- Blitz L, Fukui Y, Kawamura A, Leroy A, Mizuno N, Rosolowsky E. 2007. *Protostars Planets V*:81–96
- Blitz L, Shu FH. 1980. *Ap. J.* 238:148–57
- Bloemen H. 1989. *Annu. Rev. Astron. Astrophys.* 27:469–516
- Bohlin RC, Savage BD, Drake JF. 1978. *Ap. J.* 224:132–42
- Bolatto AD, Jackson JM, Ingalls JG. 1999. *Ap. J.* 513:275–86
- Bolatto AD, Leroy A, Israel FP, Jackson JM. 2003. *Ap. J.* 595:167–78
- Bolatto AD, Leroy AK, Jameson K, Ostriker E, Gordon K, et al. 2011. *Ap. J.* 741:12
- Bolatto AD, Leroy AK, Rosolowsky E, Walter F, Blitz L. 2008. *Ap. J.* 686:948–65
- Boselli A, Lequeux J, Gavazzi G. 2002. *Astron. Astrophys.* 384:33–47

- Bot C, Boulanger F, Lagache G, Cambr  sy L, Egret D. 2004. *Astron. Astrophys.* 423:567–77
- Bot C, Boulanger F, Rubio M, Rantakyro F. 2007. *Astron. Astrophys.* 471:103–12
- Bot C, Rubio M, Boulanger F, Albrecht M, Leroy A, et al. 2010. *Astron. Astrophys.* 524:52
- Bothwell MS, Chapman SC, Tacconi L, Smail I, Ivison RJ, et al. 2010. *MNRAS* 405:219–33
- Bothwell MS, Smail I, Chapman SC, Genzel R, Ivison RJ, et al. 2013. *MNRAS* 428:3047–67
- Boulanger F, Abergel A, Bernard JP, Burton WB, Desert FX, et al. 1996. *Astron. Astrophys.* 312:256–62
- Bradford CM, Nikola T, Stacey GJ, Bolatto AD, Jackson JM, et al. 2003. *Ap. J.* 586:891–901
- Brand J, Wouterloot JGA. 1995. *Astron. Astrophys.* 303:851–71
- Braun R, Thilker DA, Walterbos RAM, Corbelli E. 2009. *Ap. J.* 695:937–53
- Brown RL, Vanden Bout PA. 1991. *Astron. J.* 102:1956–59
- Bryant PM, Scoville NZ. 1996. *Ap. J.* 457:678
- Bryant PM, Scoville NZ. 1999. *Astron. J.* 117:2632–55
- Burton WB, Gordon MA, Bania TM, Lockman FJ. 1975. *Ap. J.* 202:30–49
- Cambr  sy L, Jarrett TH, Beichman CA. 2005. *Astron. Astrophys.* 435:131–39
- Carilli CL, Daddi E, Riechers D, Walter F, Weiss A, et al. 2010. *Ap. J.* 714:1407–17
- Carilli CL, Walter F. 2013. *Annu. Rev. Astron. Astrophys.* 51:105–61
- Chapman NL, Mundy LG, Lai SP, Evans NJ II. 2009. *Ap. J.* 690:496–511
- Cormier D, Madden SC, Hony S, Contursi A, Poglitsch A, et al. 2010. *Astron. Astrophys.* 518:L57
- Crawford MK, Genzel R, Townes CH, Watson DM. 1985. *Ap. J.* 291:755–71
- Dabrowski I. 1984. *Can. J. Phys.* 62:1639–64
- Daddi E, Bournaud F, Walter F, Dannerbauer H, Carilli CL, et al. 2010a. *Ap. J.* 713:686–707
- Daddi E, Elbaz D, Walter F, Bournaud F, Salmi F, et al. 2010b. *Ap. J. Lett.* 714:L118–22
- Dame TM, Hartmann D, Thaddeus P. 2001. *Ap. J.* 547:792–813
- Dame TM, Ungerechts H, Cohen RS, de Geus EJ, Grenier IA, et al. 1987. *Ap. J.* 322:706–20
- Dannerbauer H, Daddi E, Riechers DA, Walter F, Carilli CL, et al. 2009. *Ap. J. Lett.* 698:L178–82
- de Jong T, Boland W, Dalgarno A. 1980. *Astron. Astrophys.* 91:68–84
- Dickman RL. 1978. *Ap. J. Suppl.* 37:407–27
- Dickman RL, Snell RL, Schloerb FP. 1986. *Ap. J.* 309:326–30
- Dobashi K, Bernard JP, Hughes A, Paradis D, Reach WT, Kawamura A. 2008. *Astron. Astrophys.* 484:205–23
- Dobashi K, Bernard JP, Kawamura A, Egusa F, Hughes A, et al. 2009. *Astron. J.* 137:5099–109
- Donovan Meyer J, Koda J, Momose R, Fukuhara M, Mooney T, et al. 2012. *Ap. J.* 744:42
- Donovan Meyer J, Koda J, Momose R, Mooney T, Egusa F, et al. 2013. *Ap. J.* In press (arXiv:1305.5275)
- Downes D, Solomon PM. 1998. *Ap. J.* 507:615–54
- Downes D, Solomon PM, Radford SJE. 1993. *Ap. J.* 414:L13–16
- Draine BT. 1978. *Ap. J. Suppl.* 36:595–619
- Draine BT. 2009. In *Cosmic Dust—Near and Far*, ed. Th Henning, E Gr  n, J Steinacker. *ASP Conf. Ser.* 414:453. San Francisco: ASP
- Draine BT, Dale DA, Bendo G, Gordon KD, Smith JDT, et al. 2007. *Ap. J.* 663:866–94
- Draine BT, Li A. 2001. *Ap. J.* 551:807–24
- Draine BT, Li A. 2007. *Ap. J.* 657:810–37
- Dufour RJ, Shields GA, Talbot RJJ. 1982. *Ap. J.* 252:461–73
- Dwek E. 1998. *Ap. J.* 501:643
- Dwek E, Cherchneff I. 2011. *Ap. J.* 727:63
- Elmegreen BG. 2000. *Ap. J.* 530:277–81
- Elmegreen BG, Morris M, Elmegreen DM. 1980. *Ap. J.* 240:455–63
- Evans NJ II, Dunham MM, J  rgensen JK, Enoch ML, Mern B, et al. 2009. *Ap. J. Suppl.* 181:321–50
- Falgarone E, Lis DC, Phillips TG, Pouquet A, Porter DH, Woodward PR. 1994. *Ap. J.* 436:728–40
- Federman SR, Rawlings JMC, Taylor SD, Williams DA. 1996. *MNRAS* 279:L41–46
- Feldmann R, Gnedin NY, Kravtsov AV. 2012. *Ap. J.* 747:124
- Fixsen DJ, Bennett CL, Mather JC. 1999. *Ap. J.* 526:207–14
- Flagey N, Noriega-Crespo A, Boulanger F, Carey SJ, Brooke TY, et al. 2009. *Ap. J.* 701:1450–63
- Frerking MA, Langer WD, Wilson RW. 1982. *Ap. J.* 262:590–605
- Fukui Y, Kawamura A. 2010. *Annu. Rev. Astron. Astrophys.* 48:547–80

- Fukui Y, Kawamura A, Minamidani T, Mizuno Y, Kanai Y, et al. 2008. *Ap. J. Suppl.* 178:56–70
- Gabici S, Aharonian FA, Blasi P. 2007. *Ap. Space Sci.* 309:365–71
- Galliano F, Hony S, Bernard JP, Bot C, Madden SC, et al. 2011. *Astron. Astrophys.* 536:88
- Gao Y, Solomon PM. 2004. *Ap. J.* 606:271–90
- Garcia-Burillo S, Combes F, Gerin M. 1993. *Astron. Astrophys.* 274:148
- Genzel R, Newman S, Jones T, Förster Schreiber NM, Shapiro K, et al. 2011. *Ap. J.* 733:101
- Genzel R, Tacconi LJ, Combes F, Bolatto A, Neri R, et al. 2012. *Ap. J.* 746:69
- Genzel R, Tacconi LJ, Gracia-Carpio J, Sternberg A, Cooper MC, et al. 2010. *MNRAS* 407:2091–108
- Glover SCO, Federrath C, Mac Low MM, Klessen RS. 2010. *MNRAS* 404:2–29
- Glover SCO, Mac Low MM. 2007a. *Ap. J. Suppl.* 169:239–68
- Glover SCO, Mac Low MM. 2007b. *Ap. J.* 659:1317–37
- Glover SCO, Mac Low MM. 2011. *MNRAS* 412:337–50
- Godard B, Falgarone E, Pineau des Forets G. 2009. *Astron. Astrophys.* 495:847–67
- Goldreich P, Kwan J. 1974. *Ap. J.* 189:441–54
- Goldsmith PF, Heyer M, Narayanan G, Snell R, Li D, Brunt C. 2008. *Ap. J.* 680:428–45
- Gratier P, Braine J, Rodriguez-Fernandez NJ, Israel FP, Schuster KF, et al. 2010. *Astron. Astrophys.* 512:68
- Grenier IA, Casandjian JM, Terrier R. 2005. *Science* 307:1292–95
- Guelin M, Zylka R, Mezger PG, Haslam CGT, Kreysa E, et al. 1993. *Astron. Astrophys.* 279:L37–40
- Guelin M, Zylka R, Mezger PG, Haslam CGT, Kreysa E. 1995. *Astron. Astrophys.* 298:L29
- Habart E, Dartois E, Abergel A, Baluteau JP, Naylor D, et al. 2010. *Astron. Astrophys.* 518:L116
- Harris AI, Baker AJ, Zonak SG, Sharon CE, Genzel R, et al. 2010. *Ap. J.* 723:1139–49
- Heiderman A, Evans NJ II, Allen LE, Huard T, Heyer M. 2010. *Ap. J.* 723:1019–37
- Heiles C. 1994. *Ap. J.* 436:720–27
- Heiles C, Troland TH. 2003. *Ap. J.* 586:1067–93
- Heyer M, Krawczyk C, Duval J, Jackson JM. 2009. *Ap. J.* 699:1092–103
- Heyer MH, Carpenter JM, Snell RL. 2001. *Ap. J.* 551:852–66
- Hollenbach D, Kaufman MJ, Neufeld D, Wolfire M, Goicoechea JR. 2012. *Ap. J.* 754:105
- Hollenbach DJ, Tielens AGGM. 1997. *Annu. Rev. Astron. Astrophys.* 35:179–216
- Hollenbach DJ, Tielens AGGM. 1999. *Rev. Mod. Phys.* 71:173–230
- Hughes A, Wong T, Ott J, Muller E, Pineda JL, et al. 2010. *MNRAS* 406:2065–86
- Hunter DA, Kaufman M, Hollenbach DJ, Rubin RH, Malhotra S, et al. 2001. *Ap. J.* 553:121–45
- Hunter SD, Bertsch DL, Catelli JR, Dame TM, Digel SW, et al. 1997. *Ap. J.* 481:205
- Ingalls JG, Bania TM, Boulanger F, Draine BT, Falgarone E, Hily-Blant P. 2011. *Ap. J.* 743:174
- Iono D, Wilson CD, Takakuwa S, Yun MS, Petitpas GR, et al. 2007. *Ap. J.* 659:283–95
- Iono D, Wilson CD, Yun MS, Baker AJ, Petitpas GR, et al. 2009. *Ap. J.* 695:1537–49
- Israel FP. 1997a. *Astron. Astrophys.* 328:471–82
- Israel FP. 1997b. *Astron. Astrophys.* 317:65–72
- Israel FP. 2009a. *Astron. Astrophys.* 506:689–702
- Israel FP. 2009b. *Astron. Astrophys.* 493:525–38
- Israel FP, Baas F. 2001. *Astron. Astrophys.* 371:433–44
- Israel FP, de Graauw T, van de Stadt H, de Vries CP. 1986. *Ap. J.* 303:186–97
- Israel FP, Johansson LEB, Rubio M, Garay G, de Graauw T, et al. 2003. *Astron. Astrophys.* 406:817–28
- Israel FP, Maloney PR. 2011. *Astron. Astrophys.* 531:19
- Israel FP, Maloney PR, Geis N, Herrmann F, Madden SC, et al. 1996. *Ap. J.* 465:738
- Israel FP, Tilanus RPJ, Baas F. 2006. *Astron. Astrophys.* 445:907–13
- Ivison RJ, Papadopoulos PP, Smail I, Greve TR, Thomson AP, et al. 2011. *MNRAS* 412:1913–25
- Jackson JM, Paglione TAD, Carlstrom JE, Rieu NQ. 1995. *Ap. J.* 438:695–701
- Kainulainen J, Beuther H, Henning T, Plume R. 2009. *Astron. Astrophys.* 508:L35–38
- Kennicutt RC Jr, Evans NJ II. 2012. *Annu. Rev. Astron. Astrophys.* 50:531–608
- Kutner ML, Leung CM. 1985. *Ap. J.* 291:188–201
- Kutner ML, Ulich BL. 1981. *Ap. J.* 250:341–48
- Lada CJ, Lombardi M, Alves JF. 2010. *Ap. J.* 724:687–93
- Lada EA, Blitz L. 1988. *Ap. J.* 326:L69–73

- Langer WD, Velusamy T, Pineda JL, Goldsmith PF, Li D, Yorke HW. 2010. *Astron. Astrophys.* 521:L17
- Larson RB. 1981. *MNRAS* 194:809–26
- Lebrun F, Bennett K, Bignami GF, Caraveo PA, Bloemen JBG, et al. 1983. *Ap. J.* 274:231–36
- Lequeux J, Le Bourlot J, Pineau des Forets G, Roueff E, Boulanger F, Rubio M. 1994. *Astron. Astrophys.* 292:371–80
- Lequeux J, Peimbert M, Rayo JF, Serrano A, Torres-Peimbert S. 1979. *Astron. Astrophys.* 80:155–66
- Leroy A, Bolatto A, Stanimirovic S, Mizuno N, Israel F, Bot C. 2007. *Ap. J.* 658:1027–46
- Leroy A, Bolatto A, Walter F, Blitz L. 2006. *Ap. J.* 643:825–43
- Leroy AK, Bolatto A, Bot C, Engelbracht CW, Gordon K, et al. 2009. *Ap. J.* 702:352–67
- Leroy AK, Bolatto A, Gordon K, Sandstrom K, Gratier P, et al. 2011. *Ap. J.* 737:12
- Leroy AK, Walter F, Brinks E, Bigiel F, de Blok WJG, et al. 2008. *Astron. J.* 136:2782–845
- Levrier F, Le Petit F, Hennebelle P, Lesaffre P, Gerin M, Falgarone E. 2012. *Astron. Astrophys.* 544:22
- Liszt HS. 2011. *Astron. Astrophys.* 527:45
- Liszt HS, Pety J. 2012. *Astron. Astrophys.* 541:58
- Liszt HS, Pety J, Lucas R. 2010. *Astron. Astrophys.* 518:45
- Lombardi M, Alves J. 2001. *Astron. Astrophys.* 377:1023–34
- Lombardi M, Alves J, Lada CJ. 2006. *Astron. Astrophys.* 454:781–96
- MacLaren I, Richardson KM, Wolfendale AW. 1988. *Ap. J.* 333:821–25
- Madden SC, Geis N, Genzel R, Herrmann F, Jackson J, et al. 1993. *Ap. J.* 407:579–87
- Madden SC, Poglitsch A, Geis N, Stacey GJ, Townes CH. 1997. *Ap. J.* 483:200
- Magdis GE, Daddi E, Elbaz D, Sargent M, Dickinson M, et al. 2011. *Ap. J. Lett.* 740:L15
- Magnani L, Chastain RJ, Kim HC, Hartmann D, Truong AT, Thaddeus P. 2003. *Ap. J.* 586:1111–19
- Magnelli B, Saintonge A, Lutz D, Tacconi LJ, Berta S, et al. 2012. *Astron. Astrophys.* 548:A22
- Maloney P. 1990. *Ap. J.* 348:L9–12
- Maloney P, Black JH. 1988. *Ap. J.* 325:389–401
- Mannucci F, Cresci G, Maiolino R, Marconi A, Gnerucci A. 2010. *MNRAS* 408:2115–27
- Mannucci F, Cresci G, Maiolino R, Marconi A, Pastorini G, et al. 2009. *MNRAS* 398:1915–31
- Mao RQ, Schulz A, Henkel C, Mauersberger R, Muters D, Dinh-V-Trung. 2010. *Ap. J.* 724:1336–56
- Mauersberger R, Henkel C, Walsh W, Schulz A. 1999. *Astron. Astrophys.* 341:256–63
- McKee CF. 1999. In *The Origin of Stars and Planetary Systems*, ed. CJ Lada, ND Kylafis, pp. 29–66. Dordrecht, Netherlands: Kluwer Acad. Publ.
- McKee CF, Ostriker EC. 2007. *Annu. Rev. Astron. Astrophys.* 45:565–687
- McKee CF, Zweibel EG. 1992. *Ap. J.* 399:551–62
- Meier DS, Turner JL. 2001. *Ap. J.* 551:687–701
- Meier DS, Turner JL. 2004. *Astron. J.* 127:2069–84
- Mény C, Gromov V, Boudet N, Bernard JP, Paradis D, Nayral C. 2007. *Astron. Astrophys.* 468:171–88
- Mirabel IF, Sanders DB. 1988. *Ap. J.* 335:104–21
- Miville-Deschênes MA, Martin PG, Abergel A, Bernard JP, Boulanger F, et al. 2010. *Astron. Astrophys.* 518:L104
- Mizuno N, Rubio M, Mizuno A, Yamaguchi R, Onishi T, Fukui Y. 2001. *Publ. Astron. Soc. Jpn.* 53:L45–49
- Moustakas J, Kennicutt RCJ, Tremonti CA, Dale DA, Smith JDT, Calzetti D. 2010. *VizieR Online Data Catalog* 219:00233
- Muñoz-Mateos JC, Gil de Paz A, Boissier S, Zamorano J, Dale DA, et al. 2009. *Ap. J.* 701:1965–91
- Murphy EJ, Porter TA, Moskalenko IV, Helou G, Strong AW. 2012. *Ap. J.* 750:126
- Nakai N, Kuno N. 1995. *Publ. Astron. Soc. Jpn.* 47:761–69
- Narayanan D, Hayward CC, Cox TJ, Hernquist L, Jonsson P, et al. 2010. *MNRAS* 401:1613–19
- Narayanan D, Krumholz M, Ostriker EC, Hernquist L. 2011. *MNRAS* 418:664–79
- Narayanan D, Krumholz MR, Ostriker EC, Hernquist L. 2012. *MNRAS* 421(4):3127–46
- Obreschkow D, Rawlings S. 2009. *MNRAS* 394:1857–74
- Oka T, Hasegawa T, Hayashi M, Handa T, Sakamoto S. 1998. *Ap. J.* 493:730
- Oka T, Hasegawa T, Sato F, Tsuboi M, Miyazaki A, Sugimoto M. 2001. *Ap. J.* 562:348–62
- Padoan P, Jones BJT, Nordlund AP. 1997. *Ap. J.* 474:730
- Padovani M, Galli D, Glassgold AE. 2009. *Astron. Astrophys.* 501:619–31

- Paglione TAD, Jackson JM, Ishizuki S. 1997. *Ap. J.* 484:656
- Pak S, Jaffe DT, van Dishoeck EF, Johansson LEB, Booth RS. 1998. *Ap. J.* 498:735
- Papadopoulos PP, Seaquist ER. 1999. *Ap. J.* 516:114–26
- Papadopoulos PP, van der Werf P, Xilouris E, Isaak KG, Gao Y. 2012. *Ap. J.* 751:10
- Papadopoulos PP, van der Werf P, Xilouris EM, Isaak KG, Gao Y, Mühle S. 2012. *MNRAS* 426(4):2601–29
- Paradis D, Dobashi K, Shimoikura T, Kawamura A, Onishi T, et al. 2012. *Astron. Astrophys.* 543:A103
- Penzias AA. 1975. In *Atomic and Molecular Physics and the Interstellar Matter; Proceedings of the Twenty-Sixth Summer School of Theoretical Physics*, ed. R Balian, P Encrenaz, J Lequeux, pp. 373–408. Holmdel, NJ: Bell Teleph. Lab., Inc.
- Pilyugin LS, Thuan TX. 2005. *Ap. J.* 631:231–43
- Pineda JE, Caselli P, Goodman AA. 2008. *Ap. J.* 679:481–96
- Pineda JL, Goldsmith PF, Chapman N, Snell RL, Li D, et al. 2010a. *Ap. J.* 721:686–708
- Pineda JL, Ott J, Klein U, Wong T, Muller E, Hughes A. 2009. *Ap. J.* 703:736–51
- Pineda JL, Velusamy T, Langer WD, Goldsmith PF, Li D, Yorke HW. 2010b. *Astron. Astrophys.* 521:L19
- Planck Collaboration XIX, Ade PAR, Aghanim N, Arnaud M, Ashdown M, et al. 2011. *Astron. Astrophys.* 536:A19
- Planck Collaboration XXI, Abergel A, Ade PAR, Aghanim N, Arnaud M, et al. 2011. *Astron. Astrophys.* 536:21
- Planck Collaboration XXIV, Abergel A, Ade PAR, Aghanim N, Arnaud M, et al. 2011. *Astron. Astrophys.* 536:A24
- Planck Collaboration XXV, Abergel A, Ade PAR, Aghanim N, Arnaud M, et al. 2011. *Astron. Astrophys.* 536:25
- Poglitsch A, Krabbe A, Madden SC, Nikola T, Geis N, et al. 1995. *Ap. J.* 454:293
- Rachford BL, Snow TP, Destree JD, Ross TL, Ferlet R, et al. 2009. *Ap. J. Suppl.* 180:125–37
- Rand RJ, Kulkarni SR. 1990. *Ap. J.* 349:L43–46
- Rand RJ, Lord SD, Higdon JL. 1999. *Ap. J.* 513:720–32
- Rangwala N, Maloney PR, Glenn J, Wilson CD, Rykala A, et al. 2011. *Ap. J.* 743:94
- Rebolledo D, Wong T, Leroy A, Koda J, Donovan Meyer J. 2012. *Ap. J.* 757:155
- Rickard LJ, Palmer P, Morris M, Zuckerman B, Turner BE. 1975. *Ap. J.* 199:L75–78
- Riechers DA, Carilli CL, Maddalena RJ, Hodge J, Harris AI, et al. 2011a. *Ap. J. Lett.* 739:L32
- Riechers DA, Carilli CL, Walter F, Momjian E. 2010. *Ap. J. Lett.* 724:L153–57
- Riechers DA, Hodge J, Walter F, Carilli CL, Bertoldi F. 2011b. *Ap. J. Lett.* 739:L31
- Rieke GH, Lebofsky MJ. 1985. *Ap. J.* 288:618–21
- Röllig M, Ossenkopf V, Jeyakumar S, Stutzki J, Sternberg A. 2006. *Astron. Astrophys.* 451:917–24
- Roman-Duval J, Jackson JM, Heyer M, Rathborne J, Simon R. 2010. *Ap. J.* 723:492–507
- Rosolowsky E. 2007. *Ap. J.* 654:240–51
- Rosolowsky E, Blitz L. 2005. *Ap. J.* 623:826–45
- Rosolowsky E, Engargiola G, Plambeck R, Blitz L. 2003. *Ap. J.* 599:258–74
- Rosolowsky E, Leroy A. 2006. *Publ. Astron. Soc. Pac.* 118:590–610
- Rubio M, Boulanger F, Rantakyro F, Contursi A. 2004. *Astron. Astrophys.* 425:L1–4
- Rubio M, Lequeux J, Boulanger F. 1993. *Astron. Astrophys.* 271:9
- Sanders DB, Mirabel IF. 1996. *Annu. Rev. Astron. Astrophys.* 34:749
- Sandstrom KM, Leroy AK, Walter F, Bolatto AD, Croxall KV, et al. 2013. *Ap. J.* In press (arXiv:1212.1208)
- Savage BD, Bohlin RC, Drake JF, Budich W. 1977. *Ap. J.* 216:291–307
- Schinnerer E, Weiss A, Aalto S, Scoville NZ. 2010. *Ap. J.* 719:1588–601
- Schlegel DJ, Finkbeiner DP, Davis M. 1998. *Ap. J.* 500:525
- Schnee S, Li J, Goodman AA, Sargent AI. 2008. *Ap. J.* 684:1228–39
- Schruba A, Leroy AK, Walter F, Bigiel F, Brinks E, et al. 2012. *Astron. J.* 143:138
- Scoville NZ, Good JC. 1989. *Ap. J.* 339:149–62
- Scoville NZ, Hersch K. 1979. *Ap. J.* 229:578–82
- Scoville NZ, Sanders DB. 1987. *Ap. Space Sci. Libr.* 134:21–50
- Scoville NZ, Solomon PM. 1975. *Ap. J.* 199:L105–9
- Scoville NZ, Yun MS, Bryant PM. 1997. *Ap. J.* 484:702
- Scoville NZ, Yun MS, Sanders DB, Clemens DP, Waller WH. 1987. *Ap. J. Suppl.* 63:821–915
- Sheffer Y, Rogers M, Federman SR, Abel NP, Gredel R, et al. 2008. *Ap. J.* 687:1075–106

- Shetty R, Glover SC, Dullemond CP, Klessen RS. 2011a. *MNRAS* 412:1686–700
- Shetty R, Glover SC, Dullemond CP, Ostriker EC, Harris AI, Klessen RS. 2011b. *MNRAS* 415:3253–74
- Shibai H, Okuda H, Nakagawa T, Matsuhara H, Maihara T, et al. 1991. *Ap. J.* 374:522–32
- Sliwa K, Wilson CD, Petitpas GR, Armus L, Juvela M, et al. 2012. *Ap. J.* 753:46
- Smith MWL, Eales SA, Gomez HL, Roman-Duval J, Fritz J, et al. 2012. *Ap. J.* 756:40
- Sodroski TJ, Odegard N, Dwek E, Hauser MG, Franz BA, et al. 1995. *Ap. J.* 452:262
- Sofia UJ, Lauroesch JT, Meyer DM, Cartledge SIB. 2004. *Ap. J.* 605:272–77
- Solomon PM, de Zafra R. 1975. *Ap. J.* 199:L79–83
- Solomon PM, Downes D, Radford SJE. 1992. *Ap. J.* 398:L29–32
- Solomon PM, Downes D, Radford SJE, Barrett JW. 1997. *Ap. J.* 478:144
- Solomon PM, Rivolo AR, Barrett J, Yahil A. 1987. *Ap. J.* 319:730–41
- Solomon PM, Scoville NZ, Penzias AA, Wilson RW, Jefferts KB. 1972. *Ap. J.* 178:125–30
- Solomon PM, Vanden Bout PA. 2005. *Annu. Rev. Astron. Astrophys.* 43:677–725
- Sonnentrucker P, Welty DE, Thorburn JA, York DG. 2007. *Ap. J. Suppl.* 168:58–99
- Stacey GJ, Geis N, Genzel R, Lugten JB, Poglitsch A, et al. 1991. *Ap. J.* 373:423–44
- Stanimirovic S, Staveley-Smith L, van der Hulst JM, Bontekoe TR, Kester DJM, Jones PA. 2000. *MNRAS* 315:791–807
- Stecker FW, Solomon PM, Scoville NZ, Ryter CE. 1975. *Ap. J.* 201:90–97
- Strong AW, Mattox JR. 1996. *Astron. Astrophys.* 308:L21–24
- Strong AW, Moskalenko IV, Reimer O, Digel S, Diehl R. 2004. *Astron. Astrophys.* 422:L47–50
- Swinbank AM, Smail I, Longmore S, Harris AI, Baker AJ, et al. 2010. *Nature* 464:733–36
- Tacconi LJ, Genzel R, Neri R, Cox P, Cooper MC, et al. 2010. *Nature* 463:781–84
- Tacconi LJ, Genzel R, Smail I, Neri R, Chapman SC, et al. 2008. *Ap. J.* 680:246–62
- Tacconi LJ, Neri R, Chapman SC, Genzel R, Smail I, et al. 2006. *Ap. J.* 640:228–40
- Tacconi LJ, Young JS. 1987. *Ap. J.* 322:681–87
- Taylor CL, Hüttemeister S, Klein U, Greve A. 1999. *Astron. Astrophys.* 349:424–34
- Taylor CL, Kobulnicky HA, Skillman ED. 1998. *Astron. J.* 116:2746–56
- Thompson TA, Quataert E, Murray N. 2005. *Ap. J.* 630:167–85
- Thronson HAJ. 1988. *Galact. Extragalact. Star Form.* 2:621
- Thronson HAJ, Greenhouse M, Hunter DA, Telesco CM, Harper DA. 1988. *Ap. J.* 334:605–12
- Ueda J, Iono D, Petitpas G, Yun MS, Ho PTP, et al. 2012. *Ap. J.* 745:65
- van Dishoeck EF, Black JH. 1986. *Ap. J. Suppl.* 62:109–45
- van Dishoeck EF, Black JH. 1988. *Ap. J.* 334:771–802
- van Dishoeck EF, Jonkheid B, van Hemert MC. 2006. *Faraday Discuss. Chem. Soc.* 133:231–43
- Velusamy T, Langer WD, Pineda JL, Goldsmith PF. 2012. *Astron. Astrophys.* 541:L10
- Velusamy T, Langer WD, Pineda JL, Goldsmith PF, Li D, Yorke HW. 2010. *Astron. Astrophys.* 521:L18
- Visser R, van Dishoeck EF, Doty SD, Dullemond CP. 2009. *Astron. Astrophys.* 495:881–97
- Vogel SN, Boulanger F, Ball R. 1987. *Ap. J.* 321:L145–49
- Vogel SN, Kulkarni SR, Scoville NZ. 1988. *Nature* 334:402–6
- Walter F, Taylor CL, Hüttemeister S, Scoville N, McIntyre V. 2001. *Astron. J.* 121:727–39
- Walter F, Weiss A, Martin C, Scoville N. 2002. *Astron. J.* 123:225–37
- Ward JS, Zmuidzinas J, Harris AI, Isaak KG. 2003. *Ap. J.* 587:171–85
- Watanabe Y, Sorai K, Kuno N, Habe A. 2011. *MNRAS* 411:1409–17
- Wei LH, Keto E, Ho LC. 2012. *Ap. J.* 750:136
- Weiss A, Downes D, Walter F, Henkel C. 2001. In *From Z-Machines to ALMA: (Sub)Millimeter Spectroscopy of Galaxies*, ed. AJ Baker, J Glenn, AI Harris, JG Mangum, MS Yun. *ASP Conf. Ser.* 375:25. San Francisco: ASP
- Wild W, Harris AI, Eckart A, Genzel R, Graf UU, et al. 1992. *Astron. Astrophys.* 265:447–64
- Wilson CD. 1994. *Ap. J.* 434:L11–14
- Wilson CD. 1995. *Ap. J. Lett.* 448:L97
- Wilson CD, Scoville N. 1990. *Ap. J.* 363:435–50
- Wilson CD, Scoville N, Madden SC, Charmandaris V. 2003. *Ap. J.* 599:1049–66
- Wilson CD, Scoville N, Madore BF, Sanders DB, Freedman WL. 1988. *Ap. J.* 333:611–15

- Wilson RW, Jefferts KB, Penzias AA. 1970. *Ap. J.* 161:L43
- Wilson TL. 1999. *Rep. Prog. Phys.* 62:143–85
- Wilson WJ, Schwartz PR, Epstein EE, Johnson WA, Etcheverry RD, et al. 1974. *Ap. J.* 191:357–74
- Wolfire MG, Hollenbach D, McKee CF. 2010. *Ap. J.* 716:1191–207
- Wolfire MG, Hollenbach D, Tielens AGGM. 1993. *Ap. J.* 402:195–215
- Wolfire MG, Tielens AGGM, Hollenbach D, Kaufman MJ. 2008. *Ap. J.* 680:384–97
- Wong T, Hughes A, Ott J, Muller E, Pineda JL, et al. 2011. *Ap. J. Suppl.* 197:16
- Yang B, Stancil PC, Balakrishnan N, Forrey RC. 2010. *Ap. J.* 718:1062–69
- Yao L, Seaquist ER, Kuno N, Dunne L. 2003. *Ap. J.* 588:771–91
- Young JS, Allen L, Kenney JDP, Lesser A, Rownd B. 1996. *Astron. J.* 112:1903
- Young JS, Knezek PM. 1989. *Ap. J.* 347:L55–58
- Young JS, Scoville N. 1982. *Ap. J.* 258:467–89
- Young JS, Scoville NZ. 1991. *Annu. Rev. Astron. Astrophys.* 29:581–625
- Young JS, Xie S, Tacconi L, Knezek P, Viscuso P, et al. 1995. *Ap. J. Suppl.* 98:219
- Zhu M, Papadopoulos PP, Xilouris EM, Kuno N, Lisenfeld U. 2009. *Ap. J.* 706:941–59
- Zhu M, Seaquist ER, Kuno N. 2003. *Ap. J.* 588:243–63



Contents

An Unscheduled Journey: From Cosmic Rays into Cosmic X-Rays <i>Yasuo Tanaka</i>	1
Solar Neutrinos: Status and Prospects <i>W.C. Haxton, R.G. Hamish Robertson, and Aldo M. Serenelli</i>	21
Three-Dimensional Dust Radiative Transfer <i>Jürgen Steinacker, Maarten Baes, and Karl D. Gordon</i>	63
Cool Gas in High-Redshift Galaxies <i>C.L. Carilli and F. Walter</i>	105
The Dawn of Chemistry <i>Daniele Galli and Francesco Palla</i>	163
The CO-to-H ₂ Conversion Factor <i>Alberto D. Bolatto, Mark Wolfire, and Adam K. Leroy</i>	207
Stellar Multiplicity <i>Gaspard Duchêne and Adam Kraus</i>	269
Solar Irradiance Variability and Climate <i>Sami K. Solanki, Natalie A. Krivova, and Joanna D. Haigh</i>	311
Asteroseismology of Solar-Type and Red-Giant Stars <i>William J. Chaplin and Andrea Miglio</i>	353
Modeling the Panchromatic Spectral Energy Distributions of Galaxies <i>Charlie Conroy</i>	393
Nucleosynthesis in Stars and the Chemical Enrichment of Galaxies <i>Ken'ichi Nomoto, Chiaki Kobayashi, and Nozomu Tominaga</i>	457
Coevolution (Or Not) of Supermassive Black Holes and Host Galaxies <i>John Kormendy and Luis C. Ho</i>	511



ANNUAL REVIEWS

It's about time. Your time. It's time well spent.

New From Annual Reviews:

Annual Review of Statistics and Its Application

Volume 1 • Online January 2014 • <http://statistics.annualreviews.org>

Editor: **Stephen E. Fienberg**, *Carnegie Mellon University*

Associate Editors: **Nancy Reid**, *University of Toronto*

Stephen M. Stigler, *University of Chicago*

The *Annual Review of Statistics and Its Application* aims to inform statisticians and quantitative methodologists, as well as all scientists and users of statistics about major methodological advances and the computational tools that allow for their implementation. It will include developments in the field of statistics, including theoretical statistical underpinnings of new methodology, as well as developments in specific application domains such as biostatistics and bioinformatics, economics, machine learning, psychology, sociology, and aspects of the physical sciences.

Complimentary online access to the first volume will be available until January 2015.

TABLE OF CONTENTS:

- *What Is Statistics?* Stephen E. Fienberg
- *A Systematic Statistical Approach to Evaluating Evidence from Observational Studies*, David Madigan, Paul E. Stang, Jesse A. Berlin, Martijn Schuemie, J. Marc Overhage, Marc A. Suchard, Bill Dumouchel, Abraham G. Hartzema, Patrick B. Ryan
- *The Role of Statistics in the Discovery of a Higgs Boson*, David A. van Dyk
- *Brain Imaging Analysis*, F. DuBois Bowman
- *Statistics and Climate*, Peter Guttorp
- *Climate Simulators and Climate Projections*, Jonathan Rougier, Michael Goldstein
- *Probabilistic Forecasting*, Tilmann Gneiting, Matthias Katzfuss
- *Bayesian Computational Tools*, Christian P. Robert
- *Bayesian Computation Via Markov Chain Monte Carlo*, Radu V. Craiu, Jeffrey S. Rosenthal
- *Build, Compute, Critique, Repeat: Data Analysis with Latent Variable Models*, David M. Blei
- *Structured Regularizers for High-Dimensional Problems: Statistical and Computational Issues*, Martin J. Wainwright
- *High-Dimensional Statistics with a View Toward Applications in Biology*, Peter Bühlmann, Markus Kalisch, Lukas Meier
- *Next-Generation Statistical Genetics: Modeling, Penalization, and Optimization in High-Dimensional Data*, Kenneth Lange, Jeanette C. Papp, Janet S. Sinsheimer, Eric M. Sobel
- *Breaking Bad: Two Decades of Life-Course Data Analysis in Criminology, Developmental Psychology, and Beyond*, Elena A. Erosheva, Ross L. Matsueda, Donatello Telesca
- *Event History Analysis*, Niels Keiding
- *Statistical Evaluation of Forensic DNA Profile Evidence*, Christopher D. Steele, David J. Balding
- *Using League Table Rankings in Public Policy Formation: Statistical Issues*, Harvey Goldstein
- *Statistical Ecology*, Ruth King
- *Estimating the Number of Species in Microbial Diversity Studies*, John Bunge, Amy Willis, Fiona Walsh
- *Dynamic Treatment Regimes*, Bibhas Chakraborty, Susan A. Murphy
- *Statistics and Related Topics in Single-Molecule Biophysics*, Hong Qian, S.C. Kou
- *Statistics and Quantitative Risk Management for Banking and Insurance*, Paul Embrechts, Marius Hofert

Access this and all other Annual Reviews journals via your institution at www.annualreviews.org.

ANNUAL REVIEWS | Connect With Our Experts

Tel: 800.523.8635 (US/CAN) | Tel: 650.493.4400 | Fax: 650.424.0910 | Email: service@annualreviews.org

